Republic of Iraq
Ministry of Higher Education
and Scientific Research
University of Misan
College of Science
Department of Physics



Optical Gain of Si Quantum Dots Laser

A Thesis Submitted to

the College of Science / University of Misan as Partial Fulfilment of the Requirements for the Master Degree of Science in Physics.

by

Amira Hassan Hussein

B.Sc. Physics / University of Misan (2022)

Supervised by

Prof.Dr. Baqer Obaid Al-Nashy

2025 A.D. 1447 H.D.

بسم الله الرّحمن الرّحيم

((يَرْفَعِ اللَّهُ الذِيرَ آمَنُولِ مِنكُمْ وَالذِيرَ أُوتُولِ

، ، العِلمَ درجاتٍ))

صدق الله العلي العظيم (سورة المجادلة: 11)



To The Sun and Moon Which Lighting my Life by Pave the Way to my Success...

My Father & My Mother

To Those who have Supported me and are Waiting for my Success...

My brothers & My Sisters & My Friends

To The one who gave me his Time and Knowledge...

My supervisor

<u>Amira</u>



I would like to express my deepest gratitude and sincere appreciation to my supervisor, **Prof. Dr. Baqir Obeid**, for their continuous guidance, valuable advice, and unwavering support throughout the course of this research. Their encouragement and insightful feedback have greatly contributed to the success of this work.

I would like to extend my sincere thanks to **Dr. Munther Abdul Hassan** and **Prof. Dr. Ahmed Hashim** for their valuable assistance and kind support whenever I sought their help. I also thank to extend my appreciation to the Department of Physics for providing the necessary facilities and a stimulating academic environment that made this study possible.

Finally, I am deeply thankful to my family and friends for their constant support, patience, and encouragement during my academic journey.





I, the superintendent of Amira Hasan Hussein, certify that this thesis (optical gain of Si quantum dots laser) was done and written under our supervision as a fulfillment of the requirement for the master degree of science in physics.

Signature		 			

Prof.Dr Baqer Obaid Al-Nashy

Department of Physics College of Science University of Misan

Date: / 9 / 2025



Head of Physics Department Recommendation

According to the recommendation of the supervisor, this thesis is forwarded to the examination committee for approval.

Signature.....

Prof. Dr. Ahmed khalaf

Head Department of Physics College of Science University of Misan

Date: / 9 / 2025



Quantum dot lasers integrated on silicon have attracted significant attention in recent years due to the excellent optical properties of quantum dots. These lasers utilize semiconductor quantum dots as the active medium.

The integration of quantum dot lasers on silicon represents a crucial step toward achieving fully integrated photonic circuits. This integration enables low threshold operation, high thermal stability, and reduced sensitivity to defects and optical feedback compared to quantum well or conventional lasers. Moreover, compatibility with existing CMOS fabrication technologies allows for the development of cost-effective and compact optoelectronic devices.

Silicon-based quantum dot lasers are widely employed in high-speed optical communication systems, on-chip data transmission, and integrated photonic circuits. They also hold great promise for applications in quantum information processing, optical interconnects between processors, and sensing technologies, owing to their high efficiency, compact size, and tunable emission wavelengths.

In recent years, scientific literature has extensively discussed quantum dot lasers (QDLs) as a next-generation class of semiconductor light sources that exhibit superior optical performance compared to quantum well or conventional lasers. These lasers are based on nanoscale quantum dots that act as an active medium, emitting photons through transitions between discrete energy levels.

Studies have also examined the significant influence of quantum dot size distribution and density on the spectral and dynamic characteristics of the laser. Moreover, recent research has focused on the integration of quantum dot lasers with silicon platforms, which represents a crucial step toward realizing fully integrated and cost-effective photonic systems.

In Chapter One, several fundamental concepts were introduced and discussed in detail. These include the fabrication techniques of quantum dots and their various applications, the concept of optical gain along with the distinction between homogeneous and inhomogeneous broadening, the crystal structure of silicon and the Miller indices, as well as the physical characteristics of quantum dot lasers.

In Chapter Two, using a quantum disc model a detailed analysis of the energy levels within the valence and conduction bands was conducted by systematically varying the quantum dot height, radius, and the wetting layer thickness. The obtained results revealed an inverse relationship between the quantum dot dimensions (height and radius) and the corresponding energy levels, indicating that an increase in the quantum dot height leads to a decrease in the energy levels. Additionally, a schematic diagram was constructed to illustrate the possible electronic transitions occurring between these quantized energy states.

In Chapter Three, a comprehensive analysis was conducted on the relationship between the emission wavelength and optical gain by changed the quantum dot height, radius, composition, and injection current density. The results demonstrated that these parameters have a significant impact on the laser's optical performance. Notably, the study revealed that the maximum linear optical gain was achieved at a molar fraction of 0.15 barrier region for material (SiOx)and we noted upper high in more far in the wavelength in visible region.

In Chapter four, QD-L structures studied above are then modeled using the rate equations system to see the power-gain relation and to specify their dynamics.

In addition to QD ground and excited states, WL, the barrier layer is also included which is not gets an importance in the earlier studies. The results explain the interested of the barrier region in the quantum dot laser accounts. The structure Si/SiO_x when the concentration (0.15 mole fraction) is more appropriate for inline static amplification applications.

List of Symbols

Symbol	definition
$\gamma(v)$	gain constant
G_0	Amplification factor
$I_v(0)$	incident irradiance
L	distance through the medium.
Н	The Hamiltonian in the cylindrical coordinates (ρ, ϕ, z)
m_d	the effective mass inside the disk
m_b	the effective mass in the WL
V_d	the electric potential inside the disk
V_b	the electric potential in the WL
$\psi_{(\rho,\varphi)}$	wave function in the disk
$E_{ ho}$	The eigen energy in the ρ - ϕ direction,
E_d	The total eigen-energy of the quantum disk
E_z	The eigen energy in the z direction
k_z	The wave vector in the z direction
Γ	The modal linear gain
Γ_3	The modal nonlinear gain
E_s	the optical electric field of mode s
D(E')	the QD density of states for the optical transition energy E'

$C_{1,2,3,4}$	The normalization constants
$ \hat{e}.P_{cv} ^2$	the momentum matrix element for electron-heave hole transition energy in TE polarization
ê	is a unit vector in the polarization direction
$ M_{env} ^2$	The envelope function term is taken between the QD electron and hole energy states that have the same quantum numbers.
E_p	the optical matrix energy parameter
Δ_0	The spin-orbit splitting energy
Eg	the energy gap of the QD
m_0	the free electron mass
n_b	the material background refractive index
С	the light speed in the free space
ε_0	the free space permittivity
ω	the optical angular frequency and <i>e</i> is the electron charge.
S ⁱ	s ⁱ represents the degree of degeneracy
σ	the spectral variance of the QD distribution
N_D	the areal density
V_{dot}^{eff}	The effective volume of the QDs
f_c	the quasi-Fermi distribution functions for the
	conduction band
f_v	the quasi-Fermi distribution functions for the
	valence band
ω_s	the angular frequency of the optical injected signal.

$ au_c$	relaxation time constants for electrons
$ au_{in}$	the polarization relaxation time considered for the homogeneous
	broadening of the gain spectrum.
$ au_v$	relaxation time constants for holes.
p_s	the optical signal power
W	width
d	thickness
A_{21}, B_{21}	The Einstein coefficients
N	refractive index
v	The frequency
L_w	the effective thickness of the active layer is
N_Q	the surface density of QDs
D	the strip width
P_{in}	the input signal power to the SOA
g_s	The single-pass gain of the structure
S_{aV}	The average signal photon density
N_Q	Surface density of QDs
$ au_{12}$	Carrier relaxation time from GS to ES
ħ	Reduced Planck's constant
m_h^*	Effective mass of hole
m_e^*	Effective mass of electron

List of Abbreviations

Attribute	Definition
QD	Quantum Dot
QW	Quantum Well
SPR	Surface Plasmon Resonance
NMs	Nano Materials
WL	Wetting Layer
Res	Rate Equations
СВ	Conduction Band
VB	Valance Band
GS	Ground State
ES	Excited State
SA	Self-Assembled
DC	Direct Current
RF	Radio Frequency
QDs	Quantum Dots
QDL	Quantum Dot Laser
SOA	Semiconductor Optical Amplifier
SHB	Spectral Hole Burning
MBE	Molecular Beam Epitaxy
EOF	External Optical Feedback
TCDD	Total Carrier Density Depletion

List of Figures

figure	page
Figuer1.1: Application of nanotechnology.	8
Figure 1.2: Homogeneously broadened laser	10
Figure 1.3: Inhomogeneously broadened laser	11
Figure 1.4: (a) Homogeneously and (b) Inhomogeneously broadened gain.	13
Figure 1.5: Atomic structure of the of (a) crystalline,(b) amorphous, and (c) amorphous	15
hydrogenated silicon	
Figure 1.6: Top-down approach	20
Figure 1.7: Bottom-up approach.	21
Figure 1.8: Energy band structures in bulk material and quantum nanostructure	22
Figure 1.9: Fundamental processes involved in a quantum dot laser subject to	27
external optical feedback	
Figure 2.1: The Electronic structure of quantum dots varies with the size of the	36
dot.	
Figure 2.2: The diagram shows the energy levels between the valence bands	38
and the conduction bands in the Si/SiO_x in quantum dot and quantum well.	
Figure 3.1(A): Calculated gain spectra at different values of, QD-L disc height	51
for structure Si/SiO _x , spectra of an un-doped structure is dash line	
Figure 3.1(B): Calculated gain spectra at different values of, QD-L disc height	51
for structure Si/SiO _x , p-type doped structure is solid line	
Figure 3.1(C): Calculated gain spectra at different values of, QD-L disc height	52
for structure Si/SiO _x , n-type doped structure is solid line	
Figure 3.2(A): Calculated Gain Spectra at Different Values of, QDL Disc Radii	53
for Structure Si/Siox, Spectra of An Undoped Structure is Dash Line and	
Figure 3.2(B): Calculated Gain Spectra at Different Values of, QDL Disc Radii	54
for Structure Si/Siox, p-type	
Figure 3.3(C): Calculated Gain Spectra at different values of, WL mole fraction	54
for structure Si/Siox, n-type doped structure is solid line.	

for structure Si/Siox, spectra of an undoped structure is dash line Figure 3.3(B): Calculated Gain Spectra at different values of, WL mole fraction for structure Si/Siox, p-type Figure 3.3(C): Calculated Gain Spectra at different values of, WL mole fraction for structure Si/Siox, n-type doped structure is solid line Figure 3.4: Explain linear gain curves doped system Si/SiO _x at different injection current carrier concentration Figure 4.1: Four-level system in laser. 61 Figure 4.2: Levels scheme diagram of QD-Laser.
for structure Si/Siox, p-type Figure 3.3(C): Calculated Gain Spectra at different values of, WL mole fraction for structure Si/Siox, n-type doped structure is solid line Figure 3.4: Explain linear gain curves doped system Si/SiO _x at different injection current carrier concentration Figure 4.1: Four-level system in laser. 61
Figure 3.3(C): Calculated Gain Spectra at different values of, WL mole fraction for structure Si/Siox, n-type doped structure is solid line Figure 3.4: Explain linear gain curves doped system Si/SiO _x at different injection current carrier concentration Figure 4.1: Four-level system in laser. 61
for structure Si/Siox, n-type doped structure is solid line Figure 3.4: Explain linear gain curves doped system Si/SiO _x at different injection current carrier concentration Figure 4.1: Four-level system in laser. 61
Figure 3.4: Explain linear gain curves doped system Si/SiO _x at different injection current carrier concentration Figure 4.1: Four-level system in laser.
injection current carrier concentration Figure 4.1: Four-level system in laser. 61
Figure 4.1: Four-level system in laser. 61
Figure 4.2: Levels scheme diagram of QD-Laser. 63
Figure 4.3: Calculated Gain-Input power relation at J=1.335 Ka/Cm ² for the
structure Si/Sio _x , (A): The disc height for QD-L (h), (B): The disc radius(ρ) For
QD-L and (C) Mole fraction SiO _x WL.
Figure 4.4: Calculated Gain-Output power relation at J=1.335 Ka/Cm ² for the
structure Si/SiO _x , (A): The disc height (h), (B): The disc radius(ρ) And (C) Mole
fraction(x).
Figure 4.5: Plot the relation between Carrier occupation probability verse time 72
four disc high for QD-L (h=0.5 nm,1nm, 1.5 nm ,2 nm) (A) Excited state. (B)
Ground state (C) Carrier density in barrier region layer
Figure 4.6: Plot the relation between Carrier occupation probability verse time 74
four-disc radius for QD-L (ρ=8 nm,10 nm, 12 nm ,16 nm) (A) Excited state. (B)
Ground state (C) Carrier density in barrier region layer
Figure 4.7: Plot carrier concentration for different the mole fraction system 76
Si/SiO _x (x=0.11, 0.15, 0.25 and 0.35) (A) Excited state. (B) Ground state (C)
Wetting layer
Figure 4.8: Carrier density of QD occupation of GS (Red Curve) and ES (Blue 77
Curve) for structure Si/SiO ₂ A) Undoped QD-L (B) Doped QD-L.

List of Tables

Table	page
Table 2.1: Subband energy Levels for QD and WL at change dot size (radius	40
effect ρ)for the Structure Si/SiO_x	
Table 2.2: Subband energy Levels for QD and WL at change dot size (height	41
effect h) for the Structure Si/SiO_x	
Table 2.3: Subband energy Levels for QD and WL at change mole fraction	43
(concentration effect x) for the Structure Si/SiO_x	
Table 2.4: The values of important Parameters for Si and Sio ₂	43
Table 3.1: Radius ρ undoped for the Structure Si / SiO_x	46
Table 3.2: Radius ρ p-type for the Structure Si / SiO_x	46
Table 3.3: Radius ρ n-type for the Structure Si / SiO_x	46
Table 3.4: High h undoped for the Structure Si / SiO_x	47
Table 3.5: High <i>h</i> n-type for the Structure Si / Sio _x	47
Table 3.6: High h p-type for the Structure Si / SiO_x	47
Table 3.7: Different mole fraction x for barrier layer undoped for the structure	48
$\mathrm{Si/SiO}_{x}$	
Table 3.8: Different mole fraction for barrier layer n-type for the Structure	48
Si/SiO_x	
Table 3.9: Different mole fraction for barrier layer p-type for the Structure	48
Si / SiO_{x}	
Table 3.10: Values the optical gain and wavelength for different carrier surface	49
density of structure Si / SiO_x	
Table 4.:1 Parameters used in the Calculations	63
Table 4.2: Gain-Output Power for the Structure Si/Sio _x	69
Table 4.3: Gain-Input Power for the Structure Si/Sio _x	69

Table of Contents

Titles	Page
Abstract	II
List of symbols	IV
List of Abbreviations	VII
List of Figures	VIII
List of Tables	X
Chapter One: Fundamental Concepts	
1.1 Introduction	1
1.1.1 History of Nanotechnology	1
1.1.2 Properties of Nanomaterials	2
1.1.2.1 Physical Properties	2
1.1.2.3 Electrical Properties Of Nanomaterials	4
1.1.3 Types of Nanomaterials	4
1.1.4 Application of Nanomaterials	5
1.2 Optical Gain	8
1.2.1 Gain in Homogeneously Broadened Laser Systems	9
1.2.2 Gain in Inhomogeneously Broadened Laser Systems	10
1.2.3 The Difference Between Homogeneously and inhomogeneously Broadened Gain Saturation	12
1.3 Silicon	13
1.3.1 Definition and Fundamental Characteristics of Silicon	13
1.3.2 Historical Development and Discovery	13

1.3.3 Chemical Properties and Periodic Classification	14
1.3.4 Physical and Thermal Properties	14
1.3.5 crystal structure of silicon	14
1.3.6 miller index	15
1.3.6.1 How to Calculate Miller Indices	15
1.3.6.2 Miller Indices of silicon	16
1.4 Quantum Dots (QDs)	17
1.4.1 Synthesis of Quantum Dots	19
1.4.2 Applications of quantum dots	22
1.4.3 Advantages and Disadvantages	24
1.5 Quantum Dot Lasers	25
1.5.1 Physical Properties of Quantum Dot Lasers	25
1.5.2 Reflection Insensitivity of Quantum Dot Lasers	26
1.5.3 Applications of QD-Lasers	27
1.6 Literary Reviews	28
1.7 Aim of the work	32
Chapter Tow: Electronic properties of semiconductor	
2.1. Electronic Properties of Semiconductors	33
2.2. Theoretical Model	33
2.3. Quantum Disk Model	33
Chapter Three: Optical Gain	
3.1 Linear Optical Gain	44

3.2 Simulation Results and Discussion	49	
3.2.1 Quantum Size Effect (QDL Height)	49	
3.2.2 Quantum Size Effect (QD-L Radii)	52	
3.2.3 Concentration Effect WL	55	
Chapter Four: Dynamics Of Eelectron in Si QD-Laser		
4.1. Rate Equation in Laser	60	
4.2. Rate Equation	61	
4.3 Saturation Power Effect For (Si/SiO _x QD Laser)	64	
4.3.1 Saturation Input-Power Effect For (Si/SiO _x QD Laser)	64	
4.3.2 Saturation Output-Power Effect For (Si/SiO _x QD Laser)	66	
4.4. Dynamical Effects for Si/SiO _x	70	
4.5. Dynamical Effects	70	
Chapter Five: Conclusions and Recommendations and Future Work		
5.1 Conclusions	78	
Recommendations	79	
References	80	



Fundamental Concepts

1.1 Introduction

Nanotechnology has emerged in recent years as one of the most significant and fascinating frontier areas in biology, chemistry, engineering, and physics. It has a lot of promise to give us several innovations shortly that will alter the course of technological development for a variety of uses[1].

Understanding and controlling matter at sizes between 1 and 100 nm is known as Nanotechnology[2].

The Greek word nanos, which means dwarf, is where the prefix "nano-" originates. (At first, scientists only used the word to denote "very small," as in "nanoplankton," but today it denotes a billionth (1×10^{-9}) . Particles that are smaller than the typical lengths linked to specific phenomena frequently exhibit novel chemistry and physics, resulting in size-dependent behavior. Thus, for instance, it has been noted that as particles shrink below a threshold size, changes occur in their electrical structure, conductivity, reactivity, melting temperature, and mechanical properties [3].

1.1.1 History of Nanotechnology

Nanoparticle research is not a novel field. In 1925, Nobel Prize winner in chemistry, Richard Zsigmondy, was the first to suggest the idea of a "nanometer.". The American physicist and Nobel Prize laureate Richard Feynman introduced the specific concept of nano technology in 1959 in his speech during the American Physical Society's annual meeting. This is considered to be the first academic talk about nanotechnology[4].

He presented a lecture that was entitled "There's Plenty of Room at the Bottom". During this meeting, the following concept was presented: "why can't we write the entire 24 volumes of the Encyclopedia Britannica on the head of a pin?" The vision was to develop smaller machines, down to the molecular level[5].

In this talk, Feynman explained that the laws of nature do not limit our ability to work at the atomic and molecular levels, but rather it is a lack of appropriate equipment and techniques that limit this. Through this, the concept of modern technology was seeded. Due to this, he is often considered the father of modern nanotechnology[6].

The term "nanotechnology" was first used to refer to semiconductor operations that took place on the order of a nanometer by a Japanese scientist named Norio Taniguchi. He encouraged that Materials could be processed, separated, consolidated, and doped by a single atom or molecule using nanotechnology[2].

1.1.2 Properties of Nanomaterials

1.1.2.1 PHYSICAL PROPERTIES

- 1) Size: The characteristics and uses of nanomaterials are largely determined by their size. The synthesis process and the reaction conditions have a significant impact on the size of the nanostructures small size particles are more reactive than large size particles[7]. Properties including melting point, fluorescence, electrical conductivity, magnetic permeability, and chemical reactivity vary with particle size as it reaches the nanoscale[8].
- 2) Surface area: All nanomaterials have the characteristic of having surface areas that are typically significantly larger than those of their bulk counterparts, it is an important feature for adsorption, catalysis, and electrochemical. sensing "surface" applications. Nanomaterials have higher dependent material characteristics because of their extremely high surface area to volume ratio. surface effects become increasingly significant at the nanoscale due to the higher ratio of surface atoms to bulk atoms, which substantially alters the optical and electronic properties of the material. In addition, the assembly of nanoparticles can further influence electronic states through inter-particle coupling, thereby modifying the overall physical and functional characteristics of the nanostructured system.

- 3) Shape: Significant aspect. The shapes of nanoparticles that are part of the same bulk material might vary. Indeed, by regulating the synthesis process and reaction conditions, nanomaterials with certain forms may now be created [6].
- **1.1.2.2 OPTICAL PROPERTIES:** The size-dependent optical characteristics of nanomaterials are significantly influenced by two factors: surface plasmon resonance and increased energy level spacing (quantum effect).
- a) Quantum confinement effects: The quantum confinement effect is one of the fundamental phenomena that distinguish nanomaterials, as it directly influences the behavior of electrons by altering their energy levels and the bandgap between the valence and conduction bands, in contrast to bulk materials. When the crystallite size is reduced to the nanometer scale, the bandgap becomes strongly size-dependent, leading to the emergence of discrete energy levels.

The so-called quantum size effect arises when the particle dimensions approach or fall below the electron de Broglie wavelength, thereby modifying the electronic structure of the nanomaterial. As a result, a wide spectrum of fluorescence emissions can be observed, depending on the particle size. Smaller particles exhibit a larger bandgap, resulting in higher-energy emissions at shorter wavelengths (blue shift), whereas larger particles possess a narrower bandgap and emit at longer wavelengths (red shift)[8].

b) Surface Plasmon Resonance: Surface Plasmon Resonance (SPR) is an optical phenomenon that occurs in metallic nanoparticles when their size is smaller than the wavelength of the incident light. It originates from the coherent oscillations of free electrons in the conduction band at the nanoparticle surface, which resonate with the energy of the incident electromagnetic field. [9]. Noble metals such as gold, silver, and aluminum are well-known for their ability to sustain SPR because of their high density of free electrons. The resonance characteristics are strongly influenced by several factors, including the number of excited electrons, the dielectric constant of the surrounding medium, and the particle's size, shape, and

composition. Variations in these parameters lead to distinct shifts in the resonance frequency and intensity, which in turn determine the optical response of the nanostructures[8][10].

1.1.2.3 ELECTRICAL PROPERTIES OF NANOMATERIALS

When the size of a material is reduced to the nanometer scale, its electrical properties change significantly due to quantum effects. The movement of electrons (charge carriers) is altered, which can cause conductive materials (e.g. copper) to lose conductivity when extremely small, while insulating materials (e.g. silicon dioxide) may become conductive. These changes are caused by factors such as: Increased surface atoms and grain boundaries, Presence of defects or impurities, changes in the energy band gap[11].

which controls electron movement between energy levels. As nanoparticles become smaller, the available energy states for electrons decrease, and the spacing between them increases. This can shift the material's behavior from metallic to semiconducting or insulating. For instance, carbon nanotubes can act as insulators, conductors, or superconductors depending on their size, shape, and structure.

In summary: The electrical behaviour of materials is significantly changed when they are reduced to the nanoscale. The composition, size, and form of a material can cause it to change from conducting to insulating, or the other way around[12].

1.1.3 Types of Nanomaterials

Nanomaterials can be classified in several ways, including according to dimension, according to origin and environment, and according to chemical composition. However, the most common classification is based on their shape and nanoscale dimensions. nanostructured materials are classified as: zero- dimensional (0D), one-dimensional (1D), two-dimensional (2D) and three- dimensional (3D) nanomaterials.

1) Based on Dimensionality

Zero-Dimensional (0D) Nanomaterials: All dimensions are within the 1–16 nm range. Examples: quantum dots, fullerenes, nanoparticles.

One-Dimensional (1D) Nanomaterials: One dimension is larger than 100 nm, while the other two are in the nanoscale range. Examples: nanotubes, nanowires, nanorods.

Two-Dimensional (2D) Nanomaterials: Two dimensions are larger than 100 nm, while the thickness is within the nanoscale range. Examples: nanosheets, nanofilms.

Three-Dimensional (3D) Nanomaterials: Structures made of nanoscale building blocks but extended in all three dimensions, such as porous materials, nanostructured powders, or bulk nanocomposites[13].

2) Based on Origin

Natural Nanomaterials; Formed through natural physical or chemical processes, Incidental Nanomaterials; Produced unintentionally as byproducts of human activities (e.g., industrial emissions), Bioinspired Nanomaterials; Designed to mimic natural nanostructures, Engineered Nanomaterials; Intentionally manufactured for specific purposes.

3) Based on Chemical Composition

Carbon-based; e.g., fullerenes, graphene, carbon nanotubes, Metal-based / Inorganic; Nanoparticles, metal oxides, ceramics, Dendrimers; Highly branched, tree-like polymeric nanostructures, Composites; Hybrids combining different types of nanomaterials[14].

1.1.4 Application of Nanomaterials

Nanomaterials possess a diverse and extensive range of advanced applications that have revolutionized numerous scientific and industrial fields, owing to their unique properties at the nanoscale. The following sections outline the most prominent of these applications:

In Medicine and Biomedical Fields:

Nanomaterials contribute significantly to advancements in healthcare and medical treatments. Key applications include the targeted drug delivery of pharmaceuticals to specific sites within the body, and the early-stage diagnosis of diseases utilizing nanoparticles. Furthermore, they are employed in cancer treatment by directing thermal energy or therapeutic agents directly to cancerous cells, thereby enhancing treatment efficacy and minimizing adverse side effects. Additional applications encompass tissue engineering for the regeneration of damaged tissues and their use as contrast agents in medical imaging techniques such as Magnetic Resonance Imaging (MRI) and fluorescence imaging [15].

In Agriculture and Environmental:

The role of nanomaterials is evident in enhancing agricultural productivity and environmental protection. Nano-fertilizers and nano-pesticides are utilized to improve crop growth and bolster resistance to diseases. Moreover, nano-remediation techniques are applied for the purification of water and soil from contaminants.

In Energy and Industry:

Nanomaterials have contributed to the development of renewable energy technologies and advanced storage solutions. The use of materials such as quantum dots and carbon nanotubes has led to the development of solar cells with higher conversion efficiency. They have also facilitated the innovation of advanced energy storage devices, including lithium-ion batteries, fuel cells, and supercapacitors. Furthermore, nanomaterials are used in developing protective coatings with properties such as anti-wear, anti-corrosion, and self-cleaning capabilities[16]

In Electronics and Communications:

Nanomaterials have driven notable progress in the electronics industry by enabling the miniaturization of transistors, which contributes to the fabrication of faster and more

efficient processors. They have also facilitated the development of flexible electronics and high-resolution displays, in addition to highly sensitive sensors for environmental and medical monitoring.

In Textiles and Materials:

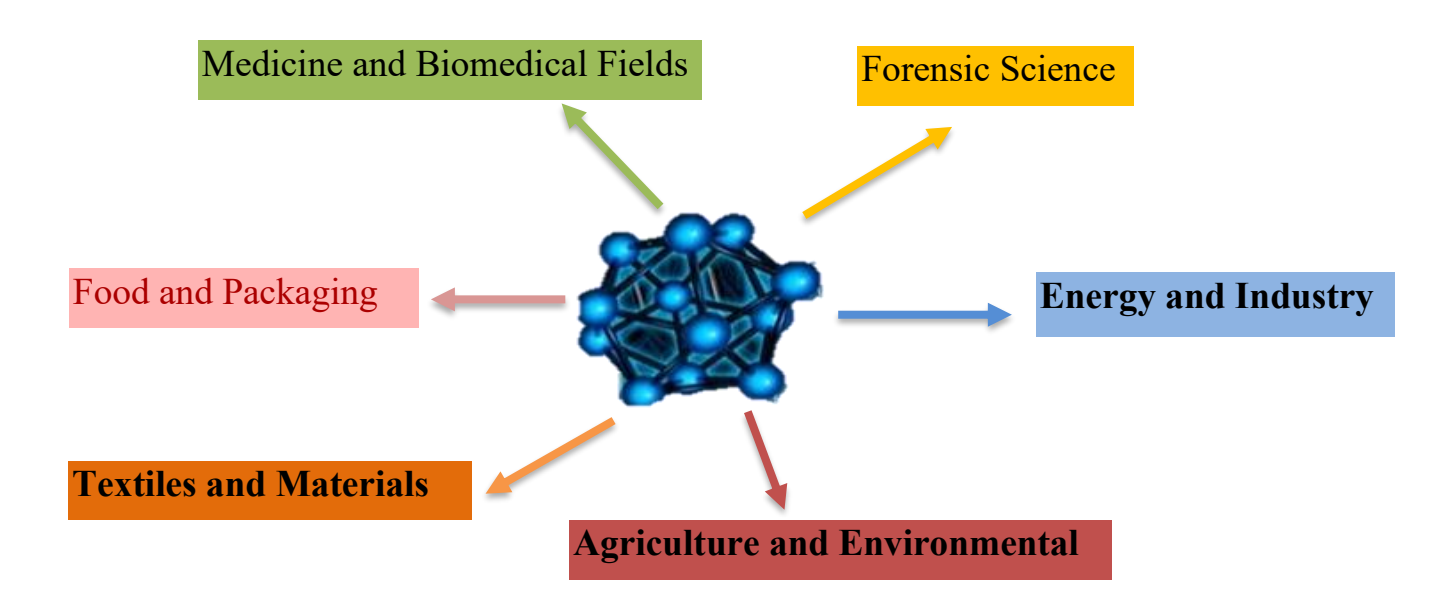
Nanotechnology has introduced substantial improvements to the textiles and materials industry. This includes the development of smart fabrics resistant to stains, wrinkles, and microbial growth. Furthermore, nanomaterials have enabled the production of lightweight, high-strength composite materials for use in sporting goods and military applications.

In Forensic Science:

Nanotechnologies have become effective tools in forensic analysis. They are employed in the analysis of trace evidence, such as fingerprints, gunshot residues, and toxic substances. They are also utilized for the extraction and analysis of DNA with very high sensitivity[13].

In Food and Packaging:

Nanomaterials have improved food quality and safety through the development of smart packaging capable of detecting food spoilage. Nano-coatings are also used to extend the shelf life of food products by acting as barriers against oxygen and moisture permeation[15].



Figuer1.1 Application of nanotechnology. Prepared by the researcher.

1.2 Optical Gain

Optical gain has long been considered an important parameter for evaluating the potential utility of laser systems. The optical gain factor g can be determined directly by measuring the intensity of the amplified spontaneous emission as a function of the length of the excitation region. The gain is usually localized to a narrow region[17].

Optical gain can be defined as: The increase in the proportion of photon density (light intensity) per unit length of light transmission,

The optical gain coefficient (g) is also expressed in inverse centimeters (cm^{-1}) , just as the optical absorption coefficient α_0 .

When an electron relocates moving from a band with lower energy to one with more energy due to photon absorption, an electron—hole pair is formed. When an existing electron-hole pair is induced to recombine, gain is produced. Producing an additional photon. The amplitude of the monochromatic wave is doubled by the second photon, which has the same wavelength and phase as the first. When this process is repeated,

considerable amplification of light results. The absorbing of photons through the creation of new electron-hole pairs, however, is the competing process.

When the conduction band, which is the higher energy level, contains more electrons, than at the lower energy level, stimulated emission predominates. Valence band level. By supplying valence band holes from the p-doped side and conduction band electrons from the n-doped side, np-junctions can investigation this inversion of the carrier population[18].

$$g = \frac{I_v(L)}{I_v(0)} = e^{\gamma(v)L}$$
 [1.1]

where: g Amplification factor, $\gamma(v)$ gain constant, $I_v(0)$ incident irradiance, L distance through the medium.

Where:

 $\gamma(v)$ = 0, the beam can travel through the medium without any profit or loss is regarded as transparent.

 $\gamma(v)$ > 0, when the gain constant bigger than zero the medium functions as an amplifier

 $\gamma(v)$ < 0, when the gain constant smaller than zero the medium functions as an attenuator

1.2.1 Gain in Homogeneously Broadened Laser Systems

Homogeneous broadening; all atoms, molecules behave similarly in the light-matter interaction, they have the same individual lineshape function. This interaction typically results in a Lorentzian spectral shape, which is characterized by a bell-shaped curve. The broadening of these spectral lines can be attributed to several common factors, including: lifetime or natural broadening, collision or pressure broadening[19].

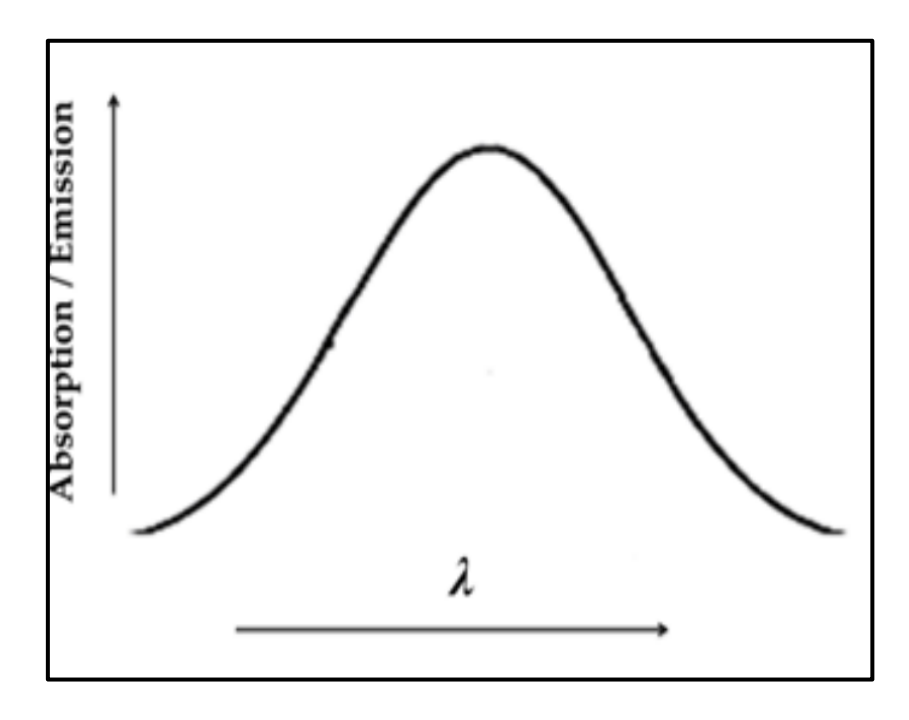


Figure 1.2 Homogeneously broadened Laser [20]

To achieve optical amplification, the population distribution of atoms must deviate from the natural Boltzmann distribution through the establishment of a population inversion. This inversion can only be realized by supplying external energy that selectively excites one or more energy levels. This selective excitation process is referred to as optical pumping.

1.2.2 Gain in Inhomogeneously Broadened Laser Systems

Group of atoms and molecules behave differently in the light matter interaction, the whole system can be characterized by an average lineshape function, The phenomenon results in a Gaussian spectral shape characterized by overlapping narrow spectra emitted by each individual capsule within the medium. This interplay leads to the formation of a broad spectrum that is partially multi-peaked, highlighting the complexity of the spectral distribution.

Several factors can contribute to this intricate broadening of the spectral lines. One notable factor is Doppler broadening, which occurs due to the thermal motion of atoms in gaseous environments. As atoms move at varying speeds, the frequency of the

emitted light waves is shifted—those moving toward the observer exhibit a higher frequency (blue shift), while those moving away exhibit a lower frequency (red shift). This collective movement results in a spread of wavelengths rather than a singular frequency.

When the gain medium is inhomogeneously broadened, the velocity of the atomic particles mostly determines the line shape for stimulated emission. Collisional broadening and each particle's inherent linewidth determine its line shape. Nevertheless, the motion of the particles causes a Doppler shift that is far greater than the linewidths of the individual particles. Thus, the resulting line shape can be described as the superposition of many overlapping Lorentzian distributions that arise from the random motion of particles. The subset of particles whose absorption frequency coincides with the incident wavelength interacts most effectively with the incoming narrowband beam, while other groups of particles contribute differently as the beam propagates through the medium [21].

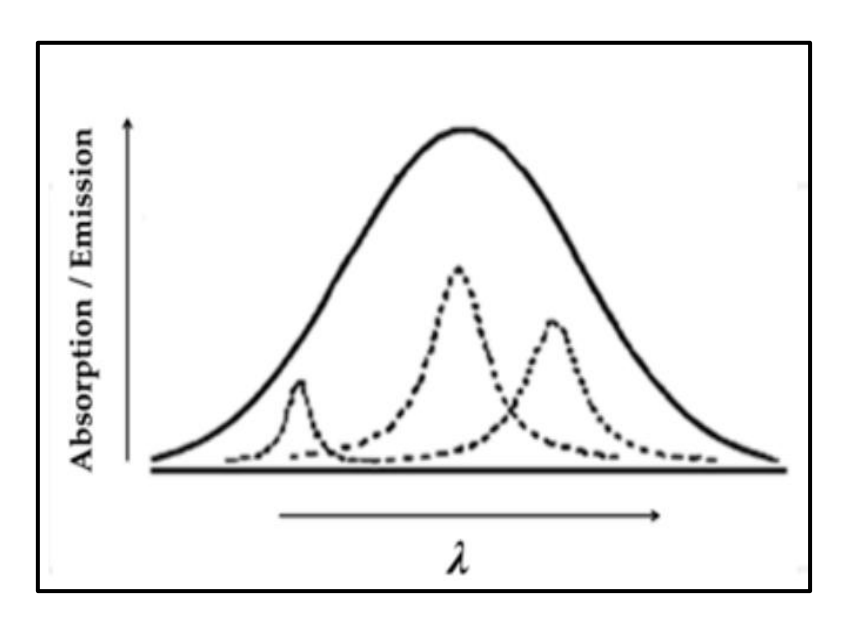


Figure 1.3 Inhomogeneously broadened laser [20]

1.2.3 The Difference Between Homogeneously and inhomogeneously Broadened Gain Saturation

How the behavior of a laser medium under saturation differs between two fundamental cases: homogeneous broadening and inhomogeneous broadening, and how this difference directly affects the laser's efficiency and its ability to produce more than one frequency.

In inhomogeneously broadened media, the particles in the medium do not all share the same resonant frequency; instead, they are distributed over a broad spectral range. When a laser beam passes through and saturates a specific group of particles (those resonant with its frequency), other groups lying outside this exact frequency range can still absorb or amplify radiation at different frequencies. As a result, the gain does not suddenly disappear after saturation it continues to be provided by other groups. This phenomenon is known as hole burning (Spectral hole burning is a high-resolution spectroscopic technique that enables the investigation of heterogeneous nanoscopic environments. It operates through the creation of a 'hole' or dip in the spectral absorption of a material at a specific optical frequency, which is achieved by irradiating the material with an intense, frequency-selective laser), and it is the reason why inhomogeneously broadened media can support and operate at multiple laser frequencies simultaneously[22].

In homogeneously broadened media, nearly all particles share the same resonant frequency. Here, when the laser beam reaches saturation, it affects all particles at once, causing a rapid and uniform drop in gain across the entire spectrum. As a result, this type of medium cannot easily support multiple laser frequencies, since any strong beam will saturate the whole medium at once.

The core idea is that saturation in inhomogeneous broadening is slower and more "selective," whereas in homogeneous broadening it is faster and more "global." This

difference determines how the laser operates and how many wavelengths it can produce at the same time[23].

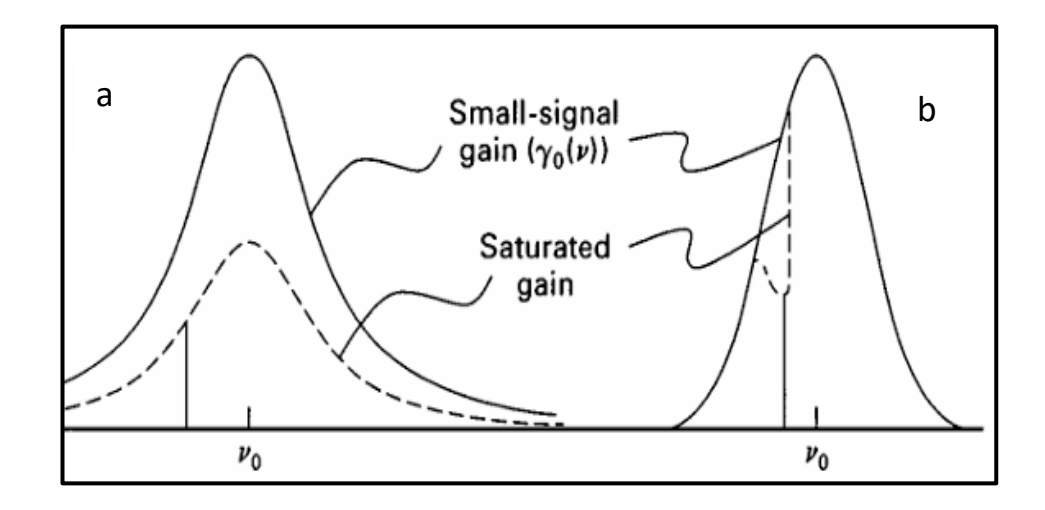


Figure 1.4 (a) Homogeneously and (b) Inhomogeneously broadened gain[23].

1.3 Silicon

1.3.1 Definition and Fundamental Characteristics of Silicon

Silicon is classified as a semiconductor characterized by an indirect band gap, Whose energy gap is 1.12eV, which significantly reduces the likelihood of phonon-assisted radiative electron-hole recombination[24]. This property leads to spontaneous photon emission under specific conditions. When the particle size approaches the bulk Bohr radius (4 nm for silicon), the element exhibits notable changes in its optical and electrical characteristics, demonstrating quantum confinement effects that are of considerable interest applications in nanotechnology [25].

It is a covalent crystal that has a diamond cubic lattice structure. The lattice constant of silicon is 5.43A°, and the distance between the neighboring covalently bonded silicon atoms is 2.35 A°, the unit cell contains eight atoms, and the atoms follow a face centered cubic (fcc) Bravais lattice [26].

1.3.2 Historical Development and Discovery

The discovery of silicon dates back to 1824, when Swedish chemist Jacob Berzelius first identified it as a distinct element. Scientific advancement continued until Henry Sainte-Claire Deville successfully synthesized the first crystalline silicon in 1854. This scientific achievement laid the groundwork for advanced technological applications of the element in the modern era, particularly in the development of semiconductor technology and electronic devices[27].

1.3.3 Chemical Properties and Periodic Classification

Silicon is denoted by the chemical symbol Si and possesses an atomic number of 14, positioning it in Group 14 of the periodic table, they are arranged in the electron configuration [Ne]3s²3p². The element is classified as a tetravalent metalloid, characterized by its hardness and brittleness as a crystalline solid with a distinctive blue-grey metallic luster. Its tetravalent nature enables the formation of four covalent bonds, making it fundamental to various chemical. Compounds and crystalline structures[28]

1.3.4 Physical and Thermal Properties

Silicon exhibits remarkable thermal stability with a melting point of 1414°C and a boiling point of 3265°C. These values represent the second highest melting and boiling points among metalloids and nonmetals, surpassed only by boron. This exceptional thermal stability makes silicon particularly valuable in high-temperature applications and contributes to its widespread use in industrial processes requiring materials capable of withstanding extreme thermal conditions[28].

1.3.5 CRYSTAL STRUCTURE OF SILICON

1. Monocrystalline Si (mono-Si): Silicon atoms are arranged in a single homogeneous lattice without any grain boundaries.

- 2. Polycrystalline Si (poly-Si): Composed of several small crystals adjacent contains several granules.
- 3. Amorphous Si(a-Si): It does not possess a regular periodic, crystal structure, with atoms distributed in a random manner.
- 4. Hydrogenated amorphous Si(a-Si:H): is an improvement over conventional amorphous silicon, characterized by the addition of hydrogen atoms during the deposition process to reduce structural defects and improve electronic properties.[29]

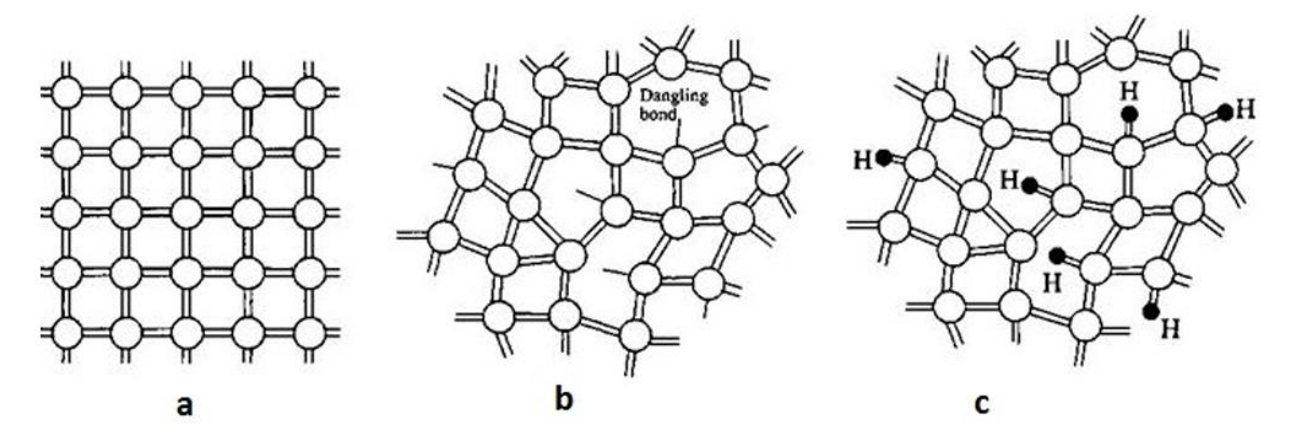


Figure 1.5: Atomic structure of the of (a) crystalline,(b) amorphous, and (c) amorphous hydrogenated silicon[30].

1.3.6 MILLER INDEX

Miller indices are a convenient mathematical system used to describe atomic planes and directions in crystal lattices. They are written in the format (h k l). Miller indices are easy to use when the crystal lattice has: Cubic structure (like silicon lattice) Maximum symmetry Orthogonal axes Identical lattice parameters in all x, y, z directions[31].

1.3.6.1 How to Calculate Miller Indices

- 1. Determine the intercept points where the plane intersects the x, y, z axes
- 2. Take the reciprocals of these intercept points
- 3. Obtain the numbers (h k l)

1.3.6.2 Miller Indices of silicon

- 1. The (100) plane intersects the x-axis at 1, y-axis at ∞ , z-axis at ∞ . Inverted (1,0,0).
- 2. The (110) plane intersects the x-axis at 1, y-axis at 1, z-axis at ∞ . Inverted (1,1,0).
- 3. The (111) plane intersects the x-axis at 1, y-axis at 1, z-axis at 1. Inverted (1,1,1).[31]

Silicon dots (Si dots) can be synthesized through a variety of methodologies, which can be broadly categorized into physical, physicochemical, chemical, and electrochemical procedures.

Physical methods often involve high-temperature processes combined with vacuum deposition techniques, such as sputtering or thermal evaporation. These techniques are typically employed to produce small quantities of Si dots, which are vital for physical and electronic applications, including photovoltaic cells and semiconductor devices. The high-temperature environment enables precise control over the dot size and morphology, which are crucial factors in determining the electronic and optical properties of the resulting materials[24].

physicochemical routes may include sol-gel processes and other hybrid methods that combine chemical and physical approaches to create nanoparticles in a more controlled setting. These methods can lead to uniformity in size and enhanced surface properties, making them suitable for various applications in nanotechnology and materials science.

Chemical methods, such as liquid-phase synthesis, enable the production of Si dots at lower temperatures and can be tailored to create dots of various sizes and surface modifications. These approaches are beneficial for applications in biomedicine and sensor technology.

Finally, electrochemical procedures involve the electrochemical etching of silicon in solutions, a method that can yield highly uniform Si dots with specific surface

characteristics. This versatility in preparation methods makes Si dots a fascinating subject of study with significant implications across multiple fields, including electronics and photonics[32].

1.4 Quantum Dots (QDs)

Quantum dots (QDs) have attracted considerable attention from physicists, chemists, and materials engineers over the years due to their fascinating carrier confinement effects. These effects arise when the motion of charge carriers within a solid is limited in certain directions to dimensions comparable to their de Broglie wavelength, leading to discrete energy levels along those dimensions. This quantization of energy levels is especially significant when charge carriers are confined in all three dimensions, as is characteristic of quantum dots[33].

Due to quantum confinement phenomena, quantum dots—nanoscale semiconductor particles that are usually between 2—10 nanometers in size—display special optical and electrical characteristics. Because electrons in quantum dots are restricted to such small dimensions, their energy levels become discrete, much like those of atoms. This enables quantum dots to produce light at specific wavelengths depending on their size[34].

Herbert Fröhlich first proposed in 1937 that the macroscopic size of a tiny particle might affect its material qualities. He noted that the conclusions of the free-electron gas model for metals[35] are significantly different for tiny particles than for bulk metals, and that these variations ought to show up in a measurable material attribute, specifically the specific heat of the electrons. He calculated that temperatures of a few degrees Kelvin and metal particles smaller than 10 nm would be enough to observe this phenomenon[36] [37].

An intense interest in the electrical characteristics of thin films was sparked by the advancement of microelectronics in the 1960s. Quantum effects showed up as oscillations of resistivity, Hall resistance, and magnetoresistance as a function of film thickness in studies carried out in thin bismuth layers and in two-dimensional electron gas generated at silicon surfaces. The measured oscillations' periodicity matched the wavelength of the electron at the anticipated effective mass. It was determined that low temperatures and long enough carrier relaxation durations are necessary for energetically resolving quantization effects[38].

In the context of colored glass, quantum size effects in nanoparticles were initially discovered. In the past, glassmakers were well aware that dopants such as cadmium, gold, selenium and silver, may change the optical properties of glass. For instance, Schott glasses, or optical filters with different cut-off frequencies, were made by controlling the kind and amount of dopant and the details of the thermal process after glass melting.

At the S.I. Vavilov State Optical Institute, Alexei Ekimov started developing doped glasses in 1979. His goal was to comprehend the structure, chemical makeup, and development process of the colloidal particles in colored glasses. He and his colleagues evaluated the optical absorption spectra of heat-treated silicate glasses with additions of Cu and Cl of the order of a few percent, exceeding the matrix's solubility limit, using methods he was accustomed to from his Ph. D. training in semiconductor physics.

Ekimov's discovery of semiconductor quantum dots in a glass matrix showed that, in addition to thin films, suspended, independent nanoparticles created using a fairly simple conventional glass process may also exhibit notable indications of quantum size effects. But the fact that Ekimov's team's quantum dots were "frozen" in glass and could not be processed further19 hampered his ground-breaking discovery[39].

1.4.1 Synthesis of Quantum Dots

Numerous approaches and strategies have been developed for the manufacture and synthesis of quantum dots (QDs). These techniques seek to precisely manage the size, shape, internal structure, and geometric dimensions of quantum dots, among other physical characteristics. Through these techniques, quantum dots' performance may now be optimised for a range of energy, photonic, and electronics applications. In generally speaking, the two primary approaches that are most frequently employed in this subject are as follows:

- A. Bottom-up approach
- B. top-down approach

Top-down approach

depends on dissolving or fracturing solid (bulky) materials into particles or structures at the nanoscale. Physical techniques are the foundation of this strategy. These approaches are extensions and advancements of the same procedures that were previously employed to create particles the size of micrometers; thus, they are not wholly novel. Because it just requires removing a portion of the solid material or breaking it up into tiny bits, or by scaling down the standard manufacturing processes to the nanoscale to get the appropriate size structures, this approach is comparatively easier than certain other approaches. This approach's disadvantage is that it creates imperfect surfaces; the resulting nanostructures are a little rough, have surface faults known as structural defects, and may contain impurities. This approach or process can be illustrated by the figure (1.7)[40].

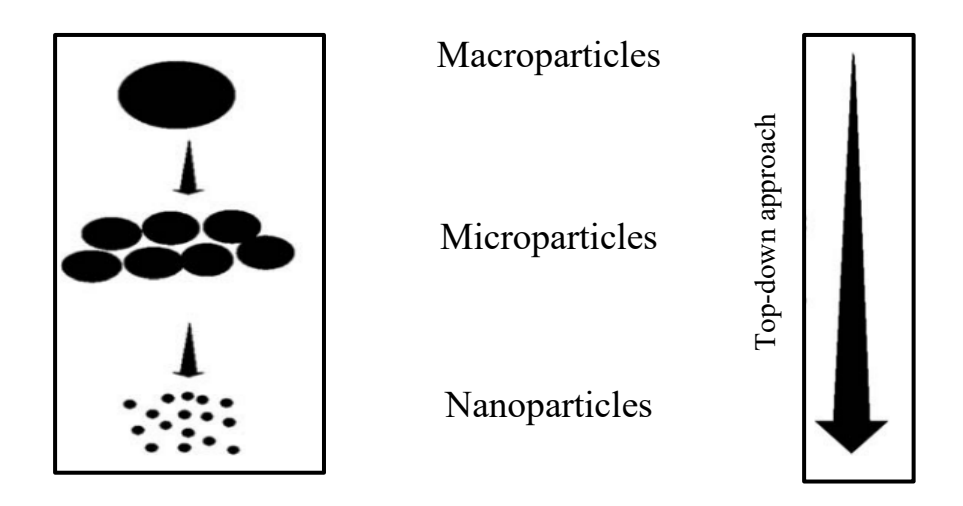
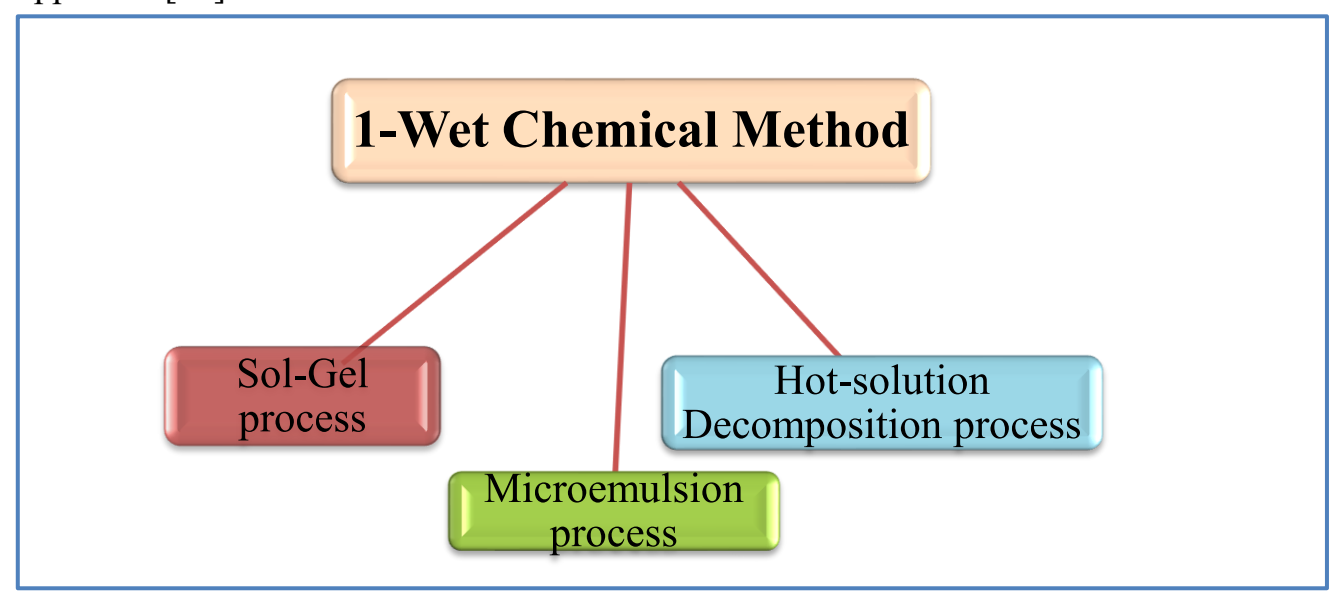


figure 1.6 Top-down approach.

Bottom-up approach

In these methods, building block atoms or molecules are carefully deposited via controlled chemical reactions, thus making the process cheaper and nanostructures of the 2-10 nm range could be easily made by these processes. Self- assembly of few hundred and molecules could make nanostructures. The bottom-up approach is generally divided into two main types: wet chemical and vapor-phase methods. The majority of these techniques rely on chemicals. These are also cost-effective. Using this method, a material is constructed from the bottom up—atom by atom, molecule by molecule, cluster by cluster, etc. In this diagram we show the methods used in this approach.[41]



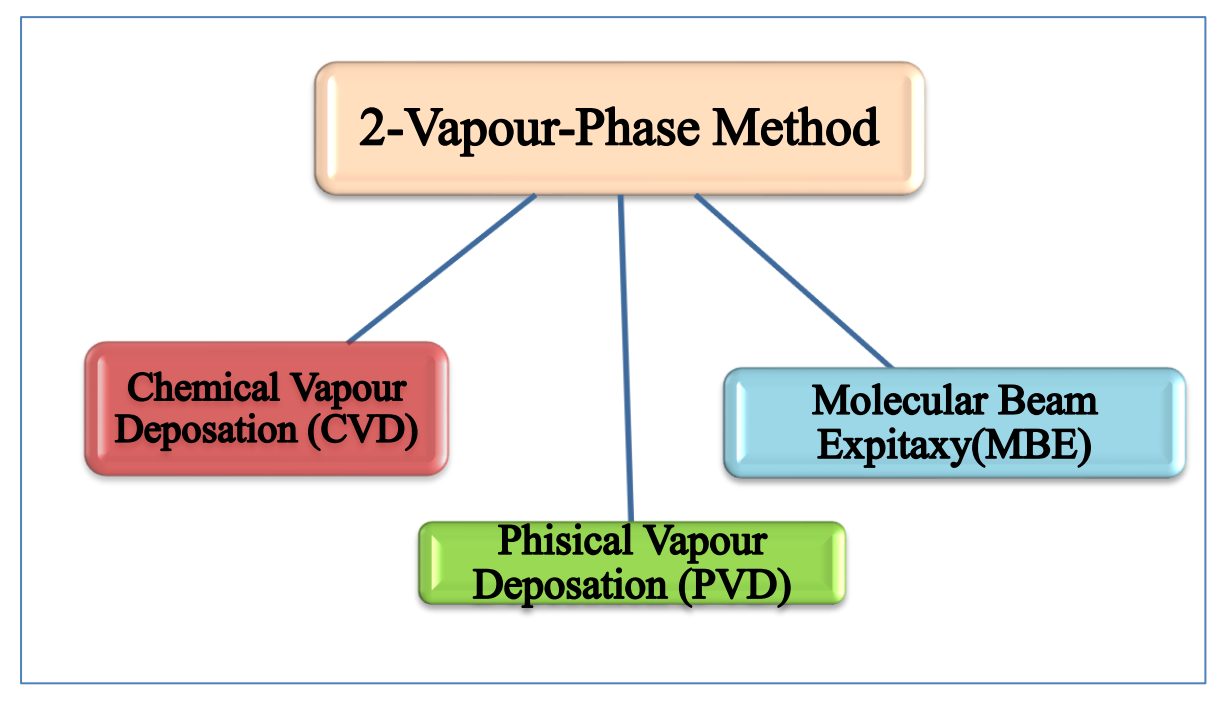


Diagram1.1: Diagrams showing wet chemical methods and vapor-phase methods for preparing nanomaterials. Prepared by the researcher,

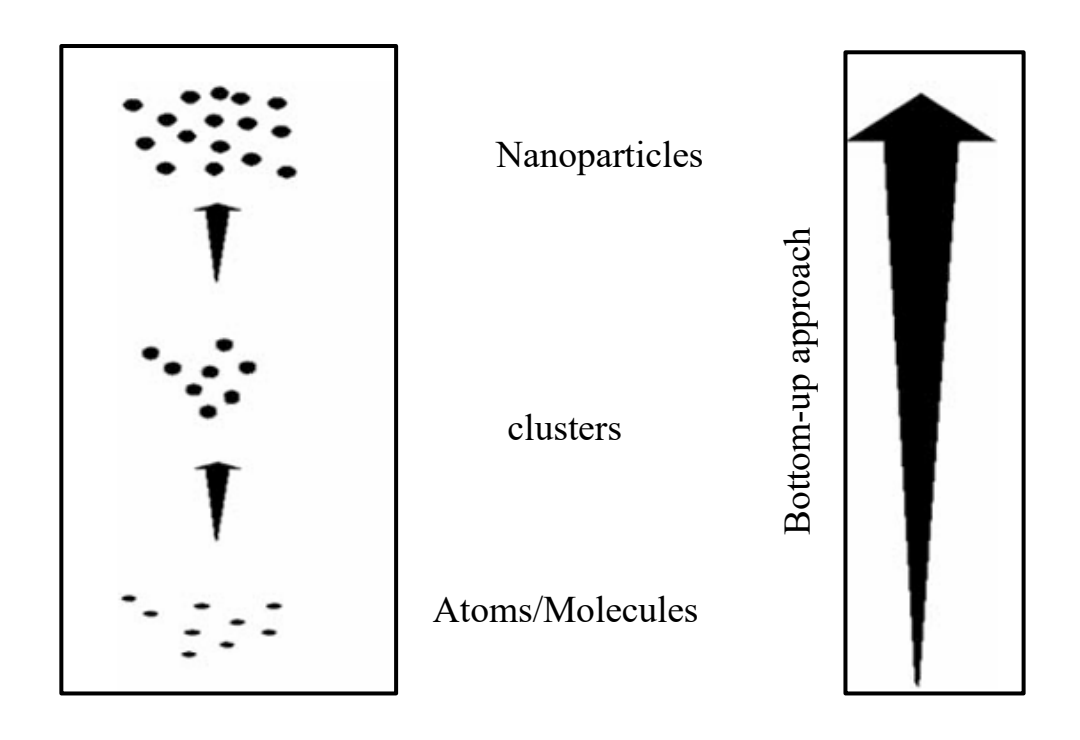


figure 1.7 Bottom-up approach

In figure (1.8), the size-dependent energy bandgap is one of the main distinctions between QDs and bulk materials. The bandgap of bulk materials remains constant regardless of size, as it is a feature of the material itself. In contrast, the bandgap in QDs, is inversely proportional to the QDs size. Because it affects the strength of the quantum confinement effect, the size of the QDs is significant. Compared to bigger QDs, smaller QDs have greater energy levels and better quantum confinement. For the development and production of novel devices and their uses, controlling the QD's size throughout growth is crucial. This size-dependent bandgap results in a variety of optical characteristics, such as adjustable emission and absorption spectra[39].

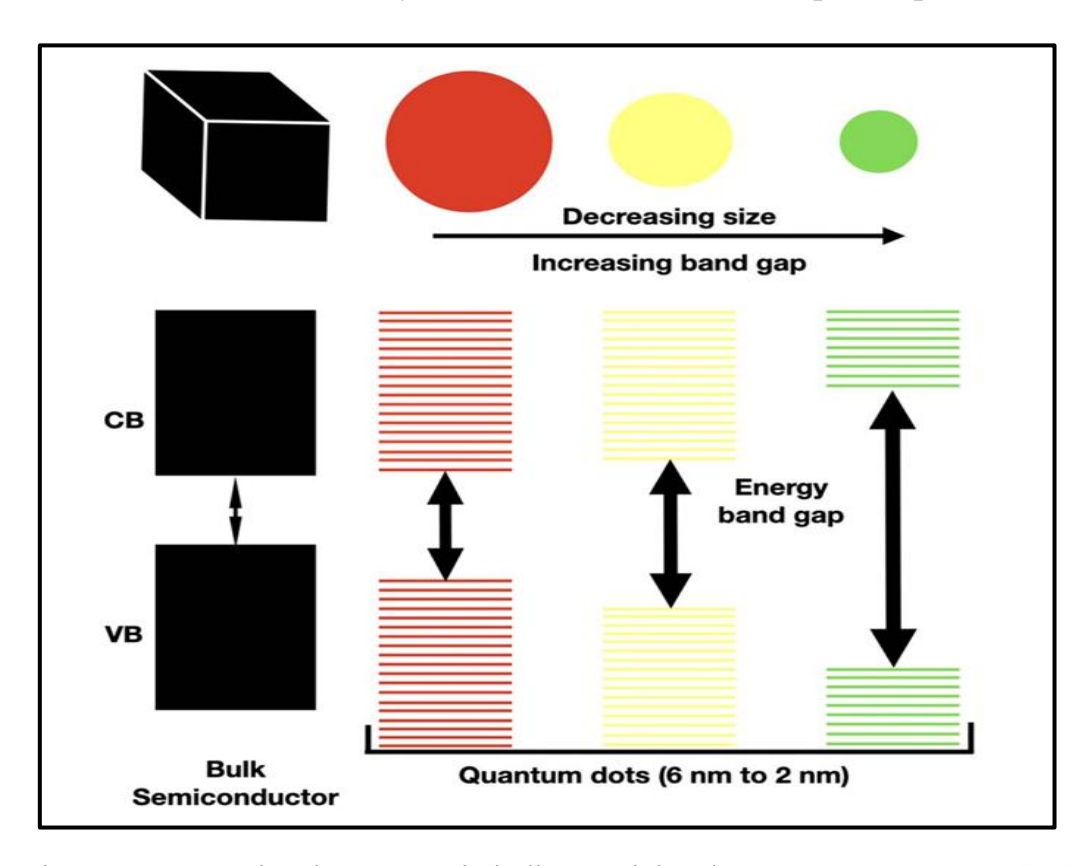


Figure 1.8 energy band structures in bulk material and quantum nanostructure[39]

1.4.2 Applications of quantum dots

While quantum dots have several uses that span a broad spectrum, the following are the primary uses:

1) Quantum Dot Solar Cells (QDSCs): represent a promising next-generation photovoltaic technology due to their high efficiency, tunable optical properties,

low-cost potential, and flexibility. They offer significant opportunities for commercial applications, especially in building-integrated photovoltaics (BIPV) and portable/wearable devices, such as smart textiles and self-powered electronics. [42]

- 2) Cancer therapy: Cancer incidence and mortality rates are continuously rising, largely due to the difficulty of detecting the disease at early stages, which reduces treatment effectiveness and increases the risk of recurrence. To address this challenge, nanotechnology has emerged as a promising field, with carbon quantum dots (CQDs) receiving considerable attention because of their unique optical properties, high fluorescence stability, and tunable size and structure. CQDs show great potential in cancer applications. In diagnostics, they enable the development of advanced devices that accurately distinguish between normal and malignant cells, thereby improving early detection and the reliability of assays. In therapeutics, they facilitate targeted drug delivery to cancer cells, which minimizes side effects on healthy tissues and enhances the bioavailability of drugs[43].
- 3) Bioimaging: Quantum dots (QDs) are considered highly promising materials for biomedical applications, particularly in live cell imaging and in vivo imaging, due to their unique optical properties such as high quantum yield, strong brightness, large extinction coefficient, and remarkable resistance to photobleaching QDs also serve as excellent fluorescent probes for detecting intracellular components, as they are readily internalized by living cells and provide strong optical signals that can be visualized using fluorescence microscopy techniques such as confocal laser scanning microscopy (CLSM). Furthermore, their surfaces can be functionalized with specific ligands to enhance selectivity toward certain proteins or receptors, thereby broadening their potential in high-resolution biomedical imaging and diagnostic applications[44].
- 4) Light-emitting diodes (LEDs): Used in displays and LEDs for purer and brighter color, due to their distinctive photoluminescence, narrow emission bandwidth, and

wide color gamut coverage, quantum dots offer unparalleled advantages in advanced display technologies, enabling the production of full-color micro-LED displays. It is essential to understand how the properties of quantum dots affect the performance of micro-LED displays to develop the most energy-efficient display devices in the near future. However, in-depth investigation of stability issues and loading methods in quantum dots is critically important to accelerate the commercialization of QD-based LED technologies[45].

1.4.3 Advantages and Disadvantages

Advantages

- 1. exhibit high quantum yields, meaning they produce intense and bright fluorescence upon excitation. A substantial proportion of the absorbed energy is converted into photon emission rather than being dissipated as heat [46].
- 2. High Photostability Unlike many organic fluorophores and conventional dyes, quantum dots demonstrate exceptional photostability. They maintain their emission capabilities over extended periods without significant photobleaching, ensuring sustained and reliable fluorescence signals during prolonged exposure [47].
- 3. Symmetric and Narrow Emission Spectra Quantum dots produce emission spectra characterized by narrow, symmetric peaks. This spectral purity provides well-defined, monochromatic emission with minimal spectral overlap, enabling precise wavelength selection and reducing interference in multiplexed detection systems[47].
- 4. Longer Lifetime Quantum dots possess significantly longer fluorescence lifetimes compared to organic fluorescent molecules.
- 5. Size-Tunable Optical Properties The emission wavelength of quantum dots can be precisely controlled by modulating their size and morphology. Smaller nanocrystals emit at shorter wavelengths (e.g., blue region), while larger particles shift emission

toward longer wavelengths (e.g., red region), enabling wavelength tunability across the visible and near-infrared spectrum.

Disadvantages

- a) Extended lifetime may create a problem when rapid degradation is required.
- b) High toxicity, when used in vivo.
- c) Blinking of quantum dots makes them invisible sometimes.
- d) Decline of fluorescence exponentially

1.5 Quantum Dot Lasers

Originally the idea to exploit quantum effects in heterostructure semiconductor lasers to produce wavelength tunability and achieve lower lasing thresholds via the change in the density of states which results from reducing number of translational degrees of freedom of the carriers was introduced in 1976 by Dingle and Henry.

The history of semiconductor lasers, starting with bulk lasers, moving on to heterostructure lasers, and culminating with quantum-based lasers, is closely linked to the history of quantum dot lasers.[48]

1.5.1 Physical Properties of Quantum Dot Lasers

The quantum dot (QD) structure provides a unique physical basis for lasers, as it generates an electronic energy distribution comparable to that of an isolated atom. Owing to their narrow bandwidth, quantum dots emit photons of well-defined energy when excited. Since the emission wavelength is directly related to the size of the quantum dot, it becomes possible to tune the photon wavelength by adjusting the dot dimensions. This size-dependent quantum confinement effect allows for flexible wavelength control, which is a critical advantage in laser design. Compared to quantum well lasers, quantum dot lasers exhibit several superior properties. These include higher temperature stability, lower threshold current density, enhanced modulation speed, and narrower linewidth. Additionally, QD lasers display a reduced linewidth enhancement

factor, minimized reflection sensitivity, and improved resistance to material defects. Such characteristics result in improved coherence and reduced susceptibility to performance degradation under varying operating conditions. From a structural perspective, quantum dots can be regarded as zero-dimensional counterparts of quantum wells. Their three-dimensional confinement leads to discrete energy states, which contribute to their distinctive optical and electronic properties. In practice, fabricating quantum dots requires embedding a narrow-bandgap material within a wide-bandgap host matrix. The physical characteristics of quantum dot lasers—stemming from their discrete energy levels, size-tunable emission wavelengths, high temperature resilience, and reduced noise—make them exceptionally promising for advanced optoelectronic applications. These properties not only distinguish them from traditional quantum well lasers but also enable their use in demanding environments such as high-speed optical communication, integrated photonic circuits, and low-power photonic devices [49].

1.5.2 Reflection Insensitivity of Quantum Dot Lasers

One of the major challenges facing on-chip laser sources is their sensitivity to optical feedback, particularly in silicon-based photonics. This phenomenon can lead to instability in laser operation, which negatively affects performance in practical applications. In this regard, quantum dot lasers monolithically integrated on silicon have demonstrated a remarkable ability to resist feedback effects, while simultaneously maintaining key advantages such as low-cost, high-energy efficiency, and scalable fabrication. The mechanism of optical feedback arises from the re-coupling of a portion of the emitted radiation back into the laser cavity, which induces perturbations in the photon density. These perturbations manifest as fluctuations in both amplitude and phase. Amplitude fluctuations are linked to carrier density and optical gain, whereas phase fluctuations result in wavelength shifts. In certain cases, the interaction between these fluctuations can give rise to severe instabilities in the laser output, including

chaotic oscillations or coherence collapse. In the field of optical communications, this phenomenon is typically analyzed by identifying the critical feedback level, which marks the onset of laser destabilization due to the interaction between the returned and emitted optical powers. Once this threshold is exceeded, undesirable dynamic behaviors emerge, ultimately degrading the stability and performance of the laser. Figure (1.9) schematically describes the fundamental processes involved when a semiconductor QD laser operates under optical feedback[50].

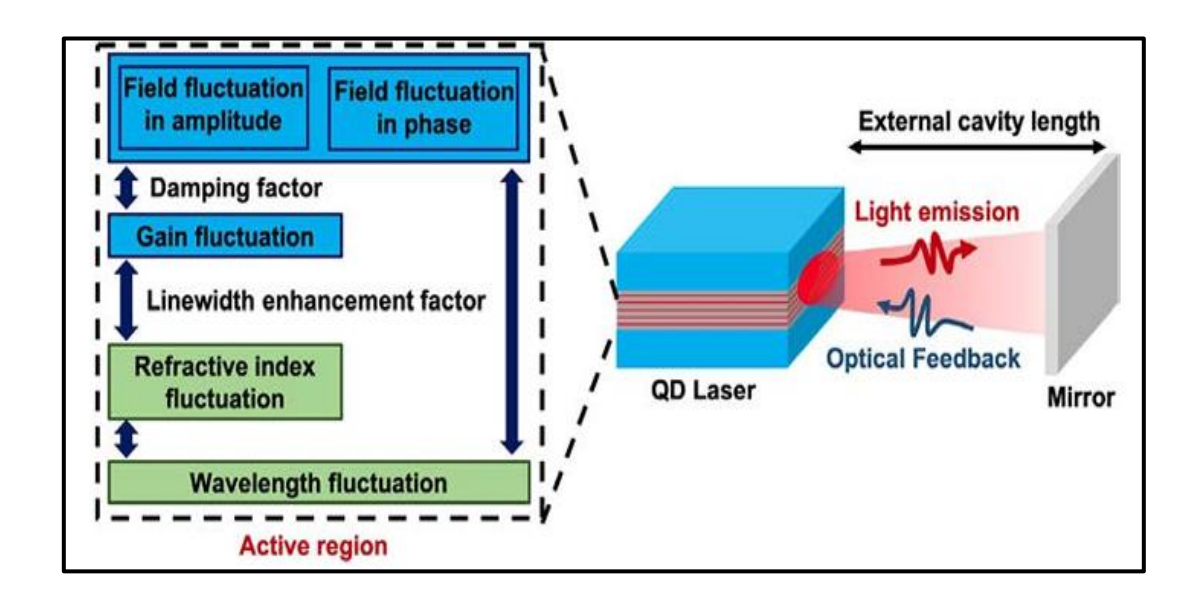


Figure 1.9 Fundamental processes involved in a quantum dot laser subject to external optical feedback[50].

1.5.3 Applications of QD-Lasers

Applications of QD Lasers The use of quantum dot (QD) lasers is steadily expanding, opening new avenues for laser applications. Currently, QD laser technology covers nearly the entire spectral range of 1.15–1.25 μm, which is particularly significant for medical applications. Within this range, InP-based lasers show limited efficiency at wavelengths below 1.3 μm[51], while InGaAs quantum well (QW) GaAs-based lasers face challenges at wavelengths above 1.15 μm due to limitations associated with InGaAs material properties. A major advancement in the field has been achieved with the development of InGaN–AlInGaN QD lasers, which benefit from the

wide bandgap of InGaN. The formation of InGaN QDs arises from the natural phase separation effect induced by local strain relaxation, driven by compositional fluctuations. Since III–V semiconductors are prone to strain caused by lattice mismatch with substrates (in multilayer systems) or with bulk lattice constants, the resulting strain relaxation in localized regions promotes phase separation. This structural phenomenon has been observed in a wide range of III–V materials such as InGaP, InGaAlSb, InGaAsP, and InGaAsN [52].

1.6 Literary Reviews

In 2010, Baqer et al. They study both linear and nonlinear gain spectra in optical amplifiers (SOAs) based on Sb-based quantum-dot (QD) semiconductors. Additionally examined are the effects of Sb-composition, quantum size, and homogeneous linewidth in the QD, wetting, and barrier layers. InAs_{0.3}Sb_{0.7} and InSb QD-SOAs provide sufficient gain saturation. The study covers the wavelength range of 1000–7000 nm[53].

In 2011, Zhenhui et al. concentrate on the production and PL characteristics of tiny Si nanoparticles as well as their possible uses in nano catalysis and bioimaging. In addition and further highlight major challenges and promises in this area[24].

In 2012, Muaffak et al. Studied the CdSe/ZnSe quantum dot semiconductor optical amplifier is studied theoretically where the core/shell composition is clarified. Coefficients of absorption and emission as well as the noise figure are examined. Comparing the obtained emission coefficient to the same structure of InGaAs/InP, it is greater. A 25dB gain is obtained. A low noise figure (5.5dB) is obtained [54].

In 2013, Lorenzo. The author discussed the characteristics and production of silicon nanocrystals. A number of methods have been put forth for the controlled production of silicon nanoparticles, including gas-phase nucleation and growth in silane-containing nonthermal plasmas and nucleation in substoichiometric thin films. The use of silicon nanocrystals for the development of novel electronic devices, light emitting devices, photovoltaic cells, and for biorelated applications, Waste heat recovery and energy storage applications are also discussed [55].

In 2014, Omar. The study linear optical gain of gain-clamped quantum dot semiconductor optical amplifiers (GCSOAs explained When the amplifier runs at ground state and the laser emits 90meV above ground state, a significant linear optical gain may be achieved, resulting in an energy separation of 81MeV between the laser and amplifier and fund that larger detuning between the laser and amplifier energy result in gain saturation[56]

In 2015, Alan et al. talked the latest developments in silicon quantum dot laser technology. The device's performance, dependability, and comparability to other comparable silicon-grown quantum well lasers outlined and they studied the potential for future short-reach silicon photonics interconnects using scalable, low-size, low-weight, and low-power nano lasers generated on silicon made possible by quantum dot active areas [57].

In 2018, Norman, Justin. The study discussed the results achieved include continuous-wave threshold currents below 1 mA in micro-scale ring laser cavities, single-facet output powers of 175 mW at 20 °C, continuous wave lasing up to 105°C, near zero linewidth enhancement factor, isolator-free xvi stability at optical feedback levels of up to 90%, and record long device lifetimes on silicon of more than 100 years at 35°C based on extrapolated 8,000-hour aging studies, and >100,000 h lifetimes at 60°C from extrapolated 4,000-hour aging studies. These results show potential to revolutionize

integrated photonics through economic advantages and performance capabilities not achievable in quantum well lasers[58].

In 2019, Justin et al. The gain bandwidth can designed to emit at a variety of near-infrared wavelengths and be either broad or narrow and Quantum dots for laser gain regions provide several advantages over quantum wells for photonic integration. Even when epitaxially grown on silicon at high dislocation densities, the extended device lifetimes are made possible by the high carrier confinement and areal dot density, which limit susceptibility to crystalline defects[59].

In 2020, Ali Gehad et al. The overall gain of the InTlAsSb quantum dot structure is investigated. Three quaternary thallium structures In_{0.85}Tl_{0.15}AsSb, In_{0.93}Tl_{0.07}AsSb, and In_{0.97}Tl_{0.03}AsSb are chosen to study the nonlinear influence of the injected signal power. The gain peak was increased by four times and the wavelength was shifted to longer one for the In_{0.97}Tl_{0.03}AsSb quantum, additionally covered is the nonlinear behaviour of these QD structures[60].

In 2021, Bozhang. Examining the nonlinear dynamics and characteristics of QD lasers on Si for PIC applications is the aim of this research. examined how epitaxial QD lasers on Si behave when exposed to external optical feedback (EOF). The QD laser provides additional information for creating isolator-free PICs because of its remarkable resilience against parasitic reflections in the short-cavity domain. To accomplish this, a nearly zero linewidth enhancement factor is also important[61].

In 2022, G.O. Kornyshov et al. Using quantum dots (0D), a number of InGaAs/GaAs lasers in the 1–1.3μm optical range have been studied. The lasing wavelength dependency on the layer gain constant is measured and analyzed across a broad range of pump currents. It is demonstrated that edge-emitting lasers without external

resonators may achieve a broader range of lasing wavelengths and have a far greater maximum optical gain than lasers based on quantum dots[62].

In 2023, Baqer et al. Under the assumption of inhomogeneous broadening, gain spectra of Cd_xZn_{1-x} Te/AlGaN undoped and doped quantum dot (QD) structures are examined at four Cd mole fractions (x = 0.25, 0.5, 0.75, 0.95). With increasing Cd concentration, the gain rises while the wavelength decreases because of the wider band discontinuities between the QD states; the impact of the QD size effect is also investigated[63].

In 2024, Huiwen et al. The co-doping approach is shown to offer robust high-temperature performance and a much lower threshold current density through the whole temperature range, Additionally, the rate equation simulation of the lasers reveals the enhancements in the doping schemes [51].

In 2025, Konstantinos et al. This study showed that InAs/GaAs-on-Si lasers can operate on native GaAs substrates with performance comparable to that of top-tier lasers. The III-V-on-silicon ridge-waveguide lasers that have been optimised exhibit high-temperature functioning up to 165 °C and a continuous-wave threshold current as low as 6 mA., lasers fabricated on both Si and GaAs substrates using x identical processes exhibit virtually identical average threshold current [64].

1.7 Aim of The Work

- 1) calculate the subband energy levels in the conduction band and the valence band. of Si QD.
- 2) calculate the subband energy levels in the conduction band and the valence band at differ (height, radius)
- 3) determine the subband energy levels in the conduction band and the valence band for barrier
- **4)** Study of the optical gain Si-QDL and explain the relationship between wavelength and optical gain.
- 5) Calculate the gain at change QD size height
- 6) Calculate the gain at change QD size radius
- 7) Calculate the gain at change SiO_x WL
- 8) study rate equation for system
- 9) Study carrier density probability for QD and WL
- 10) The relation between the power saturation dBm vs gain dB



Electronic properties of Si

2.1. Electronic Properties of Semiconductors

The electrons and holes in the conduction and valence bands, respectively, are primarily responsible for the electrical characteristics of semiconductors.

Nearly all holes and electrons are produced by thermally exciting electrons across the energy gap. When the quantity of electrons and holes in a semiconductor is equal, the semiconductor is said to be intrinsic.[65]

2.2. Theoretical Model

This chapter treats Si Semiconductor QDs as a quantum - quantum-disk with height (h) and radius (ρ). For the structures under study, this model is employed to compute the energy levels in the valence band (VB) and conduction band (CB). For instance, energy levels for Si / SiO_x QD-structure are calculated where Si is the QD material, Si is the wetting layer (WL) and SiO_x is the barrier layer. By using the parabolic band model to solve the Schrödinger equation, the energy levels of the quantum disc are found.

2.3. Quantum Disk Model

For the quantum disk with a radius (ρ) and height (h). The Hamiltonian in the cylindrical coordinates (ρ, φ, z) is given by [66]:

$$H = \left\{ -\frac{\hbar^2}{2m^*} \left[\frac{1}{\rho} \frac{\partial}{\partial \rho} \left(\frac{1}{\rho} \frac{\partial}{\partial \rho} \right) + \frac{1}{\rho^2} \frac{\partial^2}{\partial \varphi^2} + \frac{\partial^2}{\partial z^2} \right] + V \right\} \psi_{(\rho, \varphi, z)} \qquad \dots \dots [2.1]$$

If the separation of variables is assumed in the solution of the Hamiltonian, an approximate wave function of the quantum disk can be obtained by solving the well-known problems of the two-dimensional circular potential well in the ρ - ϕ

direction and the one-dimensional square potential well in the z direction. In the ρ - ϕ direction, we have a solution of the form

$$\psi_{(\rho,\varphi)} = \frac{i^{m\varphi}}{\sqrt{2\pi}} \begin{cases} C_1 J_m(p\rho) & \rho \le a \\ C_2 k_m(q\rho) & \rho > a \end{cases} \qquad \dots \dots [2.2]$$

$$\rho = \frac{\sqrt{2m_d^*(E_Z - V_d)}}{\hbar} \qquad \dots \dots [2.3]$$

$$q = \frac{\sqrt{2m_b^*(V_b - E_\rho)}}{\hbar} \qquad [2.4]$$

Where $m_d^* = m_d$ is the effective mass inside the disk and $m_b^* = m_b$ in the WL. In the same way, the electric potential is $V = V_d$ inside the disk and $V = V_b$ in the WL. When the variables are separated for the Hamiltonian, the well-known problems of the one-dimensional square potential well in the Z direction and the two-dimensional cylindrical potential well in the ρ - ϕ direction may be solved to produce an approximate wave function of the quantum disc.

After some mathematical manipulation from the corresponding wave function in the dot and the barrier, the constant p and q has the relation;

$$(pa)^{2} + \frac{m_d^*}{m_h^*} (qa)^2 = \frac{2m_d^*(V_b - V_d)a^2}{\hbar^2} \qquad \dots [2.5]$$

ing the boundary condition in which the wave function Ψ and its first derivative divided by the effective mass $\left(\frac{1}{m^*}\frac{d\Psi}{d\rho}\right)$ are continuous at the interface between the WL and the dot, we obtain

$$C_1 J_m(Pa) = C_2 K_m(qa)$$
[2.6]

$$C_1(P/m_d^*)J_m'(pa) = C_2(q/m_b^*)k_m'(qa)$$
[2.7]

Eliminating C1 and C2, we obtain the eigen-equation

$$\frac{pa'J'_m(p_a)}{m_d^*J_m(\rho a)} = \frac{q_a K'_m(q_a)}{m_b^*Km(q_a)} \qquad \dots \dots [2.8]$$

The quantized constants p and q can be obtained from a graphical solution based on Eqs. [2.5] and [2.8].[66]

if the potential in the disk is taken as $V_d=0$, the transverse eigen-energy E_ρ is obtained by:

$$E_{\rho} = \frac{h^2}{2} \frac{(pa)^2}{m_d^* a^2} \qquad \dots \dots [2.9]$$

The solution of the wave function for the Z-dependence is the same as that of a quantum well. The solution of the even wave function is expressed as

$$\Psi(z) = \begin{cases} c_3 e^{-\alpha} \left(|z| - \frac{h}{2} \right) & |z| \ge \frac{h}{2} \\ c_4 \cos(k_z z) & |z| < \frac{h}{2} \end{cases} \dots [2.10]$$

Where

$$k_z = \frac{\sqrt{2m^*(E_z - V_d)}}{\hbar}$$
 [2.11]

and

$$\alpha = \frac{\sqrt{2m^*(V_b - E_z)}}{\hbar} \qquad \dots \dots [2.12]$$

The constant k_z and α are related as:

$$\left(k_z \frac{h}{2}\right)^2 + \frac{m_d^*}{m_h^*} \left(\alpha \frac{h}{2}\right)^2 = \frac{2m_d^*(V_b - V_d)}{h^2} \left(\frac{h}{2}\right)^2 \qquad \dots \dots [2.13]$$

From the boundary condition referred above, we obtain

$$C_3 = C_4 \cos\left(k_z \frac{h}{2}\right) \qquad \dots \dots [2.14]$$

$$\frac{\alpha}{m_h^*} C_3 = \frac{k_z}{m_d^*} C_4 \sin\left(k_z \frac{h}{2}\right) \qquad [2.15]$$

Eliminating and C_3 and C_4 lead to the eigen-equation for the even wave function

$$\alpha = \frac{m_b^* kz}{m_d^*} \tan\left(k_z \frac{h}{2}\right) \qquad \dots \dots [2.16]$$

the longitudinal eigen-energy E_z is obtained by:

$$E_z = \frac{\hbar^2}{2m_d^*} \frac{(p \, h/2)^2}{\left(h/2\right)^2} \qquad \dots \dots [2.17]$$

The total eigen-energy of the quantum disk E_d is, approximately, the summation of the transverse and longitudinal eigen-energies, and expressed as

$$E_d = E_\rho + E_z$$
 [2.18]

The discrete energy levels of quantum dots vary with their size. The energy gap widens as the nanocrystal's size shrinks, producing a rainbow of colors that varies in size. The size of the dot, not the substance it is formed of, determines the emission photon's wavelength, The manufacturer may decide the wavelength of emission, which in turn defines the color of light that the human eye perceives, by manipulating the size of the quantum dot. The smaller the dot, closer it's to the blue end of the spectrum and the large the dot, closer to the red. The closer quantum dots are to one another, the more their optical characteristics will change [67]as shown in the figure 1.

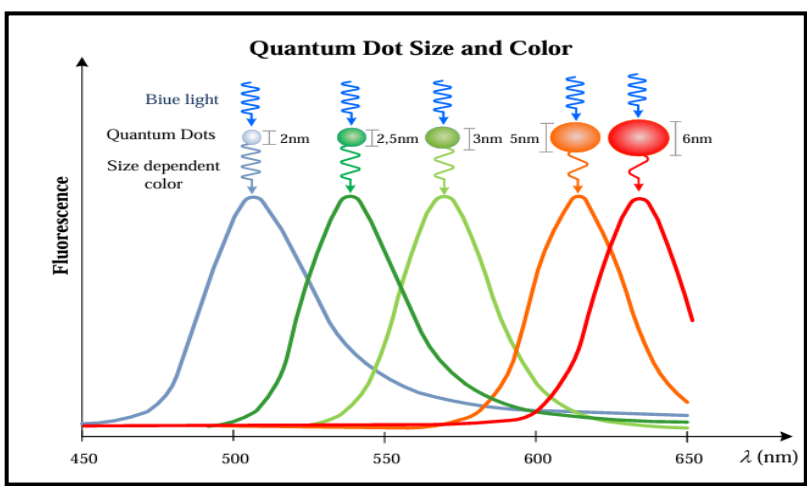


Figure 2.1 The Electronic Structure Of Quantum Dots Varies With The Size Of The Dot[68]

The figure (2.2) illustrates the energy band diagram of a structure composed of silicon quantum dots (Si-QDs) embedded between two layers of silicon dioxide (SiO₂ or SiO_x). This configuration represents a fundamental model widely used in

the design of quantum dot lasers, quantum dot light-emitting diodes (QD-LEDs), and optoelectronic conversion systems. The operating principle of this structure is based on the quantum confinement effect, which leads to the quantization of energy levels within the quantum dots and an increase in the effective bandgap compared to that of bulk silicon.

The structure consists of three main regions: Two insulating SiO₂ barrier layers at the top and bottom, and an active region in the middle containing the Si quantum dots. The SiO₂ layers serve as high-energy barriers with a large bandgap of approximately ~9 eV, which enables the confinement of both electrons and holes within the nanoscale silicon region. In contrast, the Si-QDs possess a smaller intrinsic bandgap (about 1.1 eV in bulk form), but this gap increases as the quantum dot size decreases due to the strong quantum confinement effect.

The active region (Si-QD) is the central part of the structure, where discrete energy levels are formed instead of continuous bands. The levels (E_{C1} , E_{C2} , E_{C3}) correspond to the quantized conduction states, while (E_{h1} , E_{h2} , E_{h3} , E_{h3}) represent the quantized valence states. In this region, electrons are injected from the upper n-type layer into the conduction levels, while holes are injected from the lower p-type layer into the valence levels. The radiative recombination between these carriers inside the quantum dots results in photon emission, where the photon energy corresponds to the transition energy difference according to:

$$E_{photon} = E_{Ci} - E_{h_j}$$

The Si/SiO₂ interface represents a semiconductor—insulator junction in which silicon dioxide forms large potential barriers for both electrons and holes. The conduction band offset (ΔE_C) is approximately 3.1 eV[69], and the valence band offset (ΔE_h) is about 4.5 eV[70]. These significant energy barriers effectively confine charge carriers within the Si-QDs, preventing leakage and enhancing radiative efficiency and optical stability.

Consequently, the Si-QD region serves as the core active zone of the device, where the optical and electronic properties can be engineered by controlling the quantum dot size, doping level, or barrier thickness. Such characteristics make silicon quantum dots embedded in SiO₂ a promising platform for nanoscale optoelectronic applications, including low-threshold quantum dot lasers and high-efficiency light-emitting diodes.

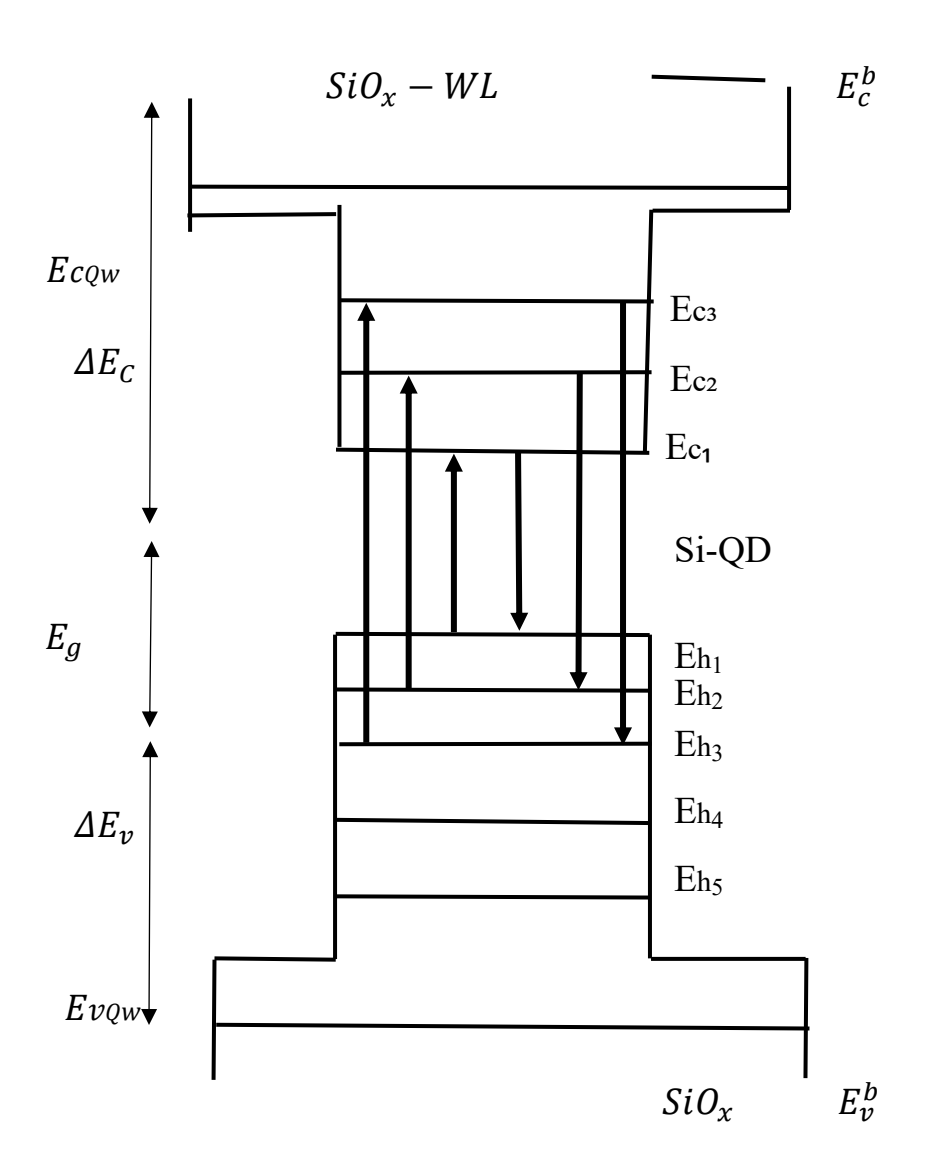


Figure 2.2. The Diagram Shows the Energy Levels Between The Valence Bands And The Conduction Bands In The Si/SiO_x in quantum dot And quantum well.

The presented table (2.1) provides a systematic study of the electronic structure of semiconductor quantum dots and their associated wetting layer, focusing on the effect of changing the geometric diameter of the quantum dot on the electronic energy levels. This study represents a theoretical or computational model aimed at understanding the relationship between nanoscale dimensions and the quantum properties of the material. The table covers four different diameters ranging from 8 nm to 16 nm, which constitute a critical range within the strong quantum confinement regime, where quantum effects become clearly observable and significant.

The data related to the conduction band energies of the quantum dots reveal a physically consistent behavior that aligns with the fundamental theory of quantum confinement. The first conduction energy level E_{CI} starts at 1.2521 eV for a diameter of 8 nm and gradually decreases to 1.2475 eV at 16 nm. This relatively small decrease—about 0.0046 eV as the diameter doubles—reflects the response of the conduction levels to size variation. The second and third levels (E_{C2} and E_{C3}) follow the same decreasing trend, exhibiting parallel shifts as the size increases. This behavior can be interpreted within the framework of the three-dimensional particle-in-a-box model, where the quantum state energy is inversely proportional to the square of the characteristic dimension of the box. For larger quantum dots, the confinement effect weakens gradually, leading to lower quantum energy levels that approach the values of the bulk material. An important observation is that the variation in conduction levels is relatively moderate compared to the valence bands, which reflects the relatively low effective mass of electrons in the conduction band of most semiconductors. Holes in the valence band possess a larger effective mass than electrons, making them more sensitive to quantum confinement effects.

Table 2.1 subband energy Levels for QD and WL at change dot size (radius effect ρ) for the Structure Si/SiO_x

Energy	$\rho = 8nm$	ho=10nm	$\rho = 12nm$	$\rho = 16nm$
Energy conduction subbands of (QD)	Ec ₁ =1.2521eV Ec ₂ =1.2791eV Ec ₃ =1.3280eV	Ec ₁ =1.2500eV Ec ₂ =1.2677eV Ec ₃ = 1.2997eV	Ec ₁ =1.2488eV Ec ₂ =1.2613eV Ec ₃ =1.2839eV	Ec ₁ = 1.2475eV Ec ₂ = 1.2475eV Ec ₃ = 1.2547eV
Energy valance subbands (QD)	Eh ₁ =0.0067eV Eh ₂ =0.0068eV Eh ₃ =0.0361eV Eh ₄ = 0.0887eV Eh ₅ =0.1647eV	Eh ₁ =0.0043eV Eh ₂ = 0.0044eV Eh ₃ =0.0232eV Eh ₄ =0.0571eV Eh ₅ =0.1060eV	Eh ₁ =0.0030eV Eh ₂ =0.0031eV Eh ₃ =0.0162eV Eh ₄ =0.0398eV Eh ₅ =0.0739eV	Eh ₁ =0.0017eV Eh ₂ =0.0017eV Eh ₃ =0.0092eV Eh ₄ =0.0225eV Eh ₅ =0.0418eV
Energy conduction subbands of (WL)	2.114 eV	2.1144 eV	2.1144 eV	2.1144 eV
Energy valance subbands of (WL)	6.6170 eV	6.6170 eV	6.6170 eV	6.6170 eV

The (2.2) illustrates the calculated subband energy levels for both the quantum dots (QDs) and the wetting layer (WL) at different quantum dot heights (h = 0.2 nm, 0.5 nm, 1 nm, and 1.5 nm). The purpose of this data is to investigate the influence of the geometrical size of the QDs on their electronic structure by examining the variation of energy levels within the conduction and valence bands.

In the first section of the table, the energy subbands of the conduction band within the QD (E_{Cl} , E_{C2} , E_{C3}) are presented. It is evident that these energy values gradually decrease as the QD height increases. For instance, (E_{Cl}) decreases from 1.9007 eV at h = 0.2 nm to 1.2934 eV at h = 1.5 nm. This trend clearly reflects the reduction of the quantum confinement effect with increasing QD size, as a larger quantum dot provides weaker carrier confinement, resulting in lower quantized energy levels.

the last section of the tables (2.1) (2.2) shows the energy subbands of the conduction and valence bands in the wetting layer (WL). These values remain constant at approximately 2.1144 eV and 6.6170 eV, respectively, suggesting that the WL is not significantly affected by changes in the QD dimensions, since it represents a relatively stable layer in the system.

Overall, the table demonstrates an inverse relationship between the QD size and the electron energy levels in the conduction band, a key factor in understanding and controlling the optical and electronic properties of quantum dots for various photonic and optoelectronic applications.

Table 2.2 subband energy Levels for QD and WL at change dot size (height effect h) for the Structure Si/SiO_x

high	h=0.2nm	h0.5nm	h = 1nm	h=1.5nm
	Ec ₁ = 1.9007eV	Ec ₁ = 1.5774eV	Ec ₁ = 1.3746eV	Ec ₁ = 1.2934eV
Energy valance	Ec ₂ = 1.9132eV	Ec ₂ = 1.5899eV	Ec ₂ =1.3872eV	Ec ₂ = 1.3059eV
subbands (QD)	Ec ₃ = 1.9358eV	Ec ₃ = 1.6125eV	Ec ₃ =1.4097eV	Ec ₃ = 1.3285eV
	Eh ₁ =0.0030eV	Eh ₁ =0.0030eV	Eh ₁ =0.0030eV	Eh ₁ =0.0030eV
Energy valance	Eh ₂ =0.0031eV	Eh ₂ =0.0031 eV	Eh ₂ =0.0031eV	Eh ₂ =0.0031eV
subbands (QD)	Eh ₃ =0.0162eV	Eh₃=0.0162eV	Eh ₃ =0.0162eV	Eh ₃ =0.0162eV
	Eh ₄ =0.0398eV	Eh ₄ =0.0398eV	Eh ₄ =0.0398eV	Eh ₄ =0.0398eV
	Eh₅=0.0739eV	Eh₅=0.0739eV	Eh₅=0.0739eV	Eh₅=0.0739eV
Energy conduction subbands of (WL)	2.1144eV	2.1144eV	2.1144eV	2.1144eV
Energy valance subbands of (WL)	6.6170eV	6.6170eV	6.6170eV	6.6170eV

The table (2.3) presents the energy values of subbands in both quantum dots (QD) and the wetting layer (WL) at different concentrations of the alloy component (x = 0.11, 0.15, 0.25, and 0.35).

The first section shows the energy conduction subbands of the quantum dots (E_{C1} , E_{C2} , E_{C3}), where the energy levels increase gradually with higher concentration values of x. This trend indicates a widening of the energy band gap as the content of the material with a larger band gap increases.

The second section displays the energy valence subbands of the quantum dots (E_{h1} – E_{h5}), which represent different quantized energy states of holes in the valence band. These energy values are relatively small and negative, showing a gradual increase with increasing x, which reflects the modification of the electronic structure of the quantum dots and the influence of composition on the valence band behavior.

In the third section, the energy conduction subbands of the wetting layer (WL) are listed, ranging from 2.2056 eV at x = 0.11 to 2.2156 eV at x = 0.35. This slight increase also suggests a moderate widening of the band gap as the alloy concentration rises. Finally, the fourth section presents the energy valence subbands of the wetting layer, with values ranging from 6.7024 eV to 6.7088 eV. These values are relatively high and nearly constant, indicating that the effect of alloy concentration on the valence band of the wetting layer is minimal compared to that in the quantum dots.

Overall, the table demonstrates that increasing the alloy concentration x leads to higher conduction band energies in both quantum dots and the wetting layer, with minor variations in the valence subbands. This behavior highlights the direct relationship between chemical composition and the electronic properties of the nanostructure

Table 2.3 subband energy Levels for QD and WL at change mole fraction (concentration effect x)for the Structure Si/SiO_x

Concentration	x = 0.11	x = 0.15	x = 0.25	x = 0.35
	Ec ₁ = 2.3218eV	Ec ₁ = 2.4605 eV	Ec ₁ = 2.4618 eV	Ec ₁ = 2.5143 eV
Energy valance	Ec ₂ = 2.3297 eV	Ec ₂ =2.4691eV	Ec ₂ = 2.4759 eV	Ec ₂ = 2.5268 eV
subbands (QD)	Ec ₃ = 2.3439 eV	Ec ₃ = 2.4846 eV	Ec ₃ = 2.5014 eV	Ec ₃ = 2.5514 eV
Energy valance subbands (QD)	Eh ₁ =0.0017 eV Eh ₂ =0.0018 eV Eh ₃ =0.0096 eV Eh ₄ =0.0235 eV Eh ₅ =0.0437 eV	Eh ₁ =0.0022 eV Eh ₂ =0.0023 eV Eh ₃ =0.0123 eV Eh ₄ =0.0304 eV Eh ₅ =0.0565 eV	Eh ₁ =0.0034 eV Eh ₂ = 0.0035 eV Eh ₃ = 0.0184 eV Eh ₄ =0.0452 eV Eh ₅ =0.0841 eV	Eh ₁ =0.0048 eV Eh ₂ = 0.0050 eV Eh ₃ = 0.059 eV Eh ₄ =0.0134 eV Eh ₅ =0.0963 eV
Energy conduction subbands of (WL)	2.2056 eV	2.2072 eV	2.2091 eV	2.2156 eV
Energy valance subbands of (WL)	6.7024 eV	6.7057 eV	6=7076 eV	6.7088 eV

Table 2.4 The values of important Parameters for Si and SiO₂[71]'[72]'[73]'[74]'[75]

parameter	Si	SiO ₂
Energy gap (eV)at 300k	1.12	8.9
Dielectric constant at 300k	$11.7 \varepsilon_0$	$3.9arepsilon_0$
Density(g/cm³)	2.32	2.2
Effective mass of electron (m_e)	$1.08*m_0$	$0.42*m_0$
Effective mass of hole (m_h)	$0.49*m_0$	$0.58*m_0$
The background refractive index	3.48	1.46



Optical Gain

3.1 Linear Optical Gain

The expression for the modal optical gain is [76]:

$$\Gamma g(\hbar\omega) = \Gamma \left[g^{(1)}(\hbar\omega) - \Gamma_3 g^{(3)}(\hbar\omega) |E_s|^2 \right] \qquad \dots \dots [3.1]$$

The terms Γ and Γ_3 are used in the modal, linear and nonlinear gain, respectively, as their optical confinement factors. E_s is the optical electric field of mode s. $g^1(\hbar\omega)$ represents the linear gain, $g^3(\hbar\omega)$ is refer to the third-order nonlinear gain suppression that resulted from the beating between the laser oscillating mode (s) and other modes. The self-organization mode produces size and shape variations in the QDs, which may be taken into account in the gain spectra for theory and experiment coinciding. To achieve this, the Lorentzian lineshape function and an inhomogeneous broadening function in the QD density of states D(E') for the optical transition energy E' are used.

The modal optical linear gain per QD layer of the self-organized QDs is then determined by multiplying the gain by the optical confinement factor, which denotes the advantageous portion of the gain is given by [76]:

$$\begin{split} \Gamma g^{(1)}(\hbar\omega) &= \Gamma C_0 \sum_i \int_{-\infty}^{\infty} dE' |M_{env}|^2 |\hat{e}. \, P_{cv}|^2 \times D(E') L(E', \hbar\omega) [f_c(E', F_c) - f_v(E', F_v)] \end{split}$$
[3.2]

where all of the radiative energy transitions are taken into consideration by calculating the summation i over the conduction and valence QD energy subbands. Depended the term $|\hat{e}.P_{cv}|^2$ is the QD momentum matrix element on the light polarization considered with \hat{e} is a unit vector in the polarization direction. The envelope function term $|M_{env}|^2$ is taken between the QD electron and hole energy states that have the same quantum numbers. Considering the parabolic form of the band, the momentum matrices of QDs are taken to be the same as those of QW near the zone center ($k_t = 0$) for heavy hole band and, are expressed as:

$$|\hat{e}.P_{cv}|^2 = \frac{3}{2}(M_b^2)$$
[3.3]

where the bulk momentum matrix element given by:

$$M_b^2 = E_p \frac{m_0}{6} \qquad[3.4]$$

And E_p is the optical matrix energy parameter, it is given by [77]:

$$E_{p} = \left(\frac{m_{0}}{m_{e}} - 1\right) \left(\frac{E_{g} \cdot (E_{g} + \Delta_{0})}{E_{g} + \frac{3}{2} \Delta_{0}}\right) \qquad [3.5]$$

Where Δ_0 is spin-orbit splitting energy, E_g is the energy gap of the QD and m_0 is the free electron mass.

$$C_0 = \frac{\pi e^2}{n_b c \varepsilon_0 m_0 \omega} \qquad \dots \dots [3.6]$$

Where n_b is the material background refractive index, c is the light speed in the free space, ε_0 is the free space permittivity, ω is the optical angular frequency and e is the electron charge.

The self-assembled QDs state density with inhomogeneous broadening is determined by [76]:

$$D(E') = \frac{s^{i}}{V_{dot}^{eff}} \frac{1}{\sqrt{2\pi\sigma^{2}}} exp\left(\frac{-(E' - E_{max}^{i^{2}})}{2\sigma^{2}}\right) \qquad[3.7]$$

 s^i represents the degree of degeneracy at each energy state of the QD. E_{max}^i

is the transition energy at the peak of QD distribution of the optical transition energy. σ is the spectral variance of the QD distribution. [76]

Using the quantum disc model to determine the energy states of the QDs after they have taken the shape of a disc [78]'[79]. Considering that the average height of QDs is h and their areal density is N_D .

$$V_{dot}^{eff} = h/N_D \qquad \qquad \dots \dots [3.8]$$

Table 3.1 Radius ρ undoped for the Structure Si/SiO_x

Radius (p)	wavelength(λ)	Gain (1/cm)
ρ =8nm	498 nm	$2.927 \times 10^3 cm^{-1}$
ho =10nm	501nm	$1.85 \times 10^3 cm^{-1}$
ρ =12nm	503nm	$1.443 \times 10^3 cm^{-1}$
ρ =16nm	505 <i>nm</i>	$580cm^{-1}$

Table 3.2 Radius ρ p-type for the Structure Si/SiO_x

Radius (ρ)	wavelength(λ)	Gain (g)
$\rho = 8$ nm	498 nm	$6.56 \times 10^3 cm^{-1}$
ρ =10nm	501nm	$4.26 \times 10^3 cm^{-1}$
ρ =12nm	503 <i>nm</i>	$3.31 \times 10^3 cm^{-1}$
ρ =16nm	505nm	$1.34 \times 10^3 cm^{-1}$

Table 3.3 Radius ρ n-type for the Structure Si / SiO_x

Radius (ho)	wavelength(λ)	Gain (g)
ρ =8nm	498 nm	$5.86 \times 10^3 cm^{-1}$
ρ =10nm	501nm	$3.71 \times 10^3 cm^{-1}$
ρ =12nm	503 <i>nm</i>	$2.83 \times 10^3 cm^{-1}$
ρ =16nm	505nm	$1.29 \times 10^3 cm^{-1}$

Table 3.4 High h undoped for the Structure Si / SiO_x

wavelength(λ)	Gain (g)
	2 4
663.75 <i>nm</i>	$1.147 \times 10^3 cm^{-1}$
800.714 <i>nm</i>	$1.53 \times 10^3 cm^{-1}$
923.75 <i>nm</i>	$1.765 \times 10^3 cm^{-1}$
983.333nm	$1.868 \times 10^3 cm^{-1}$
	663.75nm 800.714nm 923.75nm

Table 3.5 High h n-type for the Structure Si / Sio_x

High(h)	wavelength(λ)	Gain (g)
h=0.2nm	661.429nm	$1.367 \times 10^3 cm^{-1}$
h=0.5nm	794.805nm	$1.878 \times 10^3 cm^{-1}$
h=1nm	914 <i>nm</i>	$2.157 \times 10^3 cm^{-1}$
h=1.5nm	972.5nm	$2.287 \times 10^3 cm^{-1}$

Table 3.6 High h p-type for the Structure Si / SiO_x

High(h)	wavelength(λ)	Gain (g)
h=0.2nm	660.976nm	$1.5\times10^3 cm^{-1}$
h=0.5nm	798.182 <i>nm</i>	$1.95 \times 10^3 cm^{-1}$
h=1nm	916.364nm	$2.25\times10^3cm^{-1}$
h=1.5nm	978.049 <i>nm</i>	$2.375 \times 10^3 cm^{-1}$

Table 3.7 different mole fraction x for barrier layer undoped for the structure Si/SiO_x

mole fractions	wavelength(λ)	Gain (g)
x = 0.35	630 nm	$519cm^{-1}$
x = 0.25	580 nm	$509cm^{-1}$
x = 0.15	539nm	$598cm^{-1}$
x = 0.11	493nm	$599cm^{-1}$

Table 3.8 different mole fraction for barrier layer n-type for the Structure Si/SiO_x

mole fractions	wavelength(λ)	Gain (g)
		,
x = 0.35	630 nm	$731.23cm^{-1}$
x = 0.25	580 nm	$719.56cm^{-1}$
x = 0.15	539nm	$796.431cm^{-1}$
x = 0.11	493nm	$797.75cm^{-1}$

Table 3.9 different mole fraction for barrier layer p-type for the Structure Si / SiO_x

mole fractions	wavelength(λ)	Gain (g)
x = 0.35	630 nm	$728.11cm^{-1}$
x = 0.25	580 nm	$778cm^{-1}$
x = 0.15	539nm	$819.52cm^{-1}$
x = 0.11	493nm	$800cm^{-1}$

Table 3.10 values the optical gain and wavelength for different carrier surface density of structure Si / SiO_x

carrier density	wavelength(λ)	Gain (g)
14 2		
$n_{2D} = 1.2 \times 10^{14} \ cm^{-2}$	685 nm	$322~cm^{-1}$
$n_{2D} = 3.2 \times 10^{14} cm^{-2}$	665 nm	$1000 \ cm^{-1}$
$n_{2D} = 5.2 \times 10^{14} \ cm^{-2}$	664nm	$1225 \ cm^{-1}$
$n_{2D} = 7.2 \times 10^{14} \ cm^{-2}$	662 nm	$1455 \ cm^{-1}$

3.2 Simulation Results and Discussion

The linear optical gain can be derived using the equation of motion of the density matrix with the perturbation approach.

In this chapter, we theoretically investigate of the linear optical gain characteristics of QD-L, focusing on the linear optical gain mechanisms. The optical gain suppression due to coherent and incoherent the total carrier density depletion (TCDD) in the active region modeled by the shift of the global quasi-Fermi level, is not including here since it appears when there is an input single (here $P_S = 0$).

3.2.1 Quantum Size Effect (QDL Height)

Figure 3.1 shows the plots of (Gain 1/cm) versus wavelength (height from h=0.2 nm, h=0.5 nm, h=1nm to h=1.5 nm), the disc height QD-L size effect on the gain, the dot height as a parameter. Figure 3.1(A) un-doped Si/SiOx system, shorter wavelength and gain less are obtained by decreasing QDL size height. For every 0.5 nm drop in height, the wavelength is shortened by about 60 nm and the gain is decrease by 100 cm⁻¹. The gain peak increases and shifted to longer wavelength with increasing Si/SiOx QD-L height size. where the wavelength is initially in the visible region (660 nm) and then moves to the infrared (980 nm).

Fig. 3.1(B) explain p-type doped for QD-L size (height), the gain is same or very small change and shifted to longer wavelength with increasing dot height A comparison done in Table (3.6) shows that the main change in the spectrum is obtained by changing disc height in the QD-L layer. This is due to reducing barrier potential in the dot layer, i.e. increasing carrier confinement for the overall system. when QD height in the layer increased by (0.5 nm), the wavelength is green solid line shifted by ~80 nm, we assume that the homogeneous linewidth due to gain recovery is the same as the linewidth due to pure dephasing.

Fig. 3.1(C) n-type doped at different system the experimental and theoretical observations where it is found that the variation between conduction- valence- band ground state energies is more sensitive to the height fluctuation than the change of base. red dash line gives lower gain and shorter wavelength than other spectra (green dash line, blue dash line, black dash line) due to QD size effect (where at decrease dot height) while black dash line have bigger gain and longer wavelength shift for red dash line compared blue dash line, we noted when increase.

The physical explanation for the increase in wavelength is due to the following relationship:

$$E = \frac{hc}{\lambda} \qquad \dots [3.9]$$

As the size of the quantum dot increases, it leads to a decrease in quantum confinement, meaning that the energy gap decreases and thus the wavelength increases. The physical explanation for the increase in gain when the size of the quantum dot increases is that when the density of DOS states increases, this means that the number of allowed transitions between electrons and holes increases.

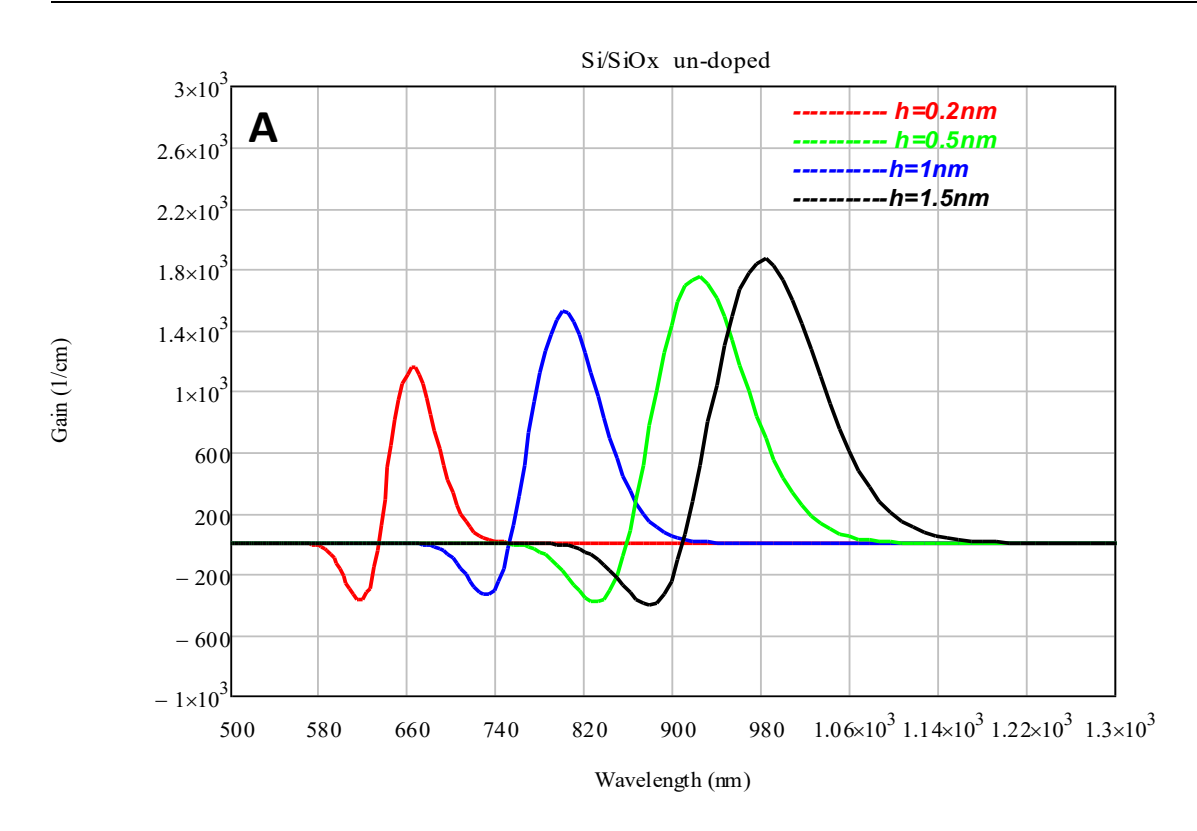


Figure 3.1(A): Calculated Gain Spectra at Different Values Of, QD-L Disc Height for Structure Si/SiO_x, Spectra of an un-doped Structure is dash line

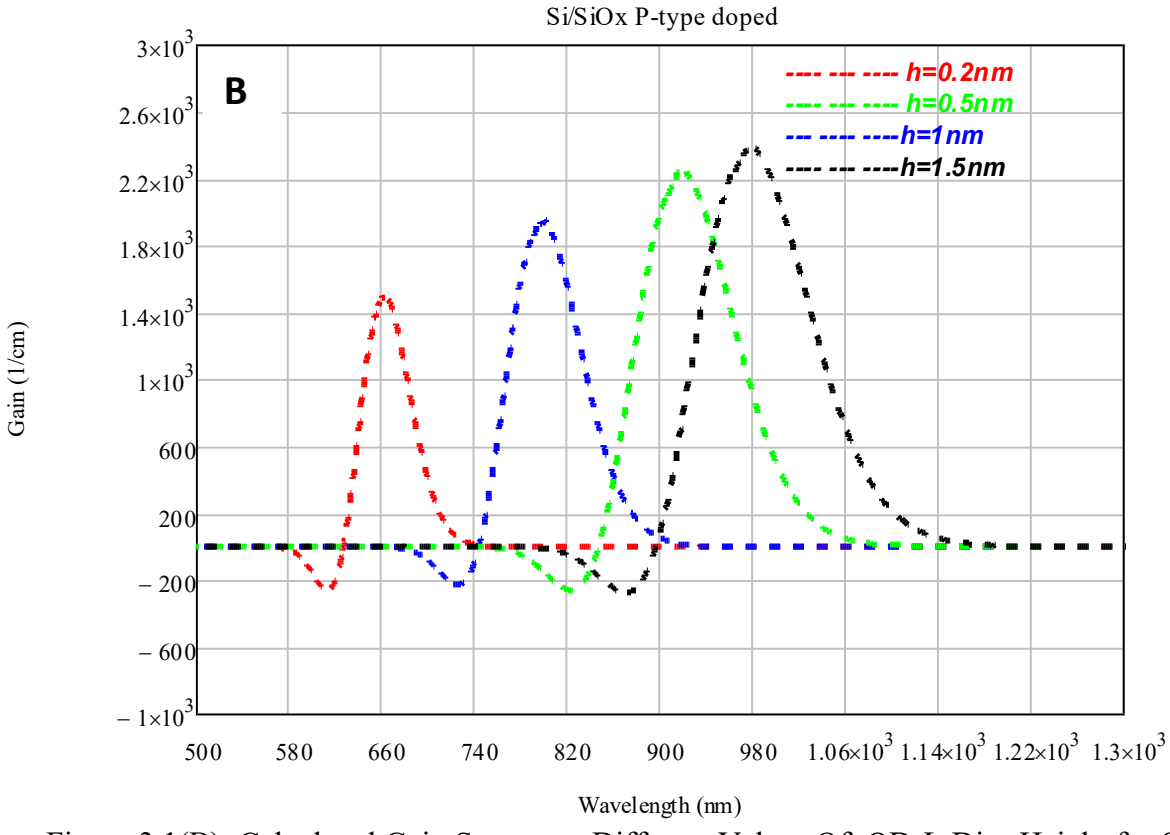


Figure 3.1(B): Calculated Gain Spectra at Different Values Of, QD-L Disc Height for Structure Si/SiO_x, P-type doped Structure is solid line

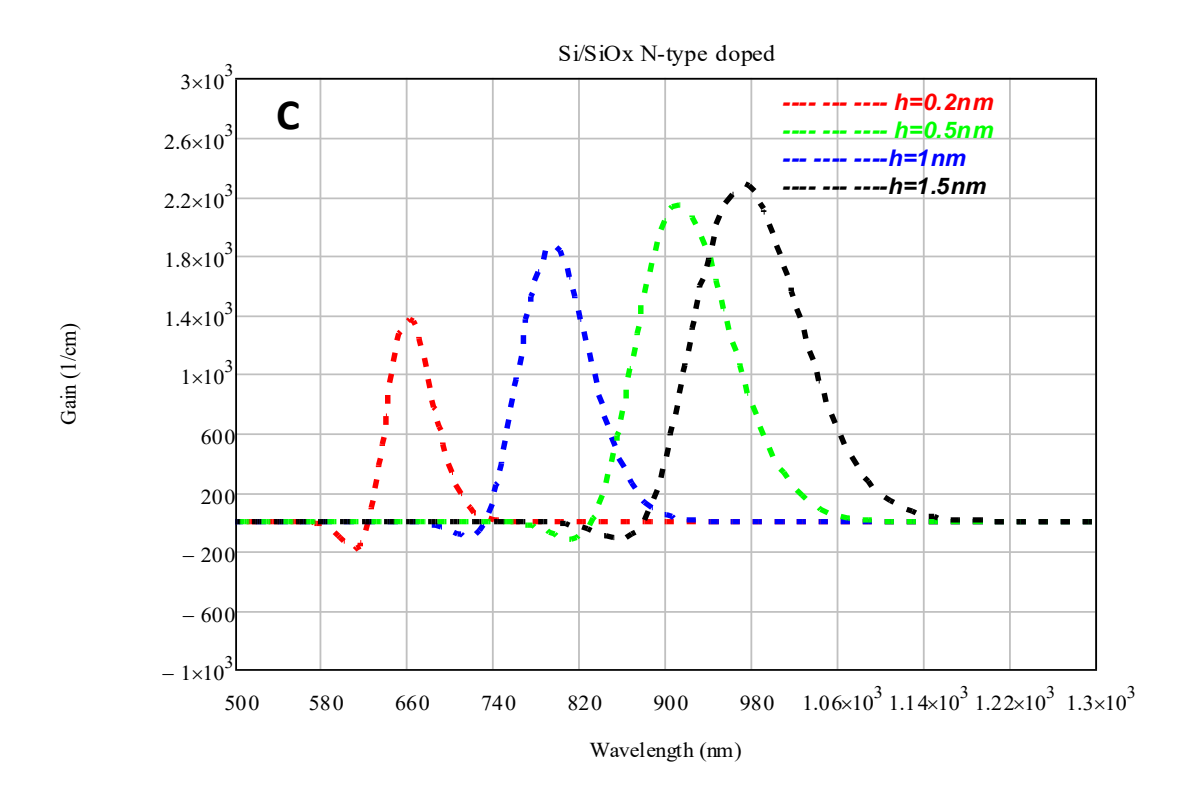


Figure 3.1(C): Calculated Gain Spectra at Different Values Of, QD-L Disc Height for Structure Si/SiO_x, N-type doped structure is solid line

3.2.2 Quantum Size Effect (QD-L Radii)

Figure. 3.2 show that disc radius QDL size effect on gain-wavelength relation (ρ =8 nm, ρ =10 nm, ρ =12 nm and ρ =16 nm). where at increase QDL radius (ρ =8 nm) the gain lower and shift wavelength amount (7 nm) to right, Fig. 3.2 (a) show that gain value for black line curve is (580cm⁻¹) when radius QD is (ρ =16 nm), while the gain value for red line spectrum is bigger (5 times) from black line curve and lower wavelength. The impact of altering the quantum disc radius where there is a slight change in the wave length is depicted in Figure 3.2 The gain increases by about 200 cm⁻¹ for every 1 nm increase in the disc radius, which is the only variation that can be taken into account.

Fig. 3.2 (A) shows the gain spectra of undoped QD radii of Si/SiO_x. This is in line with theoretical and experimental findings that show[80] that the difference between valence- and conduction-band ground state energies

Fig. 3.2 (B) illustrate p-type doped for QD radii of Si/SiO_x, for the doped structure, one peaks have the differ height. The bandwidth of the doped peaks is reduced for higher transition peaks. The gain is so high. The spectrum covers 460-550 nm wavelength.

Fig. 3.2 (C) show the gain spectra versus wavelength for n-type system When radius concentration is increasing from 8 to 16 nm, the peak gain in both TE and TM reduced by 3 times. A neglected change in the wavelength with this few change in the SiO_x in the WL.

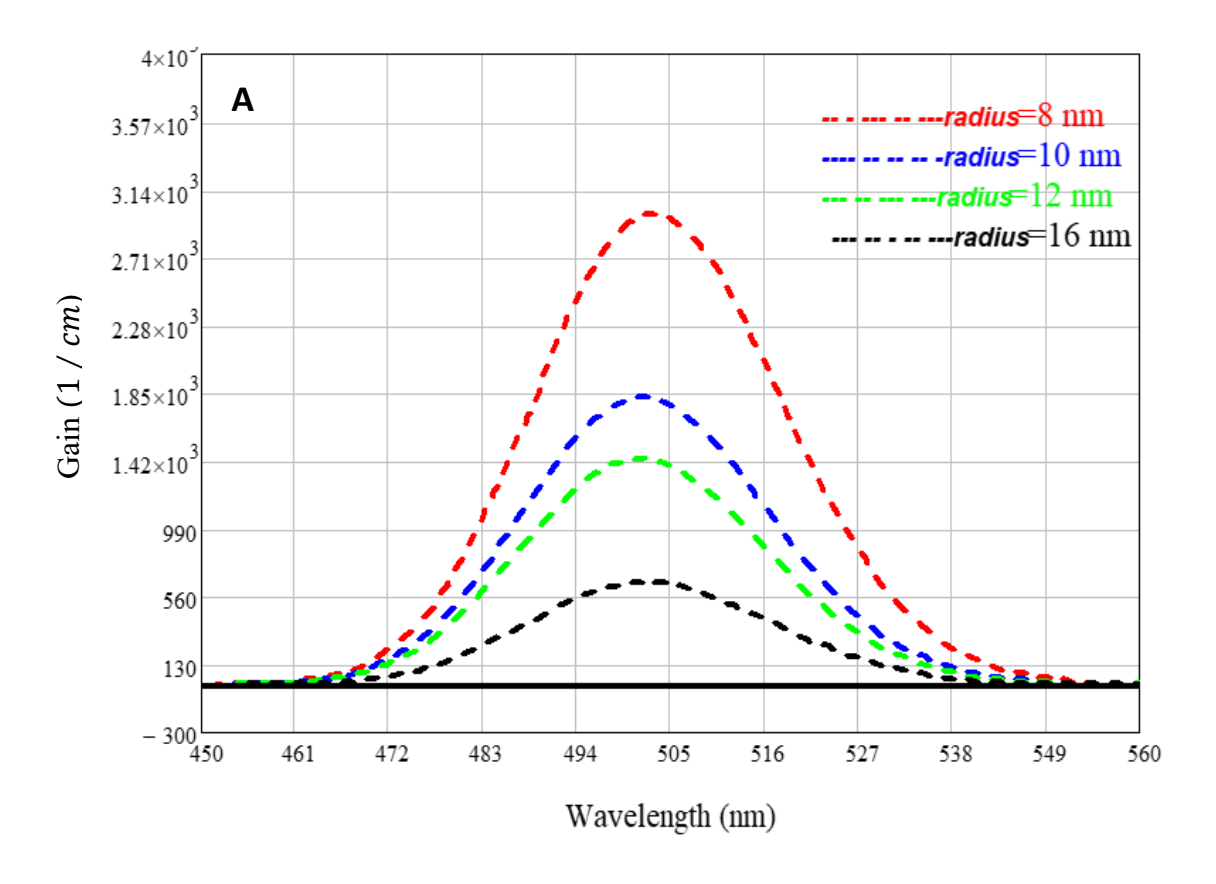


Figure 3.2(A): Calculated Gain Spectra at Different Values Of, QDL Disc Radii for Structure Si/Siox, Spectra of an Undoped structure is dash line

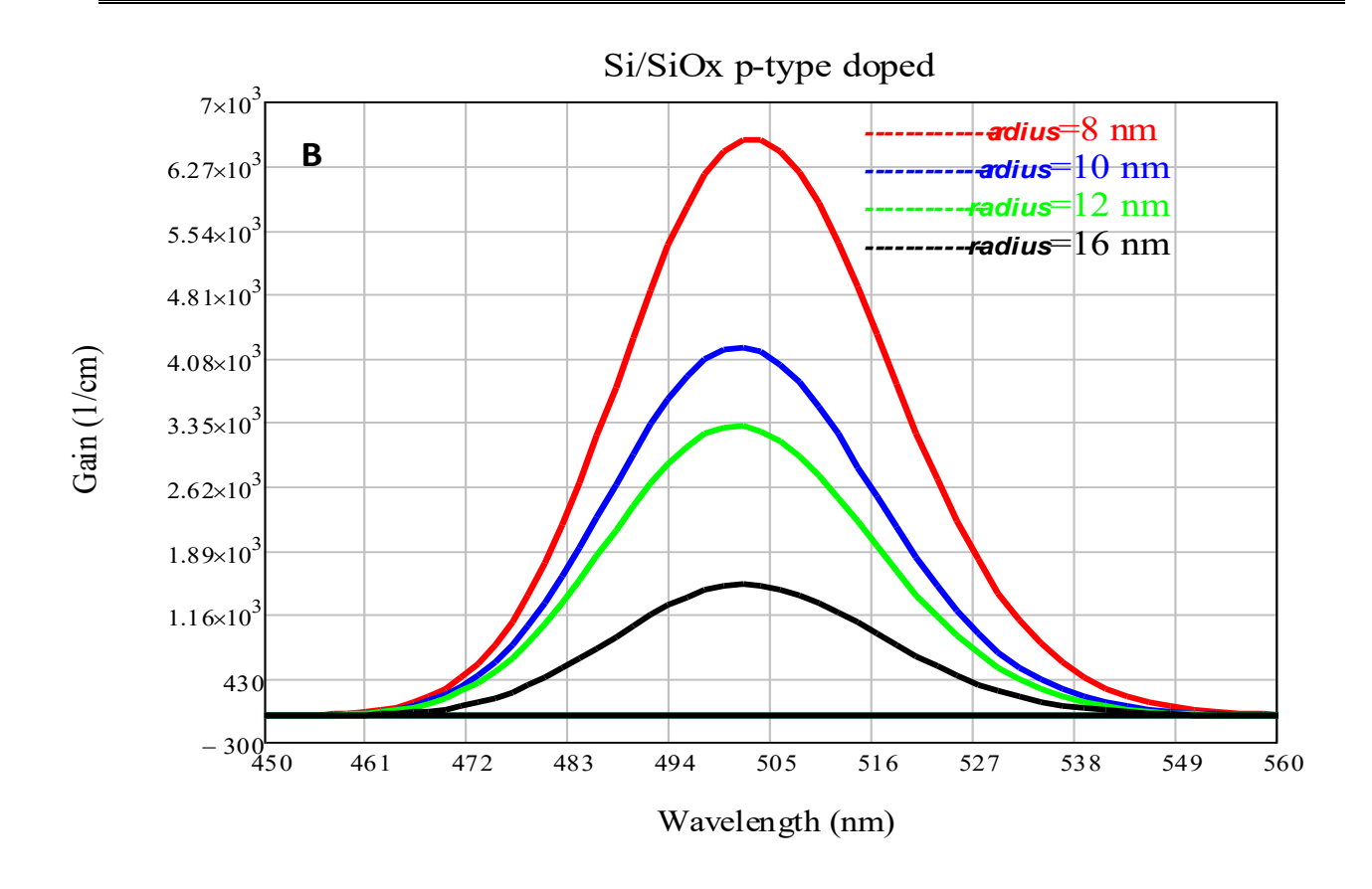


Figure 3.2(B): Calculated Gain Spectra at Different Values Of, QDL Disc Radii for Structure Si/Siox, p-type

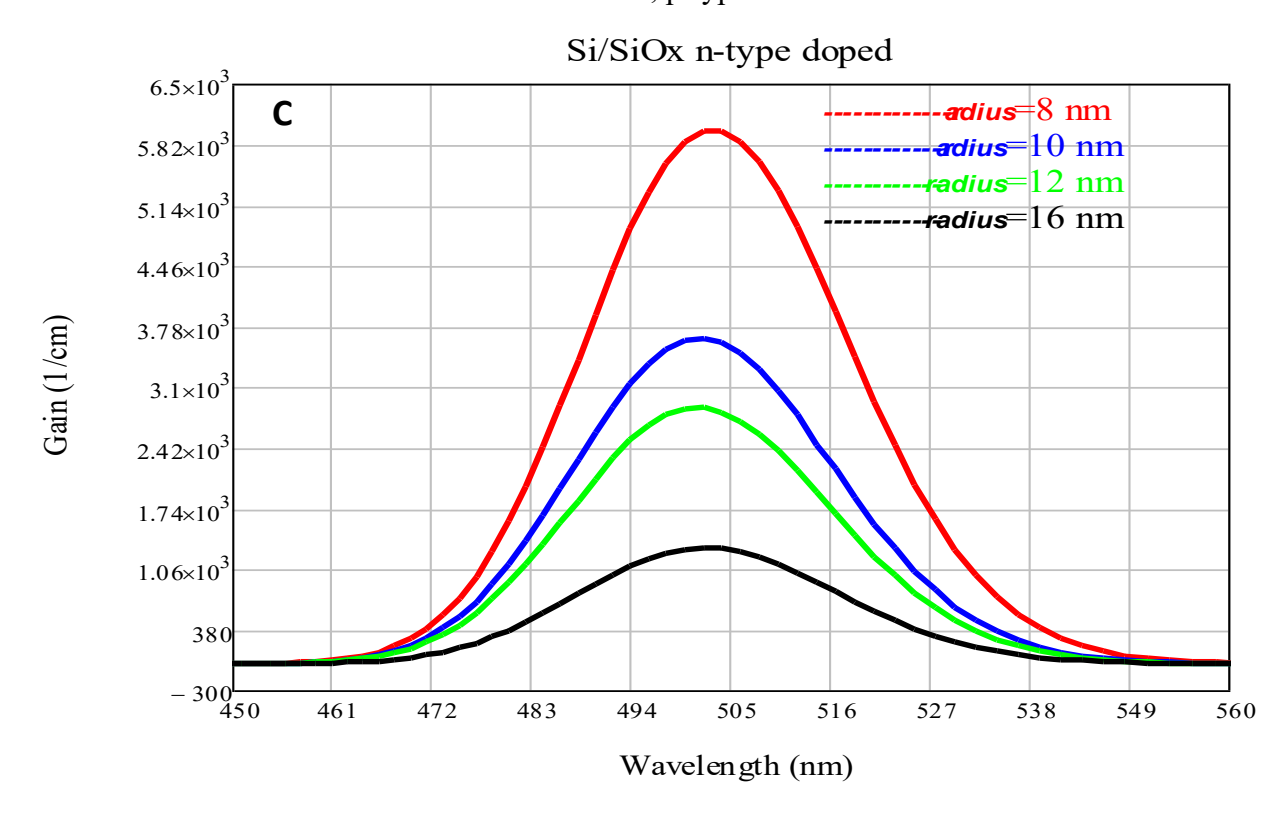


Figure 3.2(C): Calculated Gain Spectra at Different Values Of, QDL Disc Radii for Structure Si/Siox, Doped and n-type doped structure is solid line.

3.2.3 Concentration Effect WL

Figure 3.3: shows gain curves vs wavelength for Si/SiO_x , system, at different concentrations in the SiO_x WL layer (mole fractions in the WL), the gain for four SiO_x -mole fractions, (0.11, 0.15, 0.25 and 0.35). The gain peak reduced and shifted to down (absorption) for tow curve (green solid line and black solid line) with increasing SiO_x concentration in the WL.

Fig 3.3 (A) Undoped Si/SiO_x Structure. In the undoped structure, the gain is relatively low compared to doped samples. At higher oxygen content (x = 0.35), the gain is only 519 cm⁻¹, corresponding to a longer wavelength (630 nm). As decreases to 0.15 and 0.11, the emission peak shifts toward shorter wavelengths (green-blue region) and the optical gain increases significantly. This enhancement can be attributed to the increase in silicon content, which strengthens quantum confinement and improves radiative recombination inside the silicon-rich SiO_x layer.

Fig 3.3 (B) The p-type doped samples show similar behavior to n-type ones but with slightly higher gain values. The maximum optical gain of 819.52 cm⁻¹ is obtained at x = 0.15, indicating that hole doping also plays an important role in enhancing radiative transitions. Although x = 0.11 gives a shorter wavelength, the gain slightly decreases due to increased non-radiative recombination or fast carrier trapping at higher silicon content. Thus, the optimal mole fraction is around x = 0.15, which provides the best trade-off between quantum confinement and carrier concentration.

Fig 3.3 (C) The n-type doped sample exhibits a noticeable increase in optical gain compared to the undoped case for all mole fractions. This is because electron doping enhances the population inversion, which is a key condition for achieving optical amplification. The spectral peaks in the figure shift progressively toward

shorter wavelengths as decreases, consistent with the widening of the energy bandgap. The highest gain value ($\sim 800 \text{ cm}^{-1}$) occurs at x = 0.11 and x = 0.15, where the overlap between electron and hole wavefunctions is optimal for stimulated emission.

The observed increase in optical gain with doping is mainly due to the improvement of carrier population inversion and the enhancement of radiative transition probability. Lowering the oxygen mole fraction reduces the oxide barrier, increases the silicon-rich region, and strengthens the carrier confinement effect. The blue shift of the emission peaks confirms the quantum confinement effect, where smaller potential wells or Si nanoclusters lead to a larger bandgap and higher energy transitions. The study demonstrates that the Si/SiO_x structure exhibits improved optical gain as the mole fraction decreases, with the highest gain achieved under p-type doping at x = 0.15. These results confirm that controlling both the oxygen mole fraction and the doping type are crucial factors for optimizing the optical properties of Si/SiO_x structures.

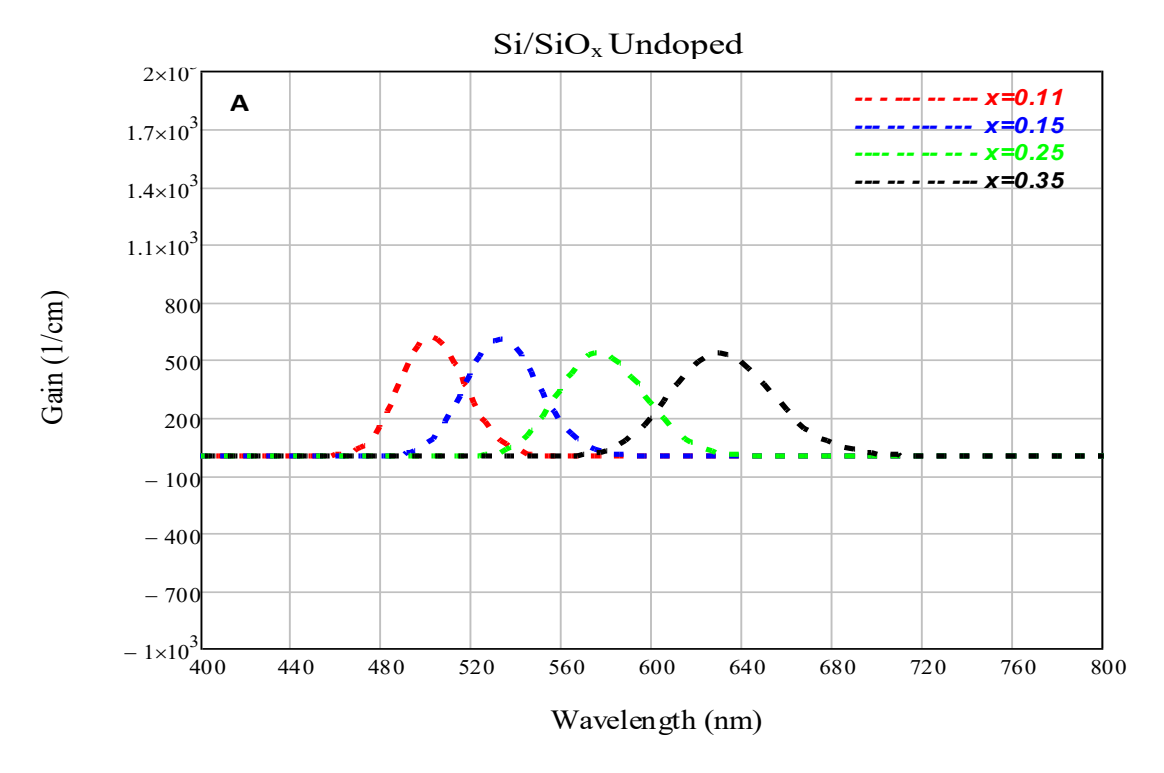


Figure 3.3(A): Calculated Gain Spectra at different values of, WL mole fraction for structure Si/Siox, spectra of an undoped structure is dash line

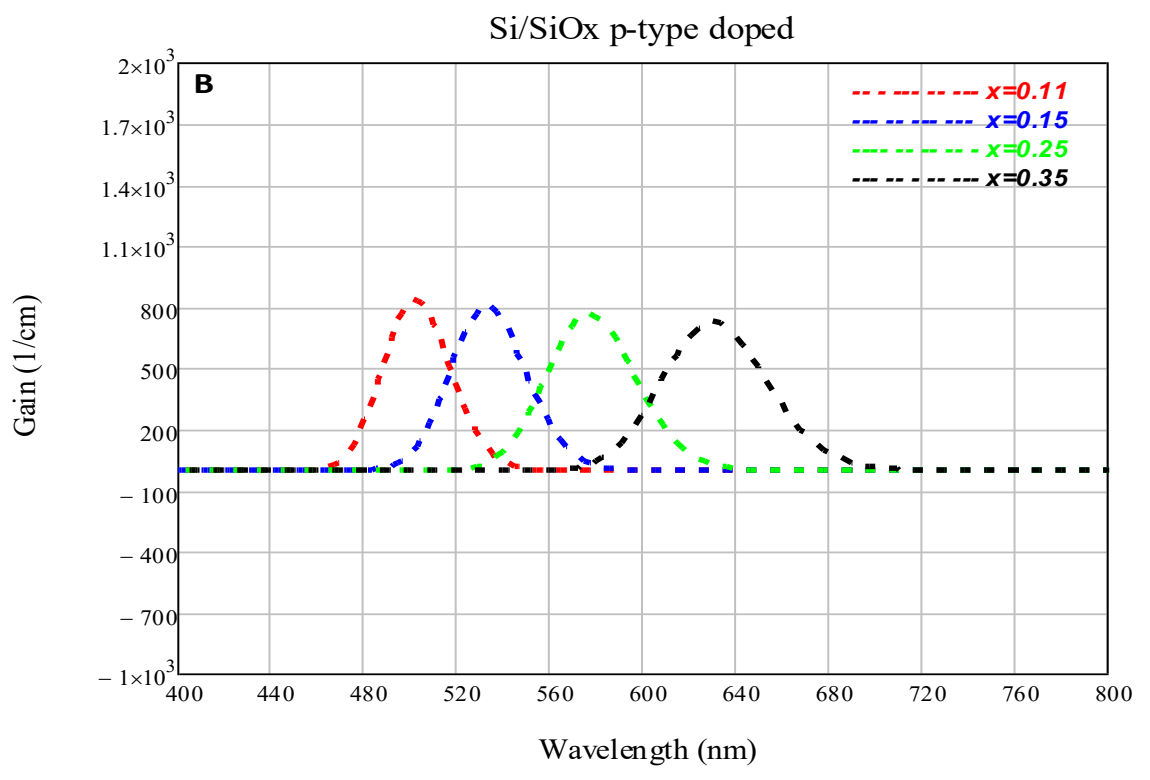


Figure 3.3(B): Calculated Gain Spectra at different values of, WL mole fraction for structure Si/Siox, p-type.

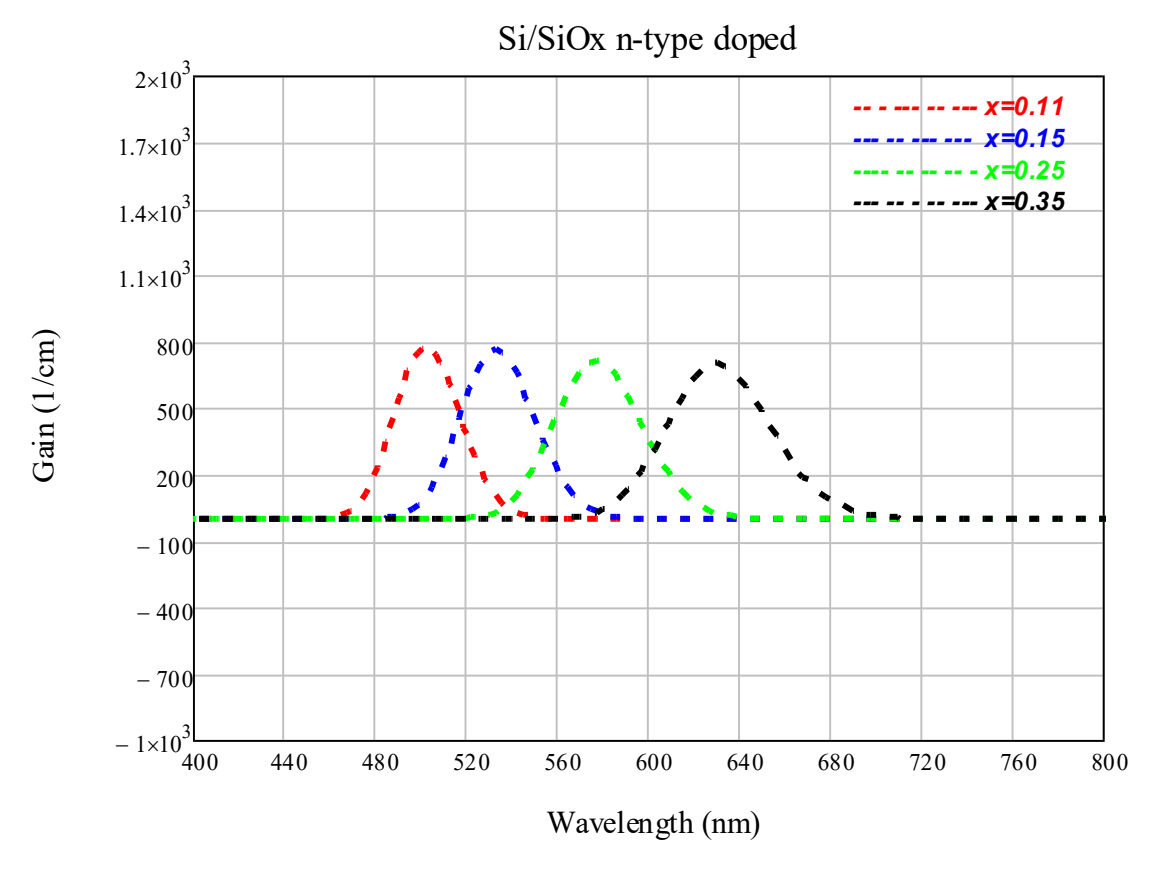


Figure 3.3(C): Calculated Gain Spectra at different values of, WL mole fraction for structure Si/Siox, doped and n-type doped structure is solid line.

Fig. 3.4 shows Si/SiO_x doped QD structures at different injection carrier current, show at increase injection current density.

Density from 1.2×10^{14} to 7.2×10^{14} cm⁻², a shift in the peak gain wavelength from 685 nm to 662 nm is observed. This shift is toward shorter wavelengths (Blue Shift). This blue shift is primarily attributed to two phenomena:

Band Filling Effect: At low injection levels, carriers (electrons and holes) occupy energy states closest to the conduction band minimum and valence band maximum, respectively. As carrier concentration increases, these lower energy states begin to fill, forcing subsequent recombination processes (photon emission) to occur between higher energy states, resulting in emission of photons with higher energy (and thus shorter wavelength) [81].

Burstein-Moss Shift: In heavily doped semiconductors or two-dimensional systems, the filling of certain energy states blocks electron transitions from the valence band maximum to the conduction band minimum (because these states are already occupied). Consequently, transitions must start from deeper levels in the valence band to higher levels in the conduction band, increasing the apparent band gap energy and causing the observed blue shift[82].

There is a strong direct proportional relationship between surface density and optical gain coefficient. The gain increases from 322 cm⁻¹ to 1455 cm⁻¹ with increasing n_{2D}. This behavior explains the concept of Population Inversion, which is the fundamental condition for optical gain and lasing to occur. Optical gain results when the rate of stimulated transitions (which emit photons) exceeds the rate of absorptive transitions (which absorb photons). This occurs only when the number of carriers in the upper energy state (conduction band) is greater than in the lower energy state (valence band) for a specific spectral region.

Increasing carrier concentration (n_{2D}) leads to an increase in the number of electrons in the conduction band and holes in the valence band. Upon exceeding a critical carrier density (known as Transparency Carrier Density), the population inversion condition is achieved for certain photon energies, and gain begins to appear.

With continued increase in n_{2D} , population inversion is achieved for a broader range of energies and the peak gain increases significantly, which is exactly what the data shows. The sharp rise in gain from 1000 to 1455 cm⁻¹ indicates that the system is entering an effective and practical gain region for laser applications.

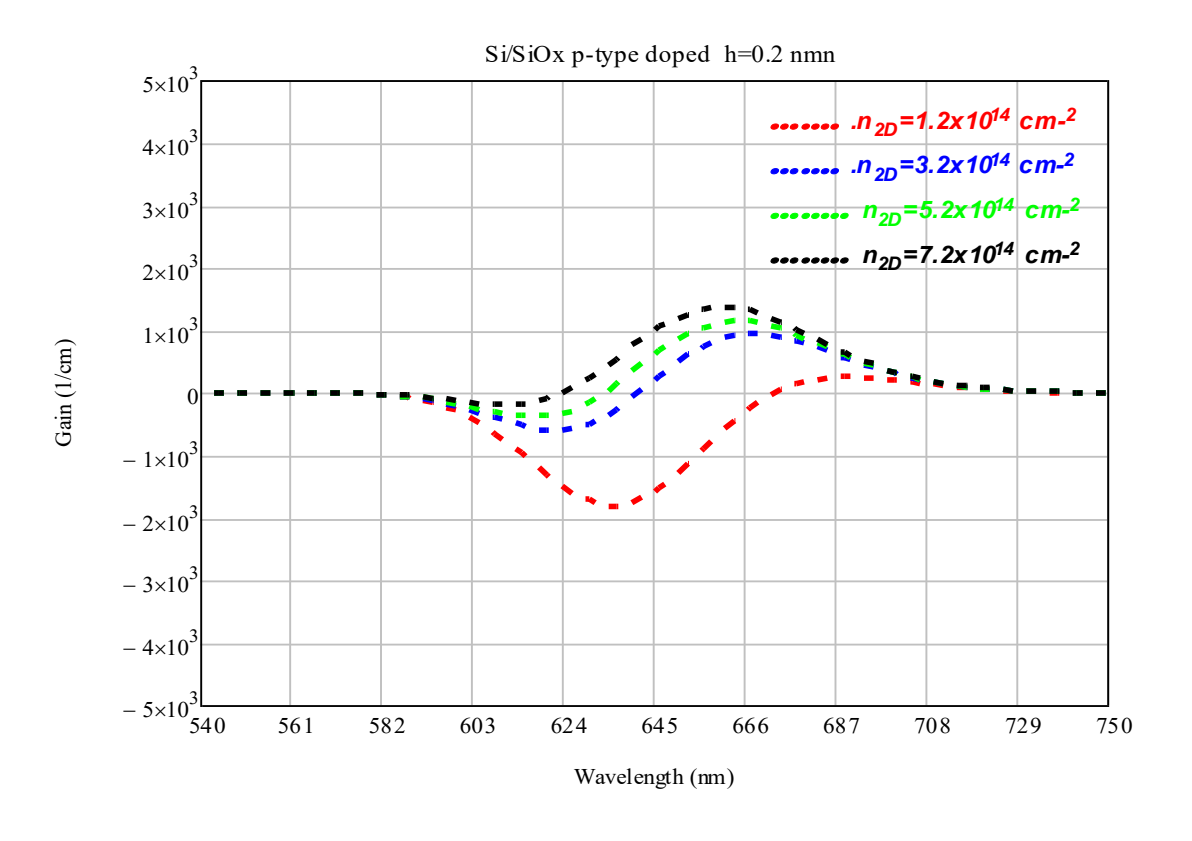
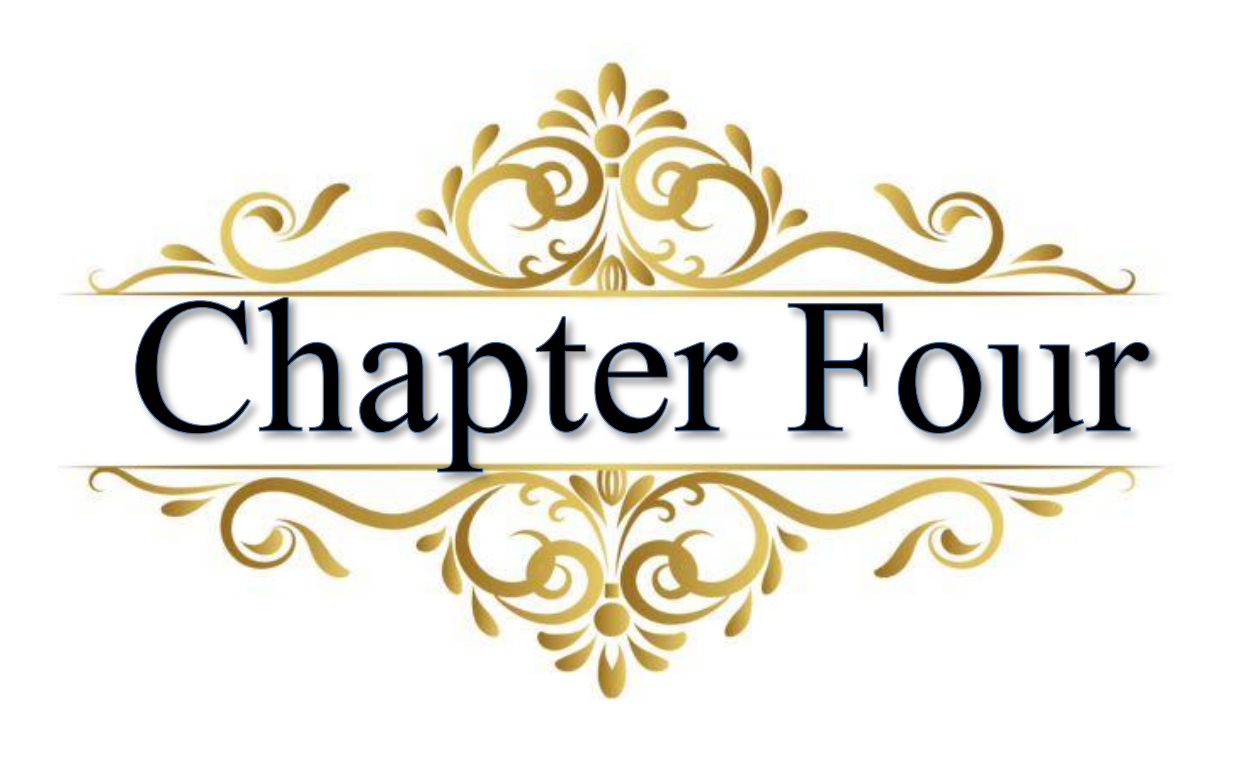


Figure 3.4: explain linear gain curves doped system Si/SiO_x at different injection current carrier concentration.



Dynamics Of Eelectron in Si QD-Laser

4.1. Rate Equation in Laser

This section introduces basic laser equations that explain the dynamics of laser oscillation.

Using a rate equation theory for clarifying the dynamical processes that take place in a laser; the rate equations match first-order differential equations. The four-level laser is treated. The idea is equally applicable to the three-level laser (where the pump level is identical as the top laser level) without any changes [19].

The physical processes that bind atomic groups to densities usually have very simple shapes, defined as spontaneous emission, stimulation, and absorption in the simplest sense.

Einstein created these equations in 1916 and used them to derive fundamental relationships between the coefficients of the spontaneous emission rate and the catalyst.[83]

$$A_{21} = \frac{2\pi v^2 e^2}{\epsilon_0 m_e c^3} \cdot \frac{g_1}{g_2} f_{12} \qquad \dots \dots [4.1]$$

$$B_{21} = \frac{e^2}{4\epsilon_0 m_e h v} \cdot \frac{g_1}{g_2} f_{12} \qquad \dots [4.2]$$

$$A_{21} = \frac{8\pi h v^3}{c^3} B_{21} \qquad \dots [4.3]$$

Where A_{21} , B_{21} The Einstein coefficients, n refractive index, c speed of light in a vacuum, v The frequency [83]

In the Centre of the four-level laser (Fig.4.1) is a two-level atomic system with the upper laser level 2 and the lower laser level 1. where after the process of absorption, which is the transfer of an atom from a lower energy level to a higher energy level, the atom will remain at the higher level for a period of time, and the

higher level may be able to relax to the lower level by a time called the (relaxation time τ_{21}). Pumping into the pump level (level 3) and fast relaxation leads to a population of the upper laser level. Relaxation depopulates the lower laser level (relaxation time τ_{12}). Thus, Systems engage with laser radiation through stimulated radiation absorption and emission[19].

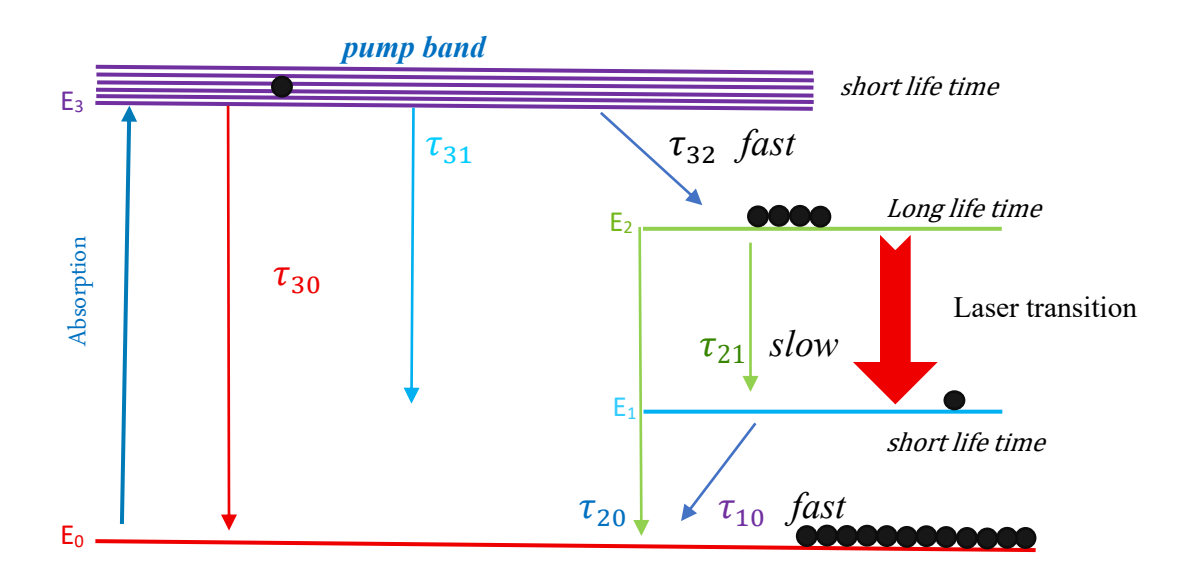


Figure 4.1 Four-level laser. Prepared by the researcher

It's crucial to remember that the only physical mechanism responsible for lasing is stimulated emission; one photon entering an atom results in twice as many photons with the same frequency leaving the atom. An avalanche of photons, a desired laser characteristic [84].

4.2. Rate Equation

In the three rate equations system, the barrier layer effect is disregarded and carriers are assumed to be injected with current density, J, in WL.

$$S_{AVE} = \frac{2\pi p_{inp} N_Q}{hw_p Ac} \qquad \dots [4.4]$$

This equation [4.1] expresses the average photon density or optical power inside the quantum laser[85].

$$\frac{\partial N_G}{\partial t} = \frac{g_{\text{max}}L}{N_O} N_{FE} (2N_G - 1) S_{\text{AVE}} \frac{c}{n_g} \Gamma - \frac{(1 - N_{FE})N_G}{\tau_{\text{FEG}}} + \frac{N_G (1 - N_{FE})}{\tau_{\text{GFE}}} + \frac{N_G^2}{\tau_{\text{GR}}} \quad [4.5]$$

In eq. [4.2] the rate of change of the number of electrons in the ground state. In this eq. describes how the number of electrons in the ground state change over time in QD-L[86].

$$\frac{\partial N_{FE}}{\partial t} = \frac{(1 - N_G)N_{FE}}{\tau_{FEG}} + \frac{N_G(1 - N_{FE})}{\tau_{GFE}} - \frac{N_W L_W (1 - N_{FE})}{N_Q \tau_{WSE}} - \frac{N_W L_W N_{FE}}{N_Q \tau_{SEW}} \qquad[4.6]$$

$$\frac{\partial N_{SE}}{\partial t} = \frac{(1 - N_G)N_{SE}}{\tau_{FEG}} + \frac{N_G(1 - N_{SE})}{\tau_{GFE}} - \frac{N_w L_w (1 - N_{SE})}{N_Q \tau_{WSE}} - \frac{N_w L_w N_{SE}}{N_Q \tau_{SEW}} \qquad[4.7]$$

In eq. [4.3], [4.4] the rate of change of the number of electrons in the first excited state and second excited state. This equations calculates the change in the number of electrons in the FES and SES, show the transition interactions between it and other energy level[87]'[88].

$$\frac{\partial N_{w}}{\partial t} = \frac{N_{w}N_{E}}{\tau_{SEW}} - \frac{N_{w}}{\tau_{WSER}} - \frac{N_{w}(1-N_{E})}{\tau_{WSE}} + \frac{JN_{E}}{eL_{w}} \qquad[4.8]$$

In eq. [4.5] the rate of change of the number of electrons in the wetting layer. This equation explains how the number of electrons in the wetting layer changes as a result of transitions and feedback from the injected current [88].

Where w_p is the energy of the signal at the peak, g_s single-pass gain, p_{inp} is the power of the input signal and c is the velocity of light in free space, A is the active region area, N_Q :number of quantum dots, L_W the effective thickness of the active layer, J is the injection current and N_W number of electrons in the wetting layer.

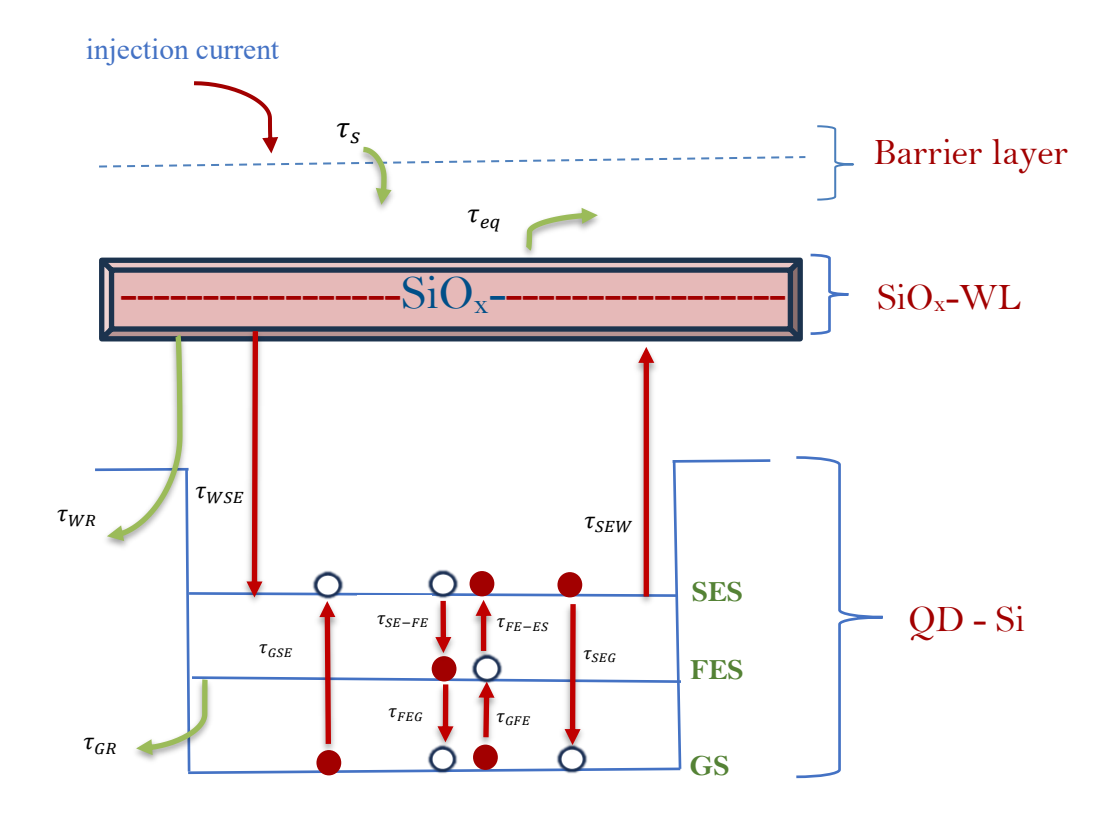


Figure 4.2 Levels scheme diagram of QD-Laser. Prepared by the researcher

Table 4.1 Parameters used in the calculations[89]'[90]'[91]'[92]'[93]

Parameter	Symbol	Value	Unit
Spontaneous radiative life time in QDs	$ au_{GR}$	0.4	ns
Spontaneous radiative life time in WL	$ au_{WR}$	1	ns
Carrier escapes time from SES to WL	$ au_{SEW}$	1	ns
Time transfer elections from high (barrier region) level to second level in QD-L	$ au_{WSE}$	3	ps
Time transfer elections from lower level to high level in QD-L	$ au_{\mathit{GFE}}$	1.2	ps
Carrier relaxation time from FES to GS	$ au_{FEG}$	0.16	ps
Diffusion time in the barrier layer	$ au_{\scriptscriptstyle S}$	6	ns
Separate confinement heterostructure	$ au_{sr}$	4.5	ns
Recombination			
Time rate for wetting layer	$ au_{qe}$	0.11	ns

interior wastage	a_{int}	2	Cm^{-1}
photonic parameter	Γ	0.007	
Laser length	L	2000	mm
The effective thickness of the active layer	L_{w}	0.2	mm
Surface density of QDs	n_Q	2× 10 ¹⁰	Cm^{-2}

4.3 Saturation Power Effect For (Si/SiO_x QD Laser)

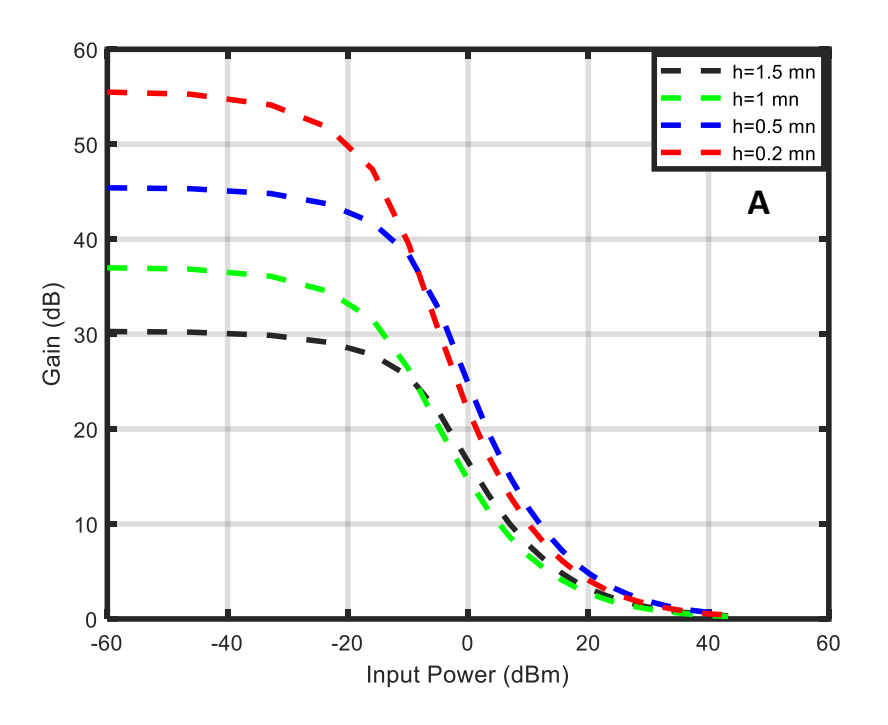
The saturation power is an amplifier's primary parameter that has a significant impact on both linear and non-linear characteristics and This optical power is known as the one that cuts the modal gain in half of the unsaturated gain[94]. Gain saturation is primarily brought on by carrier depletion, and as QDL pump current increases, so do the gain saturation power and gain saturation pulse energy[95].

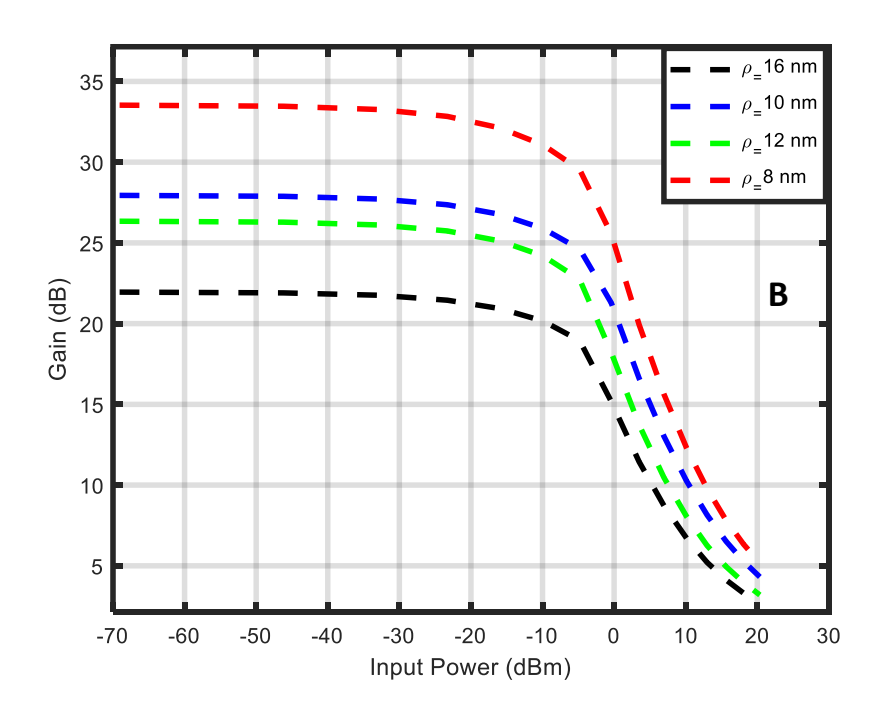
4.3.1 Saturation Input-Power Effect For (Si/SiO_x QD Laser)

Saturation input-power It refers to the power level at which the device's capacity to greatly amplify or absorb the signal and is used to describe the incident optical power level at which a saturable absorber or gain media begins to deviate from linearly. The output power no longer rises in proportion to the input power at this point, and the gain begins to fall as the input power rises [96].

Figure 4.3 input power-gain for Si/SiO_x Fig 4.3 (a) show that the change QD size (height from h=0.2 nm, h=0.5 nm, h=1 nm to h=1.5 nm), illustrate the effect disc height QDL size on input power-gain relation where we note high gain at height dot size at (8 nm) to its high bandgap, Fig 4.3 (b) illustrate the change radius QD size (from ρ =8 nm, ρ =10 nm, ρ =12 nm to ρ =16 nm), show that disc radius QDL size on input power-gain relation where low gain at radius QD size at (ρ =16)

because bigger to its low bandgap , and The relation input power-gain for the structure SiO_x is displayed in Figure (4.3)(c). with a greater gain at 0.11 O_x -mole fraction.





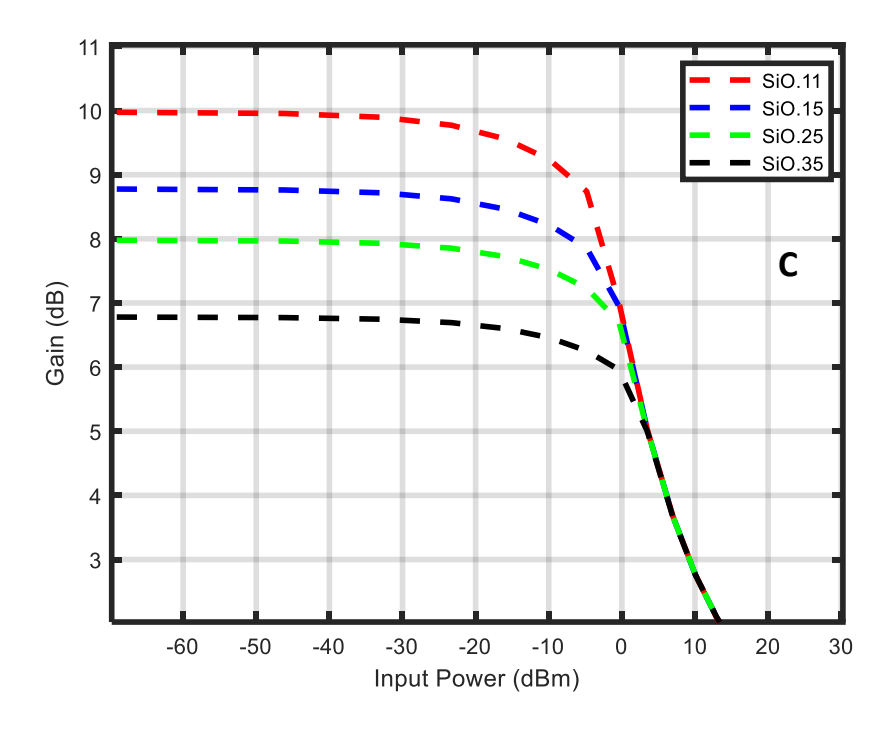


Figure 4.3: Calculated Gain-Input Power Relation at J=1.335 Ka/Cm² for the Structure Si/Sio_x, (A): The Disc Height for QDl (h), (B): The Disc Radius(ρ) for QDl and (C) Mole Fraction Sio_x WL.

4.3.2 Saturation Output-Power Effect For (Si/SiO_x QD Laser)

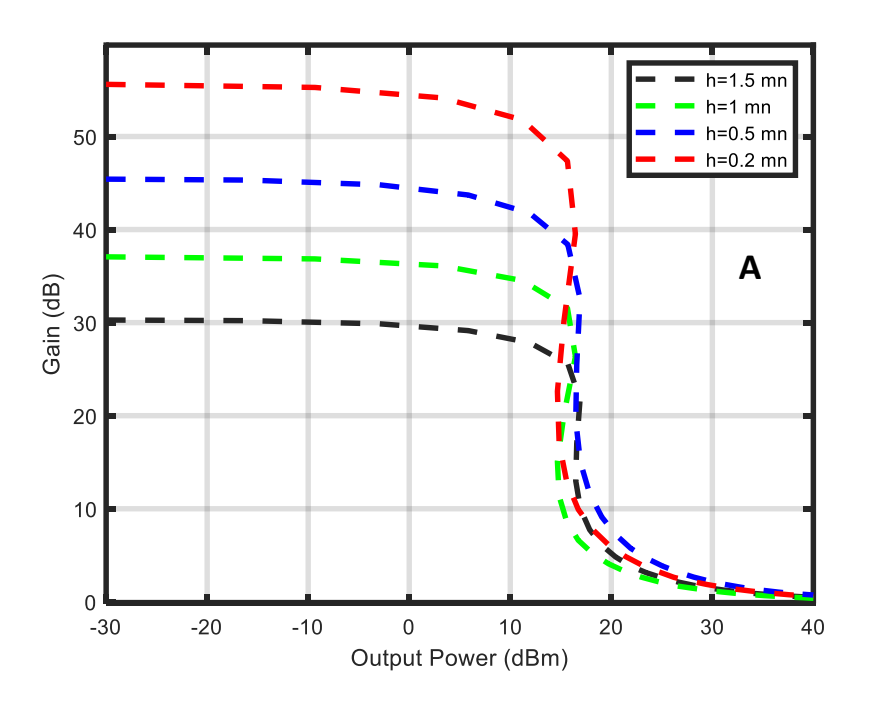
Output saturation power refers to the maximum output power an amplifier can deliver before its output no longer increases proportionally with the input signal. It's the point where the amplifier's gain begins to diminish, and do not lead to significant increases in output power, further increases in input power[97]'[98].

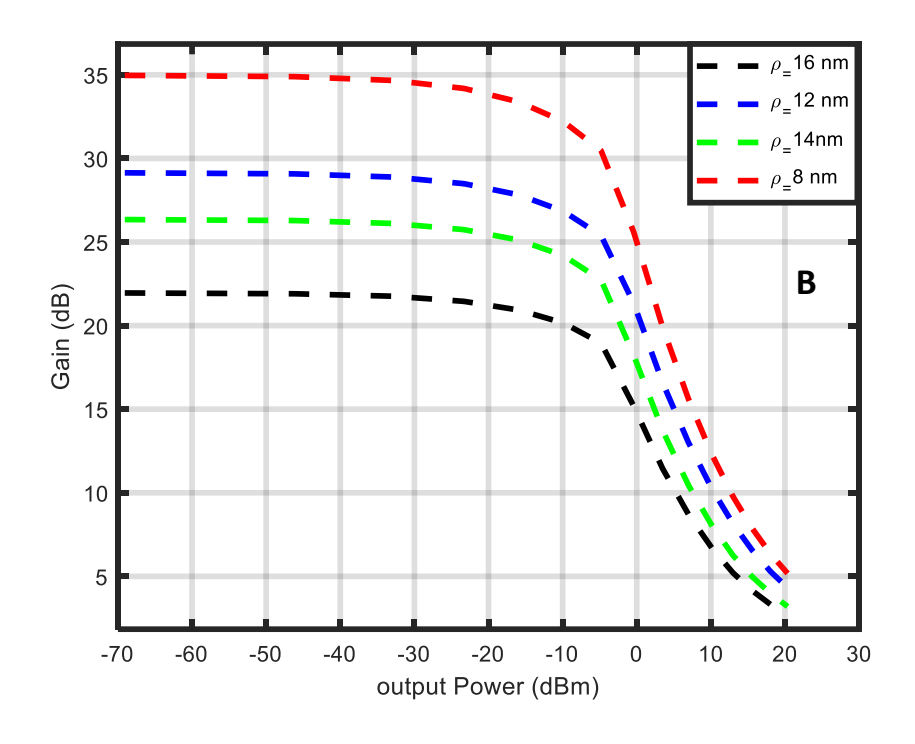
Figure (4.4) explained the effect QD-L size (radius, height for QD and mole fraction for WL) on input power-gain relation and mole fraction for wet layer SiO_x are shown in Fig. 4.4 (A), (B), (C), where the contribution due to changing SiOx-composition in WL is minor as in Fig. 4.4 (C). The output saturation power is calculated and stated in Table (4-3). Comparing these results with the measured values of some other QD-L, for example it is measured in [99] Fig. 4.4 (A) illustrate that QD-red dash line have a saturation power of 56 dBm, height QD-blue dash line

have a saturation power of 45 dBm, QD size -green dash line have a saturation power of 37 dBm and disc height (h=1.5 nm)-black dash line have a saturation power of 30 dBm, Here we get a saturation power until 20 dBm which in comparison with QDL shows a high value and confirms the prediction of high saturation power due to spatially distributed optical gain, the fast recovery time and the small confinement factor.

Fig. 4.4 (B) The gain saturates at low input power, then it declines at high input powers. This can be attributed to the carrier depletion in the QDs where the output power begins to increase.

Fig. 4.4 (C) saturation power of 15 dBm for black dash line have a low gain 7 dB while red dash line has high gain at 10 dB and more stability





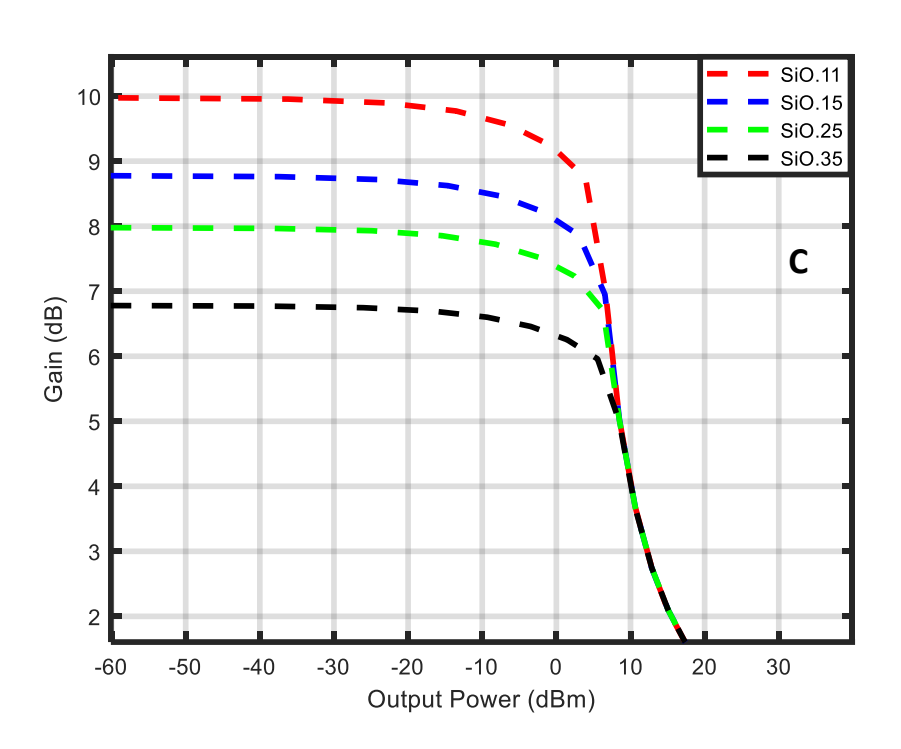


Figure 4.4: Calculated Gain-Output Power Relation At J=1.335 Ka/Cm² for the Structure Si/Sio_x, (A): The Disc Height (h), (B): The Disc Radius(ρ) And (C) Mole Fraction(x).

Table 4.2 Gain-Input Power for the Structure Si/Siox

The Structure	Input Power (dBm)	Gain(dB)
	h = 0.2 nm	55
0.10.0	h = 0.5nm	45
Si/SiOx	h = 1nm	38
	h = 1.5 nm	30
	$\rho = 8 nm$	34
	$ ho = 10 \ nm$	27
Si/SiOx	$ ho = 12 \ nm$	26
	$ ho = 16 \ nm$	22
	x = 0.11	10
	x = 0.15	8.8
Si/SiOx	x = 0.25	8
	x = 0.35	6.9

Table 4.3 Gain-Output Power for the Structure Si/Sio_x

The Structure	Output Power(dBm)	Gain(dBm)
	h = 0.2 nm	56
21/212	h = 0.5nm	45
Si/SiOx	h = 1nm	38
	$h = 1.5 \ nm$	30
	$ ho = 8 \ nm$	35
	$ ho = 10 \ nm$	26
Si/SiOx	$ ho = 12 \ nm$	29
	ho=16 nm	22
	x = 0.11	10
	x = 0.15	8.8
Si/SiOx	x = 0.25	8
	x = 0.35	6.9

4.4. Dynamical Effects for Si/SiO_x

A silicon (Si) quantum dot (QD) laser's electron dynamics are complicated, involving elements such as temperature, optical feedback, and electron escape rate. To maximum laser performance, it is essential to comprehend these dynamics, which include stability, emission wavelength, and lasing properties.

The carrier density of the structures Si/SiO_x in the WL is displayed Because the barrier layer was neglected,

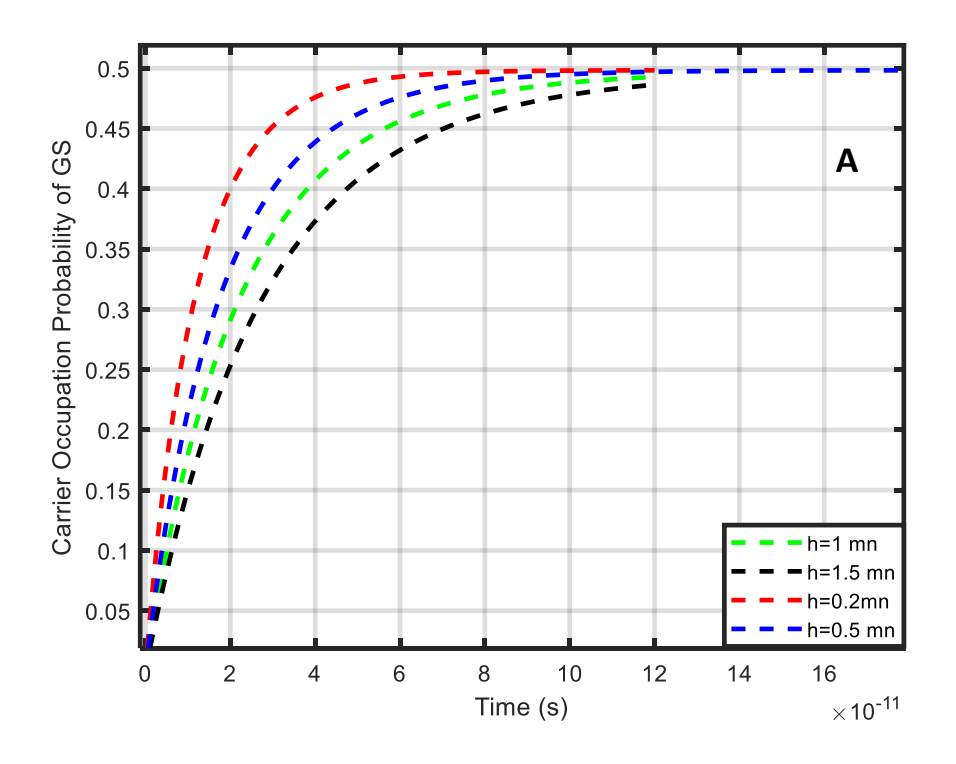
The steady state is reached in each of these curves when the rate of carrier loss (from spontaneous and nonradiative recombination) and carrier capture are balanced. A slight alteration is seen in Fig. 4.4 (C) upon altering the Si/SiO_x -mole fraction in the WL., where it takes a little longer to saturate than in Fig.2 A significant effect is seen when the QD shifts from height (h=0.2 nm to h=1.5 nm) Si/SiO_x

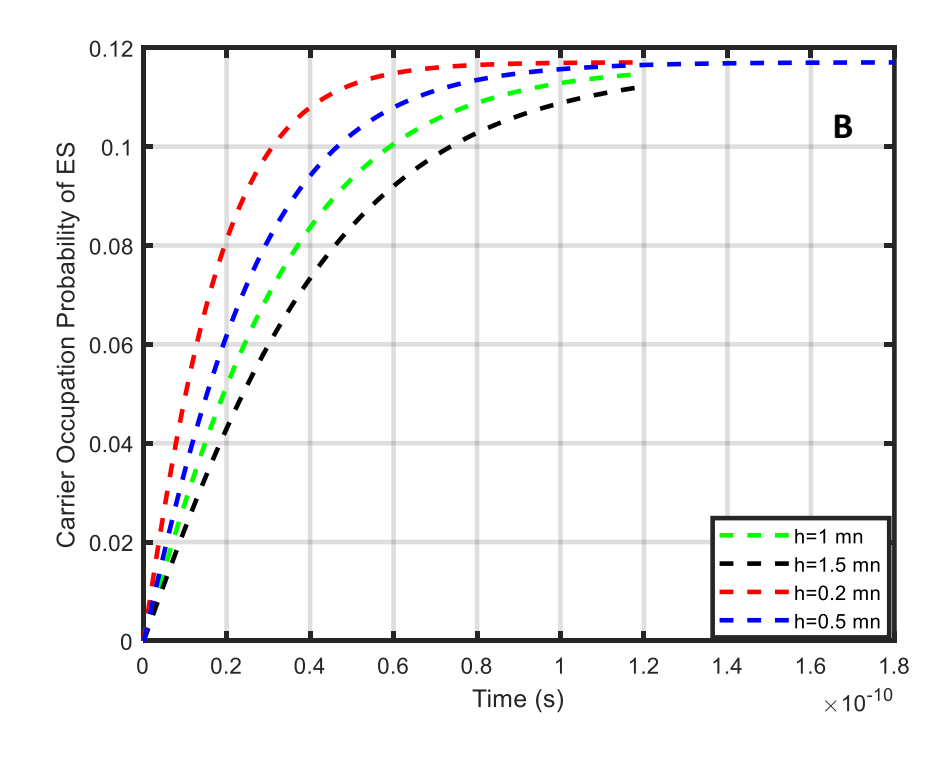
4.5. Dynamical Effects

In Fig. 4.5 shows carrier occupation probabilities vs time at the change QD size (height from h=0.2 nm, h=0.5 nm, h=1 nm to h=1.5 nm), Fig. 4.5 (A) GS occupation probabilities for Si QD where it takes here a somewhat long time. Fig. 4.5 (B) illustrate the ES occupation probabilities for Si QD, the barrier region take more interval time from ground state and excited state by 20 ps to stability case this mean the difference between barrier region and ground state in the interval time to S-T be (20 to 30 ps).

4.5 (C) explain the electrons concentration for the barrier region at mole fraction different we noted that upper height (h=2nm) is faster to (S-T) in 4.5 (C) It show the lines for disc high different be low in barrier region compared in ground state and excited state. The carrier density $(3.6\times10^{-12} \text{ cm}^{-3})$ for WL is lower than the value obtained in[100] due to the neglect of barrier layer. The value of steady state carrier density in the wetting layer is $\sim (5\times10^{14} \text{ cm}^{-3})$ which is in the range of the

carrier density used in chapter three. at the steady state the carrier density (3.6 \times 10¹²) for barrier layer is less than the number found in[100]. The significance of incorporating the WL into the SiO_x computations can be determined from these graphs.





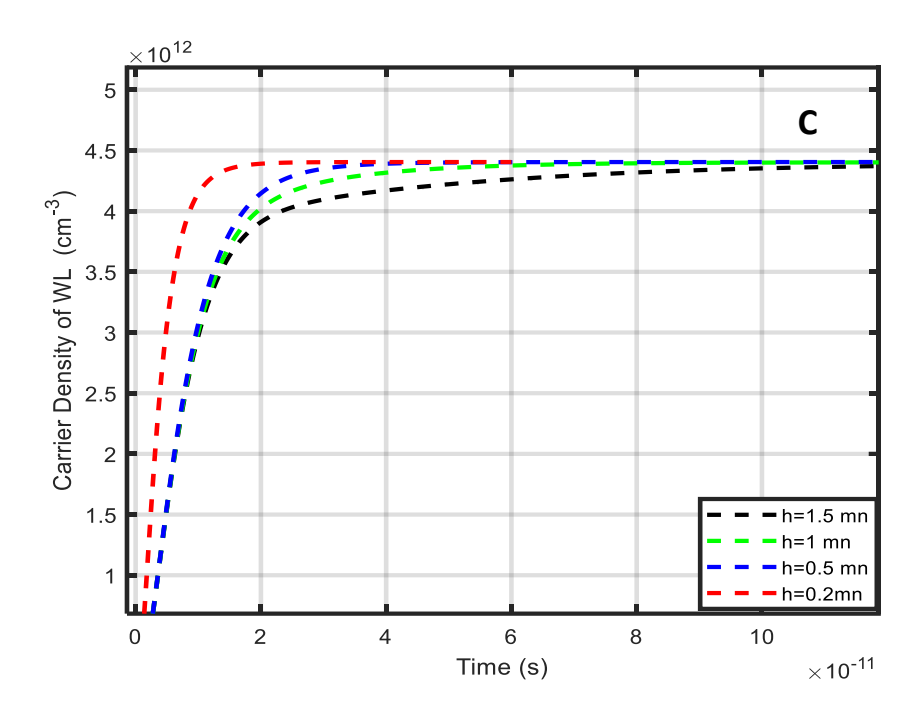
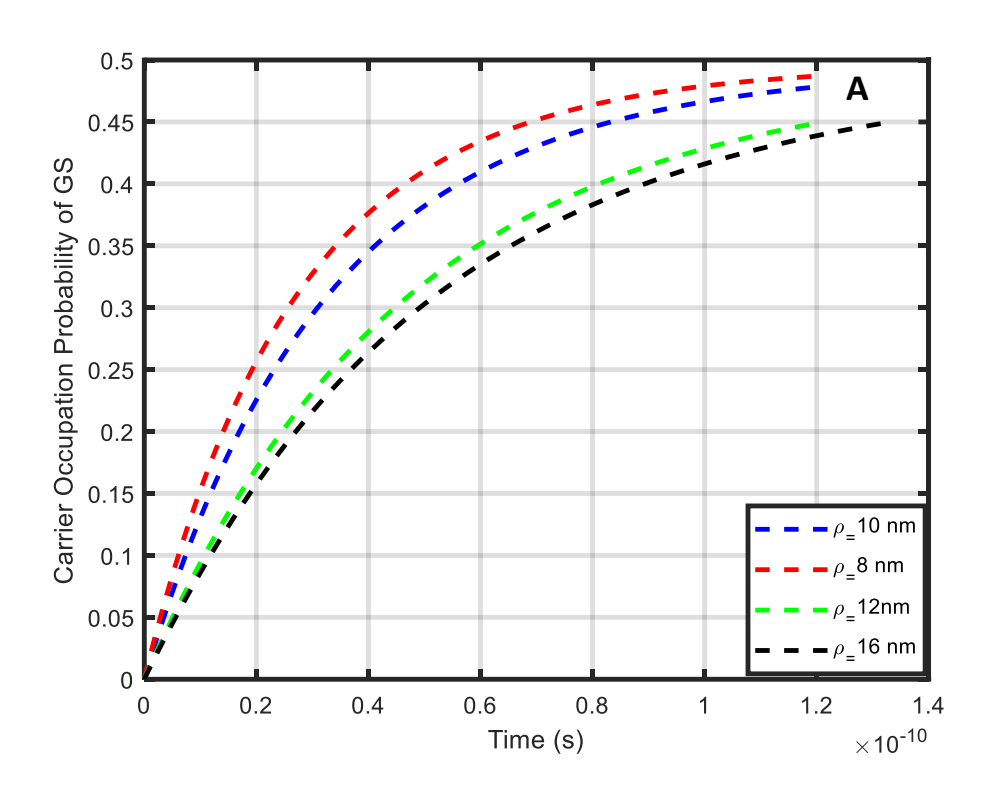


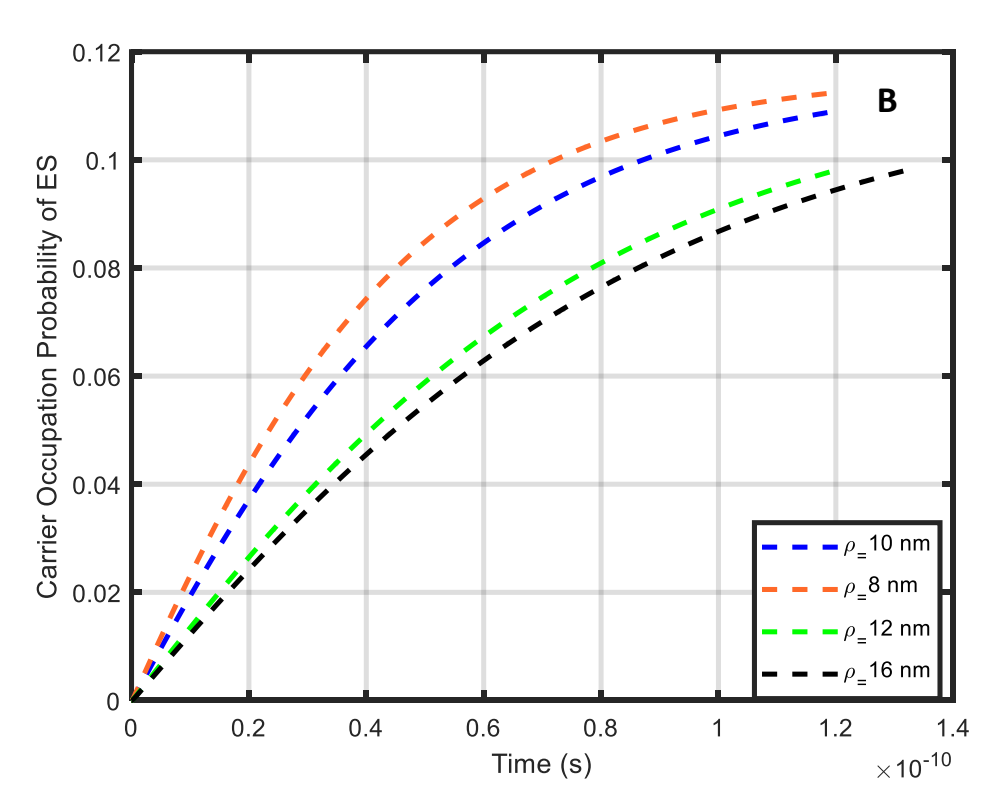
Figure 4.5: plot the relation between Carrier occupation probability verse time four disc high for QD-L (h=0.5 nm,1nm, 1.5 nm ,2 nm) (A) excited state. (B) ground state (C) carrier density in barrier region layer

In Fig. 4.6 shows carrier occupation probabilities vs time at the change radius QD size (from ρ =8 nm, ρ =10 nm, ρ =12 nm to ρ =16 nm), Fig. 4.6 (A) GS occupation probabilities for Si QD. The excited state in the figures sum slow from ground state access to stable case and so laxation between ground state and excited state be quicker from laxation between excited state and wetting region.

Fig. 4.6 (B)illustrate the ES occupation probabilities for Si QD Fig. 4.6 (C) explain WL occupation probabilities for SiO_x wetting layer. Sum figures show the stability case (ST) be between average of density losses due to non-radiative recombination and the spontaneous possibility ground state and excited state.

where it takes here a somewhat long time (compared with Fig. 4.5) to saturate.





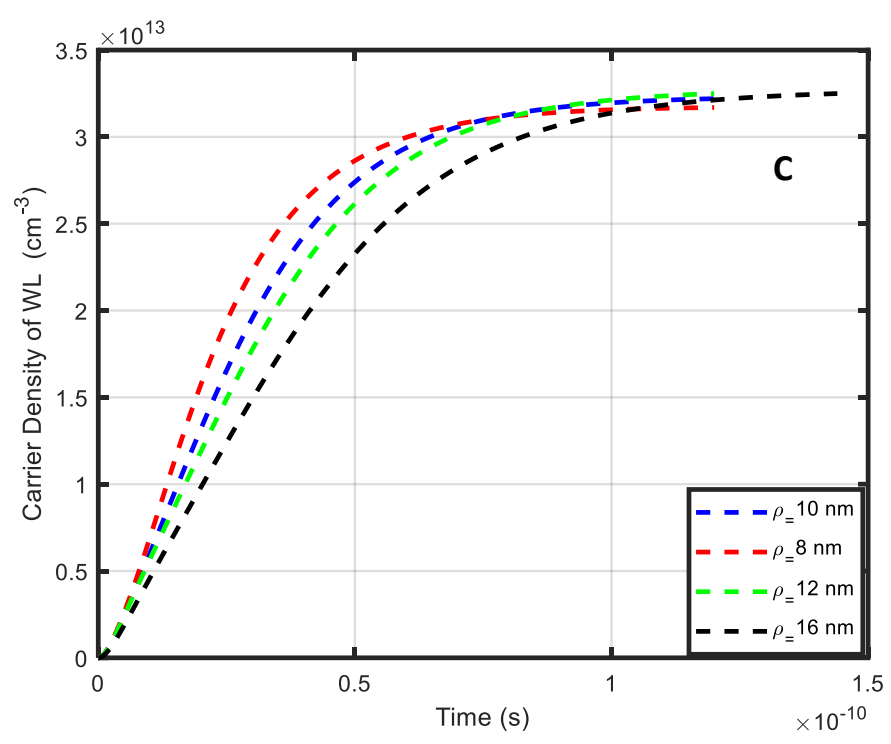
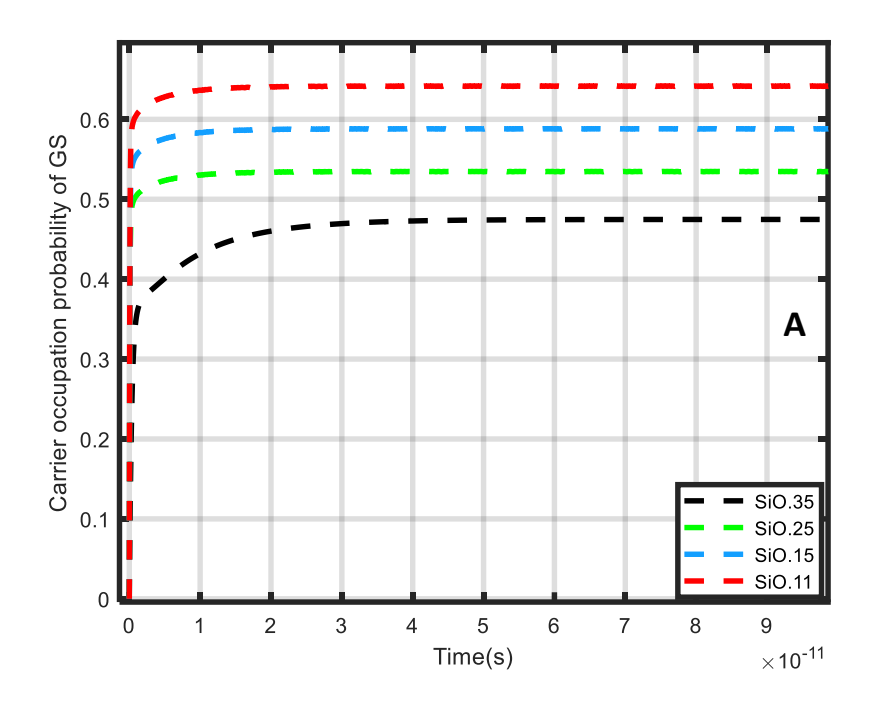
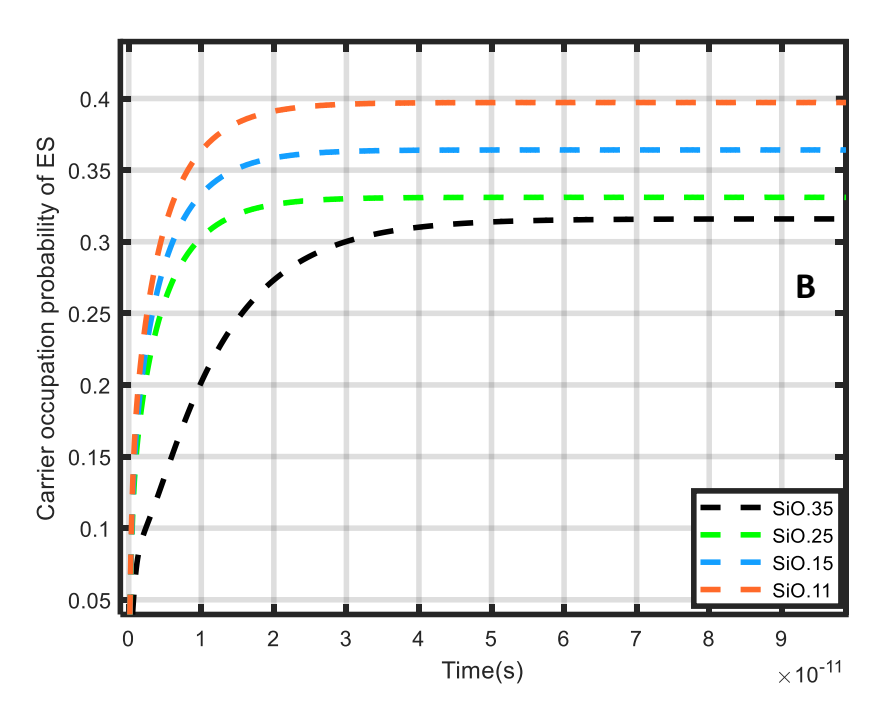


Figure 4.6: plot the relation between Carrier occupation probability verse time four-disc radius for QD-L (ρ=8 nm,10 nm, 12 nm,16 nm) (A) excited state. (B) ground state (C) carrier density in barrier region layer

In Fig. 4.7 shows carrier occupation probabilities vs time at the change mole fraction WL size (from x=0.11, x=.15, x=0.25 to x=0.35), we note a small change is observed when SiO_x -mole fraction in the WL is changed Fig. 4.7 (A) GS occupation probabilities for Si QD, Fig. 4.7 (B) illustrate the ES occupation probabilities for Si QD Fig. 4.6 (C) explain WL occupation probabilities for SiO_x wetting layer. The figures one explains the importance of including the barrier (SiO_x) in the QD-L accounts. Figure. 4.7 explain the (Ground State) is the upper one with 10 ps but it takes a longer time to reach steady state than WL although of the longer rate for transition between the ground state and excited state.





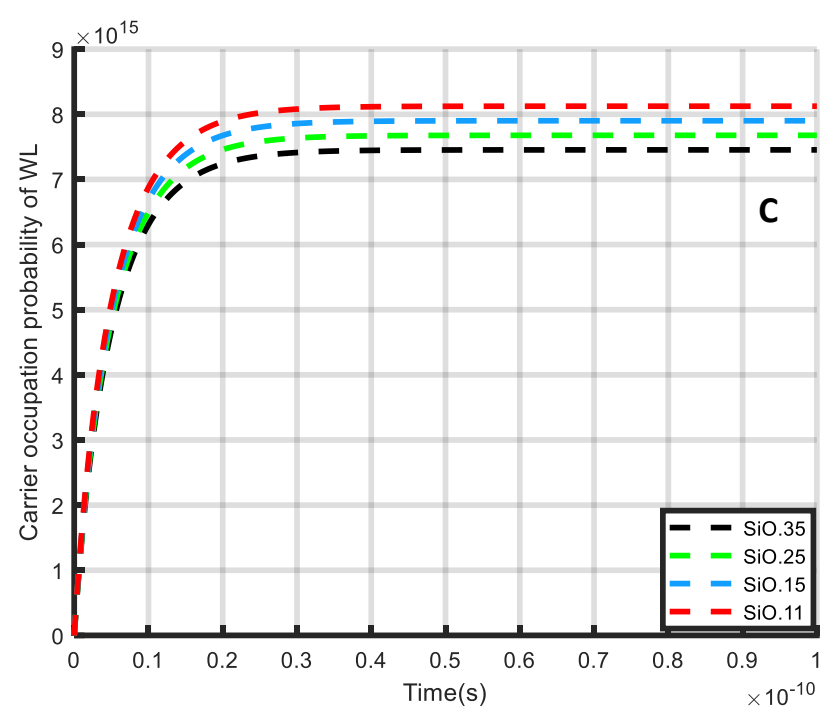
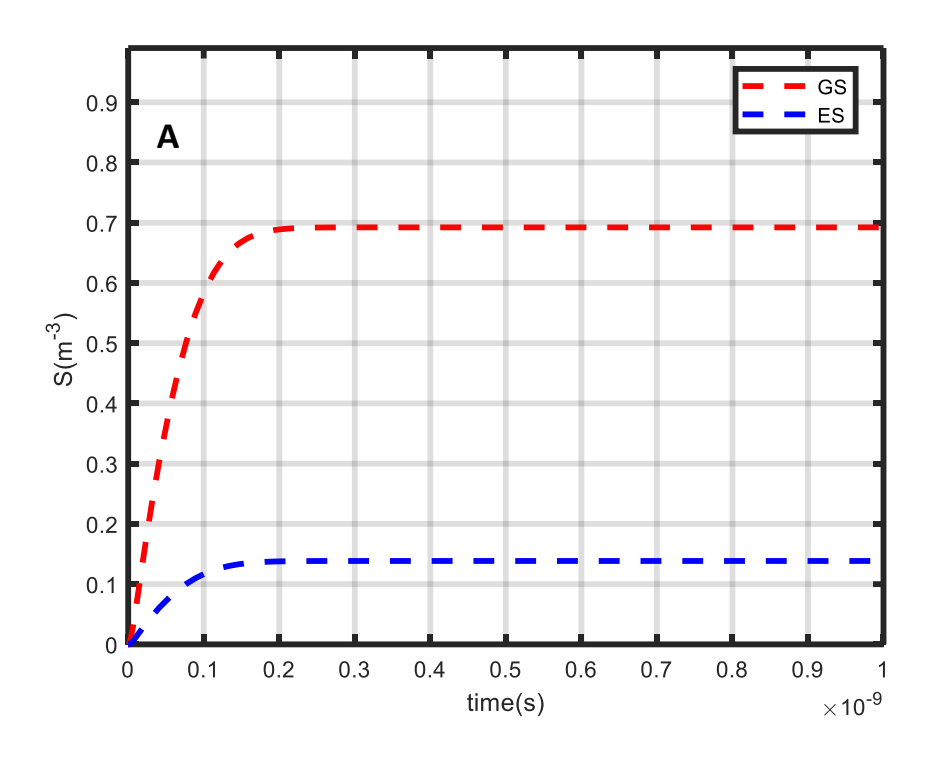


Figure 4.7: plot Carrier concentration for different the mole fraction system Si/SiO_x (x=0.11, 0.15, 0.25 and 0.35) (A) excited state . (B) ground state (C) wetting layer

Figure 4.8: compare between Carrier density for QD Si/SiO₂ structure for GS and ES where we noted that GS red dash line be high from ES blue dash line because GS have more between Carrier density at started pumping



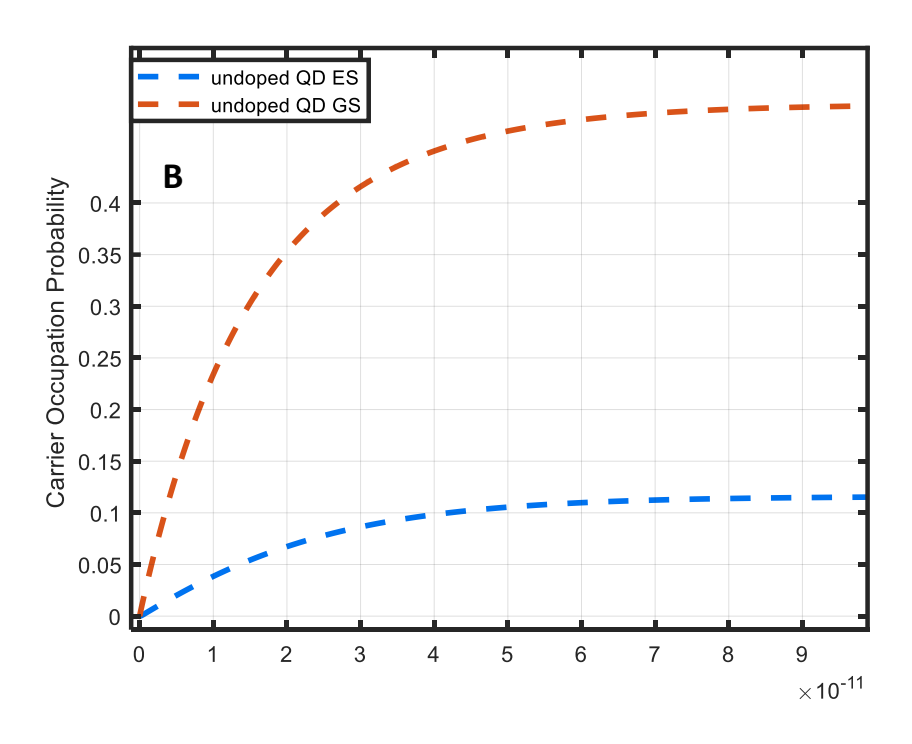


Figure 4.8: Carrier Density of QD Occupation of GS (Red Curve) And ES (Blue Curve). for Structure for Si/Sio2 (A) Undoped QD-L (B) Doped QD-L



Conclusions and Recommendations and Future Work

5.1 Conclusions

- 1. The energy levels (subbands) for both conduction and valence bands are calculated using the quantum disc mode.
- 2. The parameters required for calculation are specified and computed using relevant relations
- 3. Electronic and optical, linear, static and dynamic properties of SI-based quantum dot laser structures are specified to cover the effects of layers (QD, WL
- 4. Calculate energy levels (subbands) for both conduction and valence bands for composition WL
- 5. Calculate energy levels (subbands) for both conduction and valence for quantum size (height and radius) effects
- 6. The effect of homogenous linewidth on saturation behavior of these amplifiers is studied. According to this there are four groups of structures
- 7. the gain peak reduced and shifted to longer wavelength with increasing SiO_x-mole fraction in the WL.
- 8. The number of peaks depends on the transitions taken (ground- and excited-state transitions). The wavelength shift is small for the ES peak.
- 9. A smaller effect of WL layer on the gain is shown. The wavelength is red shifted by ~100 nm when Al mole fraction in the WL is increased by 0.2 the highest gain obtained in these group of Si-structures is 70 cm⁻¹ for QDL.
- 10. The gain is increased by 50cm-1 for each 1nm height reduction while the wavelength is shortened by~230nm.
- 11.QD structure well confinement of gives good gain saturation. This can be done by using a QD with low gap or by using a WL with enough (high) gap.
- 12. Changing QD-radius is efficient to get gain saturation than changing QD-height.
- 13. The inhomogeneous Gaussian function is shown to increases gain.

- 14.It is shown that the structure Si/SiO_x , with is better using for inline electrostatic amplifiers applications primarily in scientific and industrial because we get the linear optical gain upper .
- 15. The contribution due to changing SiO_x -composition in WL layer on input powergain relation is minor
- 16. The results explain the interested of the barrier region in the quantum dot laser accounts. The structure Si/SiO_x when the concentration (0.15 mole fraction) is more appropriate for inline static amplification applications.
- 17. The occupation probabilities of ES and GS when the QD changes from disc height to disc radius.
- 18. Calculate the effect on input power-gain relation for disc height QDL size where we note high gain at height dot size at (8 nm).
- 19. Show that disc radius QDL size on input power-gain relation where low gain at radius QD size at (ρ =16) because bigger to its low bandgap
- 20.Carrier occupation probabilities vs time at the change QD size (height and radii QDL)

5.2 Recommendations and Future Work

As a continuation to the work in this thesis the following points can be addressed in the future

- 1- Study of type Si/SiO QD for nonlinear gain
- 2- Completely Inhomogeneous Density-Matrix Theory.
- 3- Gain as a Function of Homogeneous Linewidth
- 4- The used of Si/SiO QD structures in bio-sensors applications.
- 5- The study of QD efficiency Si/SiO photonic structures

REFRENCES

- [1]C.P.Poole Jr and F.JOwens, "Introduction to Nanotechnology" Hoboken, NJ,USA:John Wiley and sons,Inc.,2003.
- [2] J. E. Hulla, S. C. Sahu, and A. W. Hayes, "Nanotechnology: History and future," *Hum. Exp. Toxicol.*, vol. 34, no. 12, pp. 1318–1321, 2015.
- [3] S. Mobasser and A. Akbar Firoozi, "Review of Nanotechnology Applications in Science and Engineering," *J. homepage www.ojceu.ir J. Civ. Eng. Urban.*, vol. 6, no. 4, pp. 84–93, 2016.
- [4] A. Santamaria, "Historical overview of nanotechnology and nanotoxicology," *Methods Mol. Biol.*, vol. 926, pp. 1–12, 2012
- [5] S. Bayda, M. Adeel, T. Tuccinardi, M. Cordani, and F. Rizzolio, "The history of nanoscience and nanotechnology: from chemical–physical applications to nanomedicine," *Molecules*, vol. 25, no. 1, p. 112, 2019.
- [6] N. Baig, I. Kammakakam, W. Falath, and I. Kammakakam, "Nanomaterials: A review of synthesis methods, properties, recent progress, and challenges," *Mater. Adv.*, vol. 2, no. 6, pp. 1821–1871, 2021
- [7] M. Sajid, "Nanomaterials: types, properties, recent advances, and toxicity concerns," *Curr. Opin. Environ. Sci. Heal.*, vol. 25, p. 100319, 2022.
- [8] AB Asha, and R Narain. "Nanomaterials properties." In *Polymer science and nanotechnology*, pp. 343-359. Elsevier, 2020.
- [9] R.Singh, and R. K. Soni. "Laser-induced heating synthesis of hybrid nanoparticles." In *Noble Metal-Metal Oxide Hybrid Nanoparticles*, pp. 195-238. Woodhead Publishing, 2019.
- [10] B. D. Cameron and R. Zheng, "Advances in surface Plasmon resonance sensing," *Nanoplasmonics Adv. Device Appl.*, pp. 221–244, 2013.

- [11] M. Singh, M. Goyal, and K. Devlal, "Size and shape effects on the band gap of semiconductor compound nanomaterials," *J. Taibah Univ. Sci.*, vol. 12, no. 4, pp. 470–475, 2018.
- [12] S. Ramasamy and B. Purniah, "Electrical properties of nanostructured materials," *Proceedings-Indian Natl. Sci. Acad. Part A*, vol. 67, no. 1, pp. 85–102, 2001.
- [13] B. Mekuye and B. Abera, "Nanomaterials: An overview of synthesis, classification, characterization, and applications," *Nano Sel.*, vol. 4, no. 8, pp. 486–501, 2023.
- [14] N. Joudeh and D. Linke, "Nanoparticle classification, physicochemical properties, characterization, and applications: a comprehensive review for biologists," *J. Nanobiotechnology*, vol. 20, no. 1, pp. 1–29, 2022.
- [15] X. Zheng, P. Zhang, Z. Fu, S. Meng, L. Dai, and H. Yang, "Applications of nanomaterials in tissue engineering," *RSC Adv.*, vol. 11, no. 31, pp. 19041–19058, 2021.
- [16] S. Malik, K. Muhammad, and Y. Waheed, "Nanotechnology: A Revolution in Modern Industry," *Molecules*, vol. 28, no. 2, 2023.
- [17] J. PIPREK, "Photon Generation," *Semicond. Optoelectron. Devices*, pp. 121–139, 2003.
- [18] J. PIPREK, "Photon Generation," *Semicond. Optoelectron. Devices*, pp. 121–139, 2003.
- [19] K. F. Renk, "Basics of laser physics". Berlin: Springer Berlin Heidelberg, vol. 33, 2012.
- [20] M. Eilchi and P. Parvin. "Gain saturation in optical fiber laser amplifiers." *Fiber Laser*, pp. 297-320, (2016).

- [21] M. Maák and P. Pál, "Laser Physics Laser Physics 1 12 2.. Interaction of light with matter Interaction of light with matter," *Laser Phys.*, vol. 12, pp. 1–18.
- [22] H. E. Wagie and P. Geissinger, "Hole-burning spectroscopy as a probe of nano-environments and processes in biomolecules: A review," *Appl. Spectrosc.*, vol. 66, no. 6, pp. 609–627, 2012.
- [23] A. Yariv and P. Yeh, Photonics: Optical Electronics in Modern Communications, 6th ed., Cambridge University Press, Cambridge, U.K., , ch. 12, pp. 396–419, 2007.
- [24] Z. Kang, Y. Liu, and S. T. Lee, "Small-sized silicon nanoparticles: New nanolights and nanocatalysts," *Nanoscale*, vol. 3, no. 3, pp. 777–791, 2011.
- [25] H. Chang and S. Q. Sun, "Silicon nanoparticles: Preparation, properties, and applications," Chinese Phys. B, vol. 23, no. 8, pp. 1–14, 2014.
- [26] T. Tsuchiya, "Silicon and Related Materials," Compr. Microsystems, vol. 1, pp. 1–23, 2007
- [27] S. Dutta and P. Dutta, "Silicon A Versatile Material," *Sci. Report.*, vol. 1, no. February, pp. 40–42, 2010.
- [28] D. Kumar and M. Johari, "Characteristics of silicon crystal, its covalent bonding and their structure, electrical properties, uses," *AIP Conf. Proc.*, vol. 2220, May, 2020.
- [29] H. Kang, "Crystalline Silicon vs. Amorphous Silicon: The Significance of Structural Differences in Photovoltaic Applications," *IOP Conf. Ser. Earth Environ. Sci.*, vol. 726, no. 1, 2021.
- [30] I. Shutsko, "Physical properties of n-doped hydrogenated silicon thin film as back and front surface field in Silicon Heterojunction Solar Cells," Maste Thesis, no. October 2016, 2016.

- [31] M. Tilli and A. Haapalinna, "Properties of silicon." In Handbook of silicon based MEMS materials and technologies, pp. 3-17. Elsevier, 2020.
- [32] A. Gahlot, "Physical Methods of Nanoparticles Preparation-An Overview," *Int. J. Adv. Eng. Manag.*, vol. 3, no. 12, p. 812, 2021.
- [33] D. Bimberg, "Quantum dots for lasers, amplifiers and computing," no. January 2004, pp. 2–2, 2004.
- [34] A. P. Alivisatos, "Downloaded from www.sciencemag.org on March 4, 2011 Downloaded from www.sciencemag.org on March 4, 2011," *Dots. Sci.*, pp. 933–937, 1996.
- [35] M. Odeh, "About the Quantum Mechanics of the Electrons in Crystal Lattices Historical Background: Bloch Wave Theorem:," p. 555, 2018.
- [36] Fröhlich, "Die Spezifische Warme Der Elektronen Metallteilchen Bel Tiefen," no. 5, pp. 406–412, 1937.
- [37] S. Background and N. Prize, "Scientific Background to the Nobel Prize in Chemistry 2023 QUA N T U M D O TS SE E DS OF NA NOSCI ENCE The Nobel Committee for Chemistry," vol. 50005, 2023.
- [38] Y. F. Ogrin, V. N. Lutskii, and M. I. Elinson, "Observation of quantum size effects in thin bismuth films," ZhETF Pisma Redaktsiiu, vol. 3, p. 114, 1966.
- [39] K. Agarwal, H. Rai, and S. Mondal, "Quantum dots: an overview of synthesis, properties, and applications," *Mater. Res. Express*, vol. 10, no. 6, 2023.
- [40] R. Karmakar, "Review Article Quantum Dots and it method of preparations revisited," Prajnan O *Sadhona–a Sci. Annu.*, vol. 2, pp. 116–142, 2015.
- [41] S. E. E. Profile, "The Institution of Electronics and Telecommunication Engineers," IETE J. Educ., vol. 33, no. 1, pp. 89–92, 1992.

- [42] P. Kumar, R. Kumar, IK. Iliev, HI. Beloev, S. Praveenkumar, N.Sunnam, and A. Bhatia. "Engineered Quantum Dot Solar Cells: From Fundamentals to Applications." Plasmonics pp 1-21 (2025)
- [43] S. Kaur, A. Srivastava, V. Aggarwal, and B. D. Malhotra, "Applications of Carbon Quantum Dots in Cancer Detection and Therapy," *Adv. Transdiscipl. Eng.*, vol. 27, pp. 311–316, 2022.
- [44] D. Bera, L. Qian, T. K. Tseng, and P. H. Holloway, "Quantum dots and their multimodal applications: A review," *Materials (Basel)*., vol. 3, no. 4, pp. 2260–2345, 2010.
- [45] Y. M. Huang *et al.*, "Gateway towards recent developments in quantum dot-based light-emitting diodes," *Nanoscale*, vol. 14, no. 11, pp. 4042–4064, 2021.
- [46] M. Grabolle, M. Spieles, V. Lesnyak, N. Gaponik, A. Eychmüller, and U. Resch-Genger, "Determination of the fluorescence quantum yield of quantum dots: Suitable procedures and achievable uncertainties," *Anal. Chem.*, vol. 81, no. 15, pp. 6285–6294, 2009.
- [47] H. Moon, C. Lee, W. Lee, J. Kim, and H. Chae, "Stability of Quantum Dots, Quantum Dot Films, and Quantum Dot Light-Emitting Diodes for Display Applications," *Adv. Mater.*, vol. 31, no. 34, pp. 1–14, 2019.
- [48] J. H. Marsh, D. Bhattacharyya, A. S. Helmy, E. A. Avrutin, and A. C. Bryce, "Engineering quantum-dot lasers," *Phys. E Low-Dimensional Syst. Nanostructures*, vol. 8, no. 2, pp. 154–163, 2000.
- [49] J. C. Norman, R. P. Mirin, and J. E. Bowers, "Quantum dot lasers—History and future prospects," *J. Vac. Sci. Technol. A*, vol. 39, no. 2, 2021.
- [50] F. Grillot, J. Duan, B. Dong, and H. Huang, Semiconductor quantum dot lasers: Genesis, prospects, and challenges. 2024.

- [51] D. Huiwen, JS. Park, X. Yu, Z. Liu, H.Jia, H. Zeng, J. Yang, S. Pan, S. Chen, A. Seeds, M. Tang "1.3 μm InAs/GaAs quantum-dot lasers with p type, n-type, and co-doped modulation." Advanced Physics Research 3, no. 10 (2024): 2400045.
- [52] H. Salama, B. Smaani, F. Nasri, and A. Tshipamba, "Nanotechnology and Quantum Dot Lasers," *J. Comput. Sci. Technol. Stud.*, vol. 5, no. 1, pp. 45–51, 2023.
- [53] B. Al-Nashy and A. H. Al-Khursan, "Linear and nonlinear gain of sb-based quantum-dot semiconductor optical amplifiers," *Recent Patents Electr. Eng.*, vol. 3, no. 3, pp. 232–240, 2010.
- [54] M. A. Al-Mossawi, A. G. Al-Shatravi, and A. H. Al-Khursan, "CdSe/ZnSe Quantum-Dot Semiconductor Optical Amplifiers," *Insciences J.*, no. April, pp. 52–62, 2012
- [55] L. Mangolini, "Synthesis, properties, and applications of silicon nanocrystals," *J. Vac. Sci. Technol. B, Nanotechnol. Microelectron. Mater. Process. Meas. Phenom.*, vol. 31, no. 2, 2013.
- [56] O. Qasaimeh, "Gain-Clamped Quantum Dot Semiconductor Optical Amplifiers," *Int. J. Comput. Electr. Eng.*, vol. 6, no. 3, pp. 271–274, 2014.
- [57] A. Y. Liu, S. Srinivasan, J. Norman, A. C. Gossard, and J. E. Bowers, "Quantum dot lasers for silicon photonics [Invited]," vol. 3, no. 5, pp. 1–9, 2015.
- [58] C. M. Tiebout, "UC Santa Barbara," J. Polit. Econ., vol. 64(5), pp. 416–424, 1956.
- [59] J. C. Norman *et al.*, "A review of high-performance quantum dot lasers on silicon," *IEEE J. Quantum Electron.*, vol. 55, no. 2, pp. 1–11, 2019.
- [60] A. G. Al-Shatravi, B. O. Al-Nashy, and A. H. Al-Khursan, "Total gain of InTlAsSb quantum dot structures," *J. Opt. Commun.*, vol. 44, no. s1, pp. S29–S34, 2023.

- [61] B. Dong, "Quantum Dot Lasers on Silicon: Nonlinear Properties, Dynamics, and Applications". Springer Nature, 2023.
- [62] Kornyshov G.O *et al.*, "Relationship between wavelength and gain in lasers based on quantum wells, dots, and well-dots," *Semiconductors*, vol. 56, no. 12, p. 915, 2022.
- [63] M. Abdullah, B. O. Al-Nashy, and A. H. Al-Khursan, "Optical gain of CdxZn1-xTe quantum dot structures," Micro Nano Lett., vol. 18, no. 9–12, 2023.
- [64] K. Papatryfonos, J.C. Girard, M.Tang, H.Deng, A.J.Seeds, C.David, G.Rodary, H. Liuand Selviah."Low-Defect Quantum Dot Lasers Directly Grown on Silicon Exhibiting Low Threshold Current and High Output Power at Elevated Temperatures." *Advanced Photonics Research* 6, no. 3,p. 2400082 (2025).
- [65] A. Wold and K. Dwight, "Electrical Properties of Semiconductors," *Solid State Chem.*, pp. 31–46, 1993.
- [66] K. Jungho and S L. Chuang. "Theoretical and experimental study of optical gain, refractive index change, and linewidth enhancement factor of p-doped quantum-dot lasers." *IEEE journal of quantum electronics* 42, no. 9, pp. 942-952, (2006).
- [67] D. Sannino, "Types and Classification of Nanomaterials," *Nanotechnol. Trends Futur. Appl.*, pp. 15–38, 2021.
- [68] K. Konishi, T.Kamimura, M.H. Wong, K.Sasaki, A.Kuramata, S. Yamakoshi and M.Higashiwaki, "Large conduction band offset at SiO2/β-Ga2O3 heterojunction determined by x-ray photoelectron spectroscopy." *physica status solidi (b)* 253, no. 4, pp. 623-625, (2016).
- [69] J. L. Alay and M. Hirose, "The valence band alignment at ultrathin SiO2/Si interfaces," J. Appl. Phys., vol. 81, no. 3, pp. 1606–1608, 1997.

- [70] I. Filikhin, S. G. Matinyan, B. K. Schmid, and B. Vlahovic, "Electronic and level statistics properties of Si/SiO2 quantum dots," Phys. E Low Dimensional Syst. Nanostructures, vol. 42, no. 7, pp. 1979–1983, 2010.
- [71] S. M. Turkane and A. H. Ansari, "Performance Analysis of TFET Using Si0.35Ge0.65/Si Hetero-junction Hetero-dielectric with Buried Oxide Layer," Proc. 2018 IEEE Glob. Conf. Wirel. Comput. Networking, GCWCN 2018, no. November 2018, pp. 91–97, 2018.
- [72] T. R. Lenka and A. K. Panda, "AlGaN/GaN-based HEMT on SiC substrate for microwave characteristics using different passivation layers," Pramana J. Phys., vol. 79, no. 1, pp. 151–163, 2012.
- [73] R. Kumar Chanana, "Determination of hole effective mass in SiO2 and SiC conduction band offset using Fowler-Nordheim tunneling characteristics across metal-oxide-semiconductor structures after applying oxide field corrections," J. Appl. Phys., vol. 109, no. 10, 2011.
- [74] J. Kim, M. Laemmlin, C. Meuer, D. Bimberg, and G. Eisenstein, "Static gain saturation model of quantum-dot semiconductor optical amplifiers," *IEEE J. Quantum Electron.*, vol. 44, no. 7, pp. 658–666, 2008.
- [75] J. Kim and S. L. Chuang, "Theoretical and experimental study of optical gain, refractive index change, and linewidth enhancement factor of p-doped quantum-dot lasers," *IEEE J. Quantum Electron.*, vol. 42, no. 9, pp. 942–952, 2006.
- [76] N. N. Ledentsov *et al.*, "Quantum-dot heterostructure lasers," *IEEE J. Sel. Top. Quantum Electron.*, vol. 6, no. 3, pp. 439–451, 2000.
- [77] J. N. Jabir, S. M. M. Ameen, and A. H. Al-Khursan, "Plasmonic Quantum Dot Nanolaser: Effect of 'Waveguide Fermi Energy," *Plasmonics*, vol. 14, no. 6, pp. 1881–1891, 2019.

- [78] P. C. Ku, C. J. Chang-Hasnain, and S. L. Chuang, "Slow light in semiconductor heterostructures," *J. Phys. D. Appl. Phys.*, vol. 40, no. 5, 2007.
- [79] J. Sun, M. Chen, T. Huang, G. Ding, and Z. Wang, "Coexistence of the Band Filling Effect and Trap-State Filling in the Size-Dependent Photoluminescence Blue Shift of MAPbBr3 Nanoparticles," *Nanomaterials*, vol. 14, no. 19, 2024.
- [80] K. G. Saw, N. M. Aznan, F. K. Yam, S. S. Ng, and S. Y. Pung, "New insights on the burstein-moss shift and band gap narrowing in indium-doped zinc oxide thin films," *PLoS One*, vol. 10, no. 10, 2015.
- [81] L. W. Casperson, "PDXScholar Rate-Equation Approximations in High-Gain Lasers," vol. 55, pp. 3073–3085, 1997.
- [82] Miller.Ch, "Laser Rate Equations Dynamical System-," *Nonlinear Dyn.*, no. laser rate equations, p. 6, 2001.
- [83] F. Habibullah and W. P. Huang, "A self-consistent analysis of semiconductor laser rate equations for system simulation purpose," *Opt. Commun.*, vol. 258, no. 2, pp. 230–242, 2006.
- [84] U. Woggon. "Optical properties of semiconductor quantum dots,". Berlin, Heidelberg: Springer Berlin Heidelberg, 1997.
- [85] P. Harrison and A. Valavanis, *Quantum wells, wires and dots: theoretical and computational physics of semiconductor nanostructures*. John Wiley & Sons, 2016.
- [86] C. Wang, F. Grillot, and J. Even, "Impacts of wetting layer and excited state on the modulation response of quantum-dot lasers," *IEEE J. Quantum Electron.*, vol. 48, no. 9, pp. 1144–1150, 2012.
- [87] B. Al-Nashy and A. H., "The Composition Effect on the Dynamics of Electrons in Sb-Based QD-SOAs," *Sel. Top. Opt. Amplifiers Present Scenar.*, no. February 2012, 2012.

- [88] A. A. Dikshit and J. M. Pikal, "Carrier distribution, gain, and lasing in 1.3-μm InAs-InGaAs quantum-dot lasers," *IEEE J. Quantum Electron.*, vol. 40, no. 2, pp. 105–112, 2004.
- [89] Y. Ben Ezra, B. I. Lembrikov, and M. Haridim, "Specific features of XGM in QD-SOA," *IEEE J. Quantum Electron.*, vol. 43, no. 8, pp. 730–737, 2007, doi: 10.1109/JQE.2007.
- [90] J. L. Xiao and Y. Z. Huang, "Numerical analysis of gain saturation, noise figure, and carrier distribution for quantum-dot semiconductor-optical amplifiers," *IEEE J. Quantum Electron.*, vol. 44, no. 5, pp. 448–455, 2008.
- [91] R. H. A. Ali, B. A. Ghalib, and R. S. Abdoon, "Dynamics of Quantum Dot Semiconductor Lasers on Mutual Loop System With Optoelectronic Feedback," *J. Optoelectron. Biomed. Mater.*, vol. 11, no. 4, pp. 69–74, 2019.
- [92] T. W. Berg, J. Mørk, and J. M. Hvam, "Gain dynamics and saturation in semiconductor quantum dot amplifiers," *New J. Phys.*, vol. 6, no. November, pp. 1–23, 2004.
- [93] T. W. Berg, J. Mørk, and J. M. Hvam, "Gain dynamics and saturation in semiconductor quantum dot amplifiers," *New J. Phys.*, vol. 6, pp. 1–23, 2004.
- [94] T. W. Berg and J. Mørk, "Saturation and noise properties of quantum-dot optical amplifiers," *IEEE J. Quantum Electron.*, vol. 40, no. 11, pp. 1527–1539, 2004.
- [95] T. W. Berg and J. Mørk, "Quantum dot amplifiers with high output power and low noise," *Appl. Phys. Lett.*, vol. 82, no. 18, pp. 3083–3085, 2003.
- [96] Y. Wu, L. Jiang, and L. V. Asryan, "Output power of a quantum dot laser: Effects of excited states," *J. Appl. Phys.*, vol. 118, no. 18, 2015.
- [97] J. P. Reithmaier *et al.*, "InP based lasers and optical amplifiers with wire-/dot-like active regions," *J. Phys. D. Appl. Phys.*, vol. 38, no. 13, pp. 2088–2102, 2005.

[98] D. W. Reschner, E. Gehrig, and O. Hess, "Pulse amplification and spatio-spectral hole-burning in inhomogeneously broadened quantum-dot semiconductor optical amplifiers," *IEEE J. Quantum Electron.*, vol. 45, no. 1, pp. 21–33, 2009.

الخلاصة

لقد حظيت الليزرات المعتمدة على النقاط الكمومية والمدمجة على ركيزة السيليكون باهتمام كبير في السنوات الأخيرة، نظرًا لامتلاك النقاط الكمية خصائص بصرية مميّزة. تعتمد هذه الليزرات على النقاط الكمومية شبه الموصلة كوسطٍ فعّال لعملية الانبعاث الضوئي.

يمثّل دمج الليزرات الكمية على السيليكون خطوةً أساسية نحو تحقيق الدوائر الضوئية المتكاملة بالكامل. إذ يتيح هذا الدمج تشغيلًا بعتبة منخفضة، واستقرارًا حراريًا عاليًا، وانخفاض الحساسية تجاه العيوب والتغذية البصرية المرتدة، مقارنةً بليزرات الأبار الكمية أو الليزرات التقليدية. علاوةً على ذلك، فإن توافقها مع تقنيات تصنيع الدارات المتكاملة (CMOS) يجعل من الممكن تطوير أجهزة ضوئية إلكترونية مدمجة وفعّالة من حيث التكلفة.

تُستخدم الليزرات الكمية المعتمدة على السيليكون على نطاقٍ واسع في أنظمة الاتصالات الضوئية عالية السرعة، ونقل البيانات على الرقاقة، والدوائر الضوئية المتكاملة. كما تُظهر إمكانات واعدة في مجالات معالجة المعلومات الكمية، والربط الضوئي بين المعالجات، وتقنيات الاستشعار، بفضل كفاءتها العالية، وحجمها الصغير، وإمكانية ضبط أطوالها الموجية المنبعثة.

وقد تناولت الأبحاث العلمية الحديثة على نطاقٍ واسع موضوع الليزرات الكمية (QDLs) بوصفها الجيل القادم من مصادر الضوء شبه الموصلة، لما تتمتع به من أداء بصري متفوق مقارنةً بليزرات الآبار الكمية أو الليزرات التقليدية. إذ تعتمد هذه الليزرات على نقاط كمية نانوية تعمل كوسطٍ فعّال ينبعث منه الضوء عبر انتقالات بين مستويات طاقية. كما بحثت الدراسات في تأثير كلٍّ من توزيع أحجام النقاط الكمية وكثافتها على الخصائص الطيفية والديناميكية لليزر. وتركزت الأبحاث الحديثة على دمج الليزرات الكمية مع ركائز السيليكون، وهي خطوة رئيسية نحو تحقيق أنظمة ضوئية متكاملة.

في الفصل الأول، جرى تقديم ومناقشة عددٍ من المفاهيم الأساسية، شملت تقنيات تصنيع النقاط الكمية وتطبيقاتها المختلفة، ومفهوم الكسب البصري والفرق بين الاتساع الطيفي المتجانس وغير المتجانس، بالإضافة إلى البنية البلورية للسيليكون ومعاملات ميلر، والخصائص الفيزيائية لليزر النقطة الكمية.

أما في الفصل الثاني، فقد تم إجراء تحليلٍ لمستويات الطاقة في نطاقي التكافؤ والتوصيل باستخدام نموذج القرص الكمي، وذلك عبر التغيير المنهجي لارتفاع النقطة الكمية ونصف قطرها وسماكة طبقة الترطيب. أظهرت النتائج وجود علاقة عكسية بين أبعاد النقطة الكمية (الارتفاع ونصف القطر) ومستويات الطاقة المناظرة، مما يشير إلى أن زيادة ارتفاع النقطة الكمية تؤدي إلى انخفاض في مستويات الطاقة. كما تم إعداد مخطط تخطيطي لتوضيح الانتقالات الإلكترونية الممكنة بين هذه الحالات الكمية.

وفي الفصل الثالث، تم إجراء تحليلٍ شامل للعلاقة بين طول الموجة المنبعثة والكسب البصري من خلال تغيير ارتفاع النقطة الكمية ونصف قطرها وتركيبها وكثافة تيار الحقن. أظهرت النتائج أن لهذه المعاملات تأثيرًا جوهريًا في الأداء البصري لليزر، ولا سيما أن أقصى كسب بصري خطي تحقق عند الكسر المولي 3.15 في منطقة الحاجز المكوّنة من مادة SiOx ، مع ملاحظة زيادة في أطوال الموجات باتجاه النطاق المرئي.

أما في الفصل الرابع، فقد جرى نمذجة تراكيب الليزر الكمي المدروسة أعلاه باستخدام نظام معادلات المعدل (Rate Equations) بهدف تحليل العلاقة بين القدرة والكسب وتحديد خصائصها الديناميكية. وإضافة إلى حالات النقطة الكمية الأرضية والمثارة وطبقة الترطيب، تم إدراج طبقة الحاجز التي لم تحظ سابقًا بالاهتمام الكافي في الدراسات السابقة. أوضحت النتائج أهمية منطقة الحاجز في أداء ليزرات النقاط الكمية، حيث تبين أن البنية Si/SiOx عند تركيز 0.15 (كسر مولي) تعدّ الأنسب لتطبيقات التضخيم البصري الخطي.



جمهورية العراق وزارة التعليم العالي والبحث العلمي جامعة ميسان كلية العلوم قسم الفيزياء

الكسب البصري لليزر النقاط الكمومية الى Si

رسالة مقدمة إلى كلية العلوم/جامعة ميسان كجزء من متطلبات نيل درجة الماجستير علوم في الفيزياء

بواسطة

امیره حسن حسین

بكالوريوس فيزياء/ جامعة ميسان (٢٠٢٢)

بأشراف

أ.د باقر عبيد الناشي

٧٤٤١ه